Quiescent Coronal Loops Heated By Turbulence

by

Ian J. O'Neill

Institute of Mathematical and Physical Sciences
University of Wales Aberystwyth (UWA)

Dr. Xing Li (supervisor)

2006

Thesis
submitted to The University of Wales
by
Ian James O'Neill MPhys (Wales)
In Candidature for the Degree of
Philosophiae Doctor

Declaration

This work has not previously been accepted in substance for any degree and is not being concurrently submitted in candidature for any degree.

Signed ..... (candidate)

Date .....

Statement 1

This thesis is the result of my own investigations, except where otherwise stated. Other sources are acknowledged by footnotes giving explicit references. A bibliography is appended.

Signed ..... (candidate)

Date .....

Statement 2

I hereby give consent for my thesis, if accepted, to be made available for photocopying and for inter-library loan, and for the title and summary to be made available to outside organisations.

Signed ..... (candidate)

Date .....

Abstract

How the solar corona is heated continues to be a problem. Many theories exist, but it is believed turbulence may be key to understanding how magnetic energy is cascaded, heating plasma to observed $>10^6$K temperatures. Observations have indicated the presence of magnetohydrodynamic waves in the lower corona from measurements of non-thermal velocities revealing possible facilitation of the propagation of energy through Alfvén waves. However, it remains a challenge to arrive at an explanation as to how energy is transported from the inner Sun to the corona and dissipated there.

This thesis examines the interaction of turbulence-driven Alfvén waves in quiescent (steady-state) coronal loops by using a 1D two-fluid model. This allows us to analyse the extent to which magnetohydrodynamic waves and a turbulent cascade may be responsible for the observed heating phenomenon in the corona. The cascade transports energy from low to high frequency Alfvén waves where direct dissipation by plasma is possible. The dissipation of high frequency waves may produce asymmetric heating and drive plasma flow in coronal loops. A rigorous parameter study is conducted so a comprehensive picture of plasma characteristics is found.

The method described in this work focuses on wave dissipation being the *only* driving force behind the coronal loop heating so comparisons can be made with other research. With this assumption in mind, a range of coronal loops are simulated. On comparison with classical hydrostatic theory, it is found that both *overdense* and *underdense* loops are commonplace when assuming plasma flow and wave dissipation as the only heating mechanism. Solutions that satisfy the characteristics of X-ray and extreme ultraviolet emission loops are present. Generally, short loops are overdense ($n > 10^9\text{cm}^{-3}$) and cool ($T < 1$MK). Long loops are underdense ($n < 10^9\text{cm}^{-3}$) and hot ($T > 1$MK). Many heating profiles exist when simulating wave dissipation. Isothermal coronal loops are generated by non-uniform heating rates and hot loops (with a temperature maximum at loop apex) are generated by uniform heating. However, loop inclination appears to be a key factor limiting the implication of wave heating in isothermal loops after consideration of the balance between wave and gravitational energy fluxes. Significant non-equilibrium (a temperature difference between protons and electrons) exists for loops driven by Alfvén waves of large driving scales (causing low densities) and when driven by waves of very low driving scales (causing an energetic 'overshoot' in proton temperature). Shocks in the downflowing section of the loop are found to be a direct consequence of rapid wave heating in a localised region above the upflowing footpoint and low temperatures at the loop apex. The characteristics of transition region 'moss' are modelled for hot loops, also a consequence of rapid wave heating.

For my parents, sister and grandparents
for their unwavering and loving support

Acknowledgements

This work would not have been possible without the excellent supervision of Dr Xing Li. His patience, support and belief in my abilities as a scientist gave me the confidence of free thought and often creative ideas to complete this PhD. Thanks also to Dr Bo Li for his kind advice, patience and help with some tricky conceptual issues. Thank you to ALL the members of the Solar Physics group and the Institute of Mathematical and Physical Sciences (who could have kicked me out at the end of funding but didn't!). My office mates past and present all deserve a big thank you for their friendship and many entertaining moments in the office. I will also remember the recently deceased Jimbob and Tiny the office goldfish, essential members of Room 106.

Too many people to list provided help behind the scenes in the past 4 years, but these people and organisations spring to mind: Thanks to Dan Le Messurier for being a great mate, introducing me to the great stress-reliever, Muay Thai (Thai boxing) and beer; Ricky Sims for giving me the motivation to start and stick with the ups and downs of PhD life and for the excellent LaTeX template this thesis is based on; Richard Jones, Andy Rayment, Michael Russell, Katherine Dewis, Leslie Le Messurier, Mario Bisi and all my friends in Aberystwyth, Llanbadarn Campus and back home in Bristol who have touched my life over the years; Shadia Habbal and Huw Morgan at the Institute for Astronomy (IfA) in the University of Hawaii for inviting me to the United States to carry out research with the group, an inadvertently life-changing trip; Caz Tricks and Dylan Sawyer from the wardening team and all the portering staff who have helped, entertained and been lovely friends during my time as Assistant Warden and Senior Resident on Llanbadarn campus; Graham Parton for help and advice on the subtleties behind IDL; Huw Evans and Tarlochan Virdi for their computer support; all members past and present of the UWA Volleyball Club; all the members of Petch Yin Dee Muay Thai Aberystwyth Camp; the NASA Abstract Data Service (ADS) which was used extensively throughout this research; and my A Level physics teacher Dan Buckley, who (in 1997) sparked my enthusiasm for astrophysics in the first place!

This thesis is dedicated to Mum, Dad, my sister Colette and my grandparents. Their support, love and belief in me have made me the person I am today, this thesis would not have been a possibility without them.

And a very special thank you to my loving girlfriend Debra who has given me the vision and motivation to complete this thesis so we can begin planning for a bright and exciting future together.

Contents

List of Figures

List of Tables

Every great advance in science has issued from a new audacity of the imagination.

- from 'The Quest For Certainty', John Dewey (1859-1952)

Chapter 1

The Sun

1.1 Introduction

The Sun governs our solar system. It may be an average, medium-size star when compared with the billions of stars in the cosmos, but from our perspective the Sun is an inspiring, complex giant in our skies. The Sun influences everything in the Solar System, from the orbit of the planets to life on Earth, its energy is key to everything we know and understand. Energy flows from the solar interior to interplanetary space via a chain of transportation mechanisms eventually reaching the Earth as visible light. To pursue a better understanding of the Sun and its transmission of energy into space, the *solar corona* has become a focus for intense study.

The corona is a hot, tenuous atmosphere. The light we see with the naked eye from the solar disk, or the photosphere, radiates in optical wavelengths (λ=400-700nm) at temperatures of 4300-7500K. The light from the photosphere totally obscures the weak coronal scattered light. During an eclipse however, the corona will appear as a bright and structured atmosphere. Ancient accounts of coronal observations are documented during total solar eclipses by Chinese astronomers as long ago as 2800BC and by Baby-

lonian astronomers in 1063BC. In the late 19th century, a new element was thought to have been discovered through spectroscopic observations of the Sun. Christened "coronium", this new element was in fact a highly ionised form of iron (FeXIV) heated to a staggering 1 million Kelvin (Erdélyi, 2005). The discovery of this fact spawned the beginning of what is now known as the *coronal heating problem*.

In recent years the coronal heating problem continues to dog solar physicists. Existing at temperatures in excess of 10^6 Kelvin (or 1MK), the solar corona seems to defy basic thermodynamic laws. The solar interior has temperatures ranging from 15MK in the core, to 6000K at the photosphere (Lang, 2001). From the chromosphere to the corona, the temperature of solar plasma jumps to above 1MK over a very small distance (Mariska, 1992). This thin region of temperature increase is known as the *transition region* and can range from tens to hundreds of kilometres thick. An analogy of this would be a light bulb heating the air surrounding it hotter than its glass surface. The second law of thermodynamics would be broken. So, what mechanism is heating the tenuous coronal plasma to these temperatures?

This chapter will explore the Sun's interior, to its surface and high into the corona, detailing core energy production, energy transfer through the solar body and some of the instrumentation used to observe the solar environment. From this starting point a broad introduction to the Sun will lead to detailed study of wave heating as the possible mechanism driving the corona in the hope of providing an answer for the mystery heating mechanism (Chapter 2). Section 1.2 will begin in the solar core where fusion generates the necessary energy and will briefly explain how this energy is transmitted through the radiative zone and into the convection zone where plasma is convected and energy transferred to the photosphere. How magnetic flux is generated and convected to the solar surface will also be detailed. Section 1.3 will describe the chromosphere and transition region and how they act as an important reservoir of energy to feed the

dynamic corona. Section 1.4 will investigate the corona and magnetic field configuration. Section 1.5 details the armada of observational space missions past and present that are contributing to our understanding of the solar corona. Finally, Section 1.6 will give a brief overview of some of the main (and most important) results to come from coronal loop analysis.

1.2 The Solar Interior

The Sun is our closest star. It produces almost all the energy in our Solar System, fusing light elements into progressively heavier matter. The solar interior is also structured and highly dynamic (Fig. 1.1). As it is so close to the Earth (1AU or 1.496×10^{13}cm), the Sun is an ideal laboratory for us to study solar phenomena in great detail. The solar body has a mass of $M_{\odot}$=1.989×10^{33}g and a radius of $R_{\odot}$=6.955×10^{10}cm (Lang, 2001).

The Sun's source of energy is fusion maintained by gravitational pressure. In the solar core, the temperature is approximately $T_{\odot}$=15MK with a density of around $\rho_{\odot}$=150g cm^{-3}. At this temperature and density, the solar plasma will undergo fusion. Protons are stripped of their associated electrons under intense pressure to form a 'soup' of charged particles where hydrogen (the most abundant element in the known Universe) fuels the fusion within the core. Solar plasma is considered to be quasi-neutral (the net charge = 0) as there are roughly equal numbers of electrons and protons in a given volume. The energy liberated from such a reaction drives the solar environment and consequently makes our star shine. The process of fusing hydrogen nuclei is known as the proton-proton chain. Once four protons have joined, a helium nucleus is the result, consisting of two protons and two neutrons. The three steps of the proton-proton chain are detailed in Fig. 1.2.

A secondary process involving 14% of the light helium (^{3}He) fusing with heavier helium

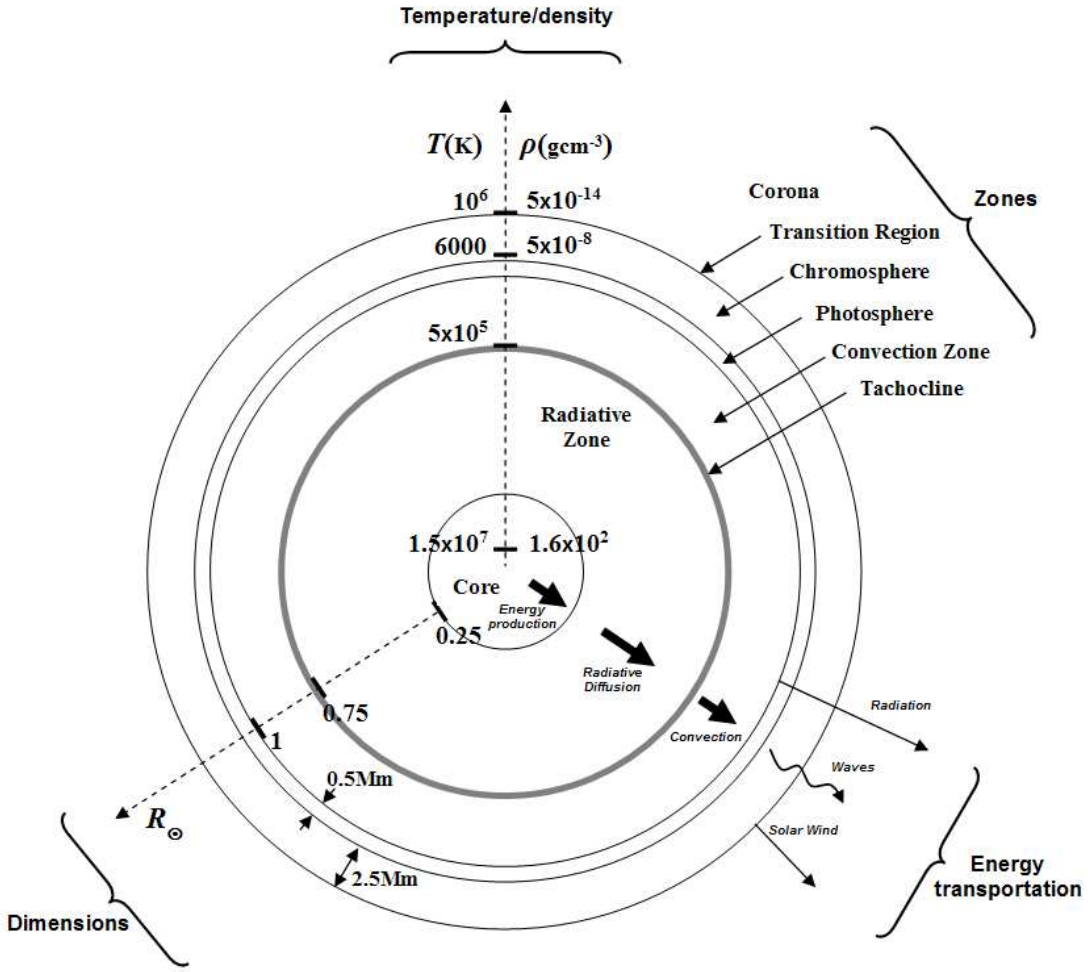

Figure 1.1: The solar interior is divided into 6 distinct layers or zones. The core is the source of energy where fusion heats the dense plasma to around 15MK. Energy is transported into the radiative zone where radiative diffusion allows energy to pass to the higher levels. The convection zone is heated from the base, allowing convection currents to flow to the surface. Supergranulation cells in the photosphere are produced by highly dynamic plasma flows. Sunspots are also evident as magnetic flux emerges through the surface. The photospheric temperature drops to around 6000K. Immediately above the photosphere, the chromosphere and transition region undergoes rapid heating over a very short distance. Plasma temperature jumps three orders of magnitude to well over 1MK as the solar plasma reaches the corona. Diagram based on Kivelson & Russell (1995) and Lang (2001)

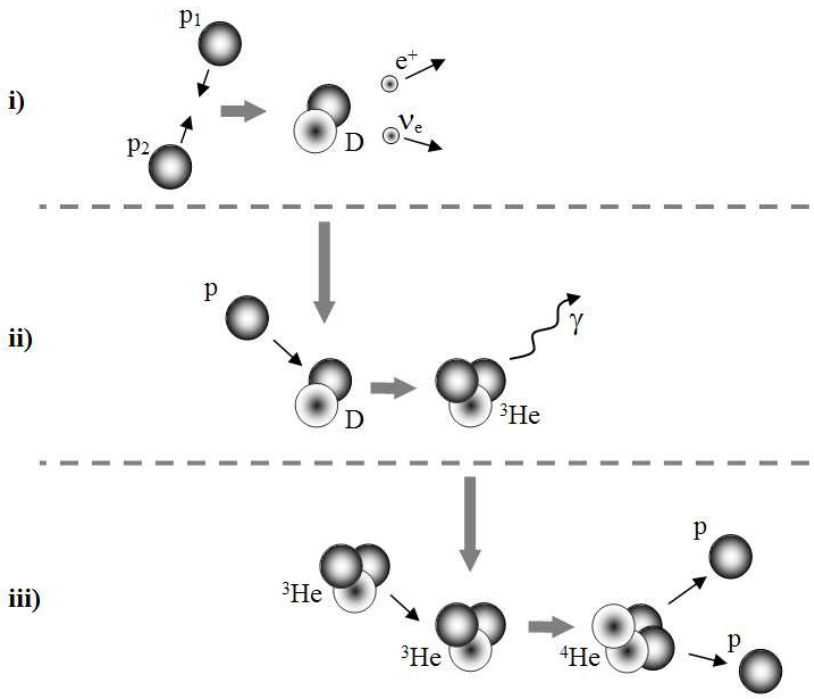

Figure 1.2: The proton-proton chain comprises of 3 stages. *i*) Two hydrogen nuclei (p_1 and p_2) are forced together to form a deuteron (deuterium nuclei), emitting a positron (e^+) and an electron neutrino (ν_e). *ii*) A helium isotope (^{3}He) is created after the collision of another proton, producing gamma radiation (γ). *iii*) In the final stage, two ^{3}He nuclei combine to form a ^{4}He nuclei, kicking off two protons in the process. Not all particles in the solar core are able to undergo the proton-proton chain, only the more energetic particles participate in this rare process. Diagram based on Lang (2001).

(^{4}He) will go on to eventually form beryllium (^{8}Be). Although its contribution to the total energy production of the Sun is small, this process is important when studying electron neutrino emissions as the ν_e released in this case is far more energetic than the ν_e emitted in the proton-proton chain (and has implications for the *solar neutrino problem*). Further details on these reactions can be found in Lang (2001).

Photons emitted from the core cannot directly travel from the Sun's centre to the surface. Light, in a vacuum, has a velocity of c=3×10^{10}cm s^{-1} and from solar core to the surface would take 2.3 seconds to travel. However, the gamma rays produced in the hot core cannot travel more than 0.09cm without colliding with the opaque matter of the radiative zone. A series of scattering events causes energy to be leached from the photons as they

slowly make their way through the solar body, slowly decreasing their frequency. It can take several million years for photons to travel from the core to the photosphere as they undergo a "random walk" (Carroll & Ostlie, 1996), constantly being scattered and deflected. In this time, photon energy will decrease from gamma radiation, to X-ray and then toward visible frequencies as observed in the photosphere. Therefore, the light we see escaping from the photosphere was produced in the solar core millions of years ago. The only detectable tracers that can be observed within minutes of their creation in the solar core are the weakly interacting neutrinos produced by hydrogen and helium fusion (Fig. 1.2i).

Radiation is the dominant energy transfer mechanism within the radiative zone. Matter from the core to $0.75R_{\odot}$ remains relatively static. This is due to the high temperatures maintaining the matter in a plasma state. Plasma will readily absorb and re-emit electromagnetic radiation, so there can be no storage of energy and net motion of the plasma. In the cooler convection zone however, electrons are able to re-combine with the plasma. Atomic bonds are far more efficient at storing energy from radiation. Radiation cannot penetrate this barrier. The energy collected by the dense gas must therefore be transported down the temperature gradient by other means. Dynamic convection cells carry hot plasma toward the photosphere, where the plasma cools and sinks back into the solar body again. Convection zone plasma is continuously heated from the base (by the radiative zone) and energy is transported to the solar surface where the energy can be released. Convection cells form intricate patterns of granulation and groups of granulation known as *supergranulation* (see Fig 1.5).

The boundary between the radiative and convection zones is widely believed to be the dynamic layer where magnetic flux is generated. Dynamo theory governs the magnetic field production (Parker 1955 and Bray *et al.* 1991). Put simply, the differential (non-uniform) rotation of the convection zone interacts with the uniform rotation of

the radiative zone, producing magnetic flux which feeds into the upper reaches of the solar body. The *tachocline* (Gough & McIntyre, 2001) indicates the layer of dynamo production in Fig. 1.1.

The differential rotation in the convection zone continually winds-up the magnetic flux as it rises toward the solar surface. As the Sun reaches *solar maximum*, the magnetic field is at its most stressed state, wrapped around the solar equator. It is during this period that the magnetic field is most deflected from its basic dipole configuration (see Figs. 1.3 and 1.4). Sunspot population can be expected to rise at this time. Solar flares and Coronal Mass Ejections (CMEs) may also result from this intense twisting of the solar magnetic flux (due to high occurrences of collisions between opposite polarity flux reconnecting). It can be expected that the solar wind configuration will become more chaotic, the fast wind (coronal holes) shifting from its normal polar configuration and the slow wind (streamer belt) shifting from its equatorial regions.

As magnetic flux emerges through the photosphere and chromosphere, the top layers of plasma are pushed aside to expose the cooler convection zone plasma. The evacuation of the plasma in the magnetic flux region leads to a buoyancy force which lifts the magnetic field up to the less dense regions of the solar interior. Buoyancy is the result of the simple pressure balance equation, $p_i + B^2/8\pi = p_e$, where p_i and p_e are the internal and external pressures respectively and $B^2/8\pi$ is the associated magnetic pressure (Golub & Pasachoff, 1997). Dark spots, or sunspots, can result.

Figure 1.5 is a high resolution image of a sunspot. The sunspot consists of two very distinct parts, the innermost umbra (darkest, radiating at a temperature of 2200K) and outermost penumbra (less dark, radiating at a temperature of 3000K). Sunspots have lifetimes in order of hours, days, weeks and even months and the solar population of sunspots depends on the time of the solar cycle and solar latitude. Sunspots can usually be observed in pairs, each at opposite polarities, one leading and one trailing.

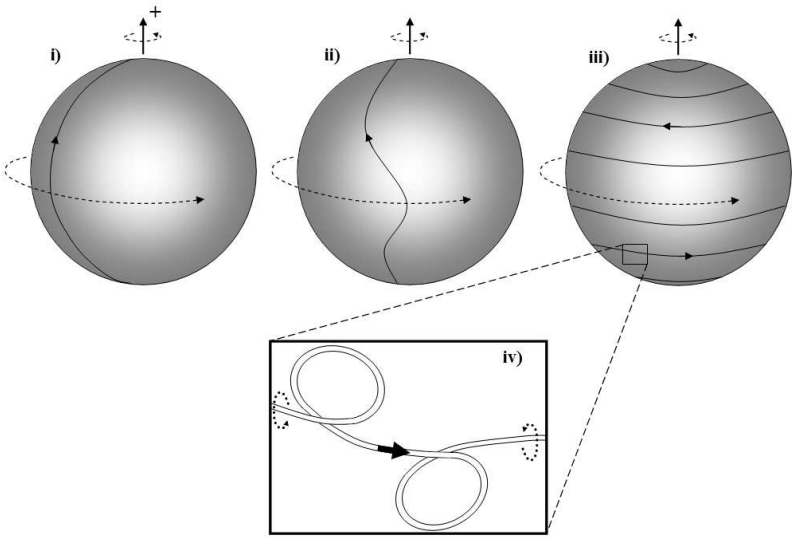

Figure 1.3: Differential rotation of the Sun. The undisturbed, bipolar magnetic field configuration during solar minimum marks the start of the solar cycle (*i*). The faster rotation at the solar equator then *drags* the magnetic field around the solar body (*ii*) until the Sun approaches solar maximum where the buoyant magnetic flux is twisted to such an extent flares and highly dynamic coronal loops become commonplace across the Sun's surface (*iii and iv*).

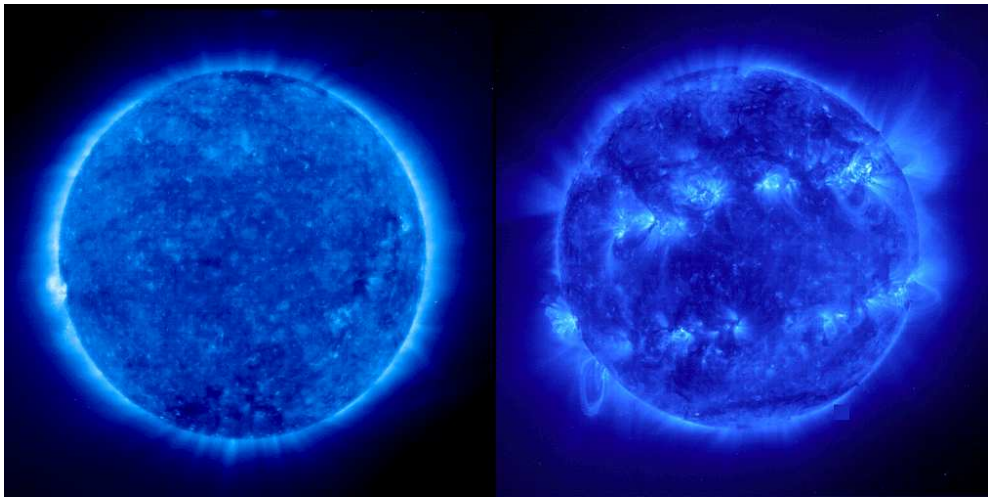

Figure 1.4: Two *SOHO* (EIT) 171Å images (two years apart) demonstrating the increase in solar activity. The image on the right clearly shows the increase of coronal loop activity due to the differential rotation *dragging* the magnetic field around the solar body (see Fig. 1.3). Source: `http://sohowww.nascom.nasa.gov/`

The proportion of the sunspot structure covered by umbrae and penumbrae depends on scale and lifetime. The penumbra may cover the majority of the spot, leaving a tiny central umbra, or the umbra may dominate (small, umbra dominating sunspots are known as 'pores'). The penumbra will often have highly structured and dynamic filamentation projecting downwards, toward the umbra.

The period from solar minimum to solar maximum lasts approximately 11 years. The polarity of the Sun's magnetic field then switches as the solar cycle reaches solar maximum, quickly followed by a period of calm before the whole process begins again. Therefore the complete solar cycle (time for two polarity 'switches') lasts approximately 22 years. It can be expected that the sunspot population will be at its highest during solar maximum. Figure 1.6 demonstrates the periodicity of the solar cycle in the form of a "butterfly diagram". By plotting the distribution of sunspots with solar

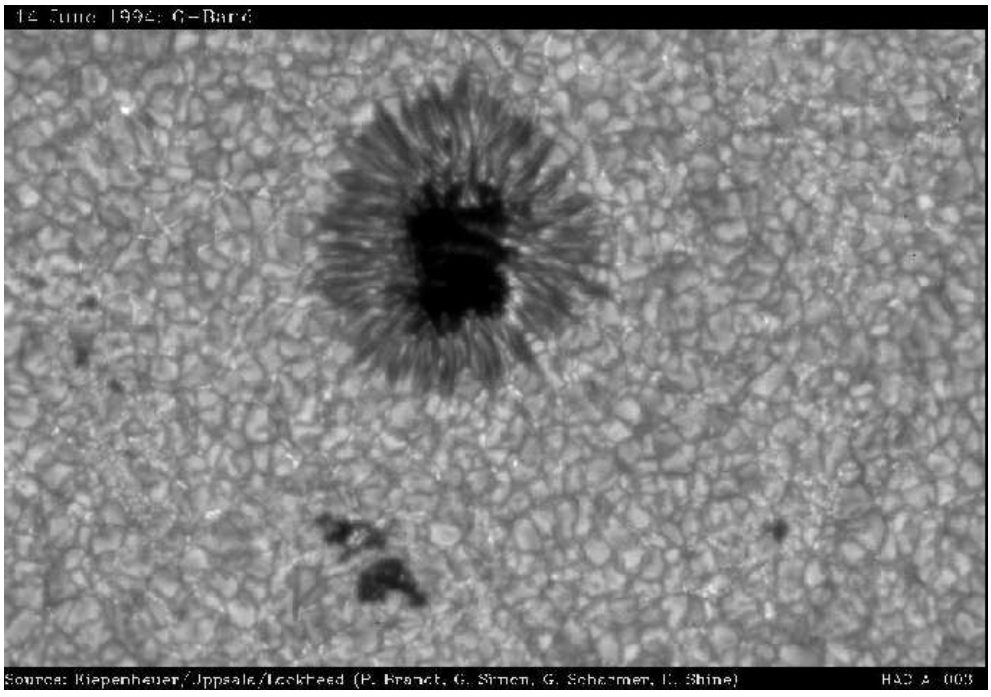

Figure 1.5: A high-resolution image of a sunspot, viewed with a 4305Å filter from the *High Altitude Observatory* (*HAO*) in Boulder, Colorado (USA). Detail of the sunspot's umbra and penumbra can be seen with obvious granulation patterns covering the surrounding area. The field of view of is 60000×38000km. Source: `http://www.hao.ucar.edu`.

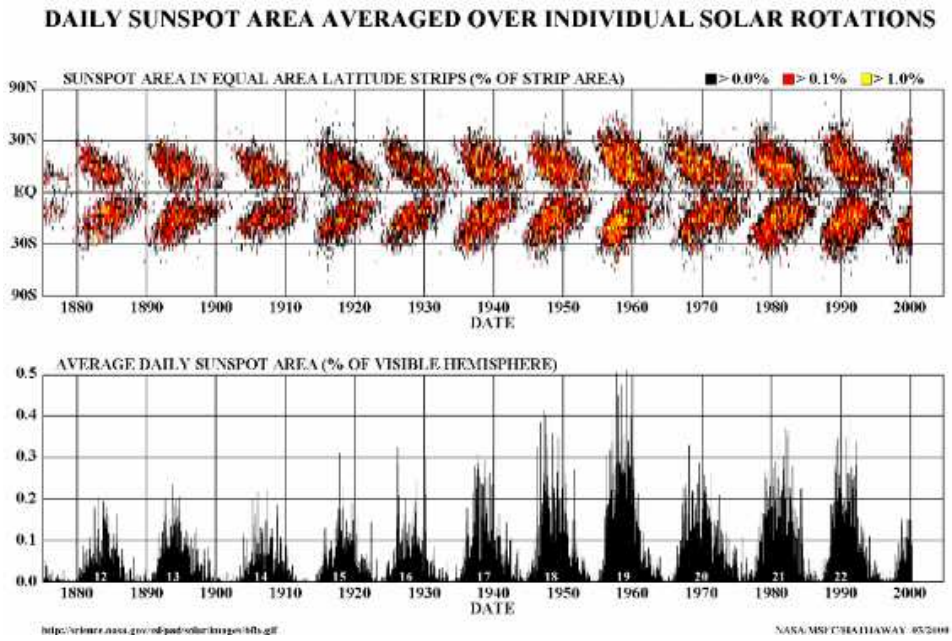

Figure 1.6: The butterfly diagram. The top panel represents the proportion of the solar surface covered by sunspots against latitude and the bottom panel is the average daily sunspot area observed on the Sun. In this case, observations dating back to 1880 are presented. Source: `http://science.nasa.gov`.

latitude, a pattern resembling that of butterfly's wings develops. From the top panel it can be deduced that as the solar cycle progresses, the sunspot distribution drifts toward the solar equator until solar maximum is reached after 11 years of activity.

Regardless whether the Sun is at minimum or maximum activity, the chromosphere has many observable features of interest. Huge loops of magnetic flux can often be found expanding into the corona trapping cool plasma. On the limb of the Sun these prominences will appear bright and highly structured. If observed in the disk, prominences will appear dark against the photospheric emission. Prominences observed in this manner are commonly known as filaments. On a smaller scale, jets of upflowing material, supported by magnetic flux, can be observed. These jets can reach many hundreds of kilometers above the photosphere, whereas prominences extend to the order of solar radii.

1.3 The Chromosphere and Transition Region

The solar transition region separates the cool chromosphere from the hot corona. All energy and matter that feeds the corona passes from the chromosphere and through the transition region. The chromosphere has a temperature of approximately 20,000K and lies above the photosphere. The transition region, very thin in comparison to the solar corona, appears almost as a discontinuity and separates the dense chromosphere from the tenuous corona. There is a sudden transition from neutral matter to highly ionized plasma and plasma temperature jumps three orders of magnitude. The mystery energy source must be powerful enough to rapidly energize solar plasma over a very small distance and pass through a transparent photosphere and chromosphere (Mariska, 1992). Figure 1.7 illustrates this dynamic region by plotting the average temperature-density model distribution for the quiet chromosphere and transition region (i.e. away from coronal holes and active regions). In this model, the photosphere extends from 100km to the temperature minimum (the dip in temperature profile at a height of 600km). In a purely radiative-convective solar atmospheric model the temperature would continue to decrease (as one would expect), but instead there is a sudden rise in temperature and drop in density indicating some form of nonradiative and/or momentum deposition mechanism. The generally accepted lower boundary of the chromosphere is at the temperature minimum, just above the photosphere.

The boundary between chromosphere and transition region is easy to define in Fig. 1.7. The temperature of the lower boundary of the transition region is approximately 25,000K (immediately above the step in temperature profile at around 20,000K). A temperature of 1MK is used by Mariska (1992) to define the lower limit of the coronal interface between corona and high transition region. Beyond 1MK, the heating becomes less intense, giving way to an increasingly isothermal corona. The height of the transition region is not uniform for the entire solar atmosphere. The height of the transition

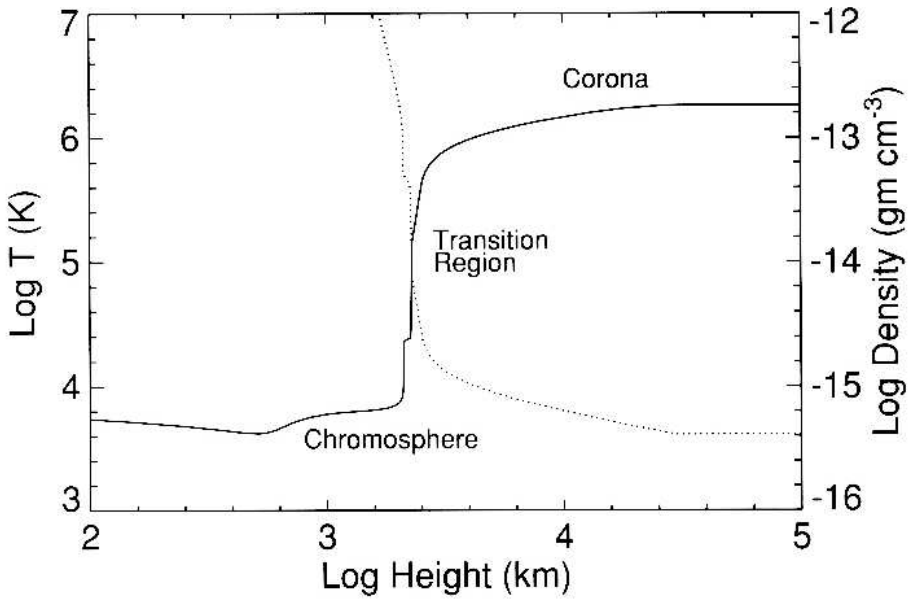

Figure 1.7: The chromosphere and transition region. Average temperature (*solid line*) and density (*dotted line*) structure of the chromosphere, transition region and corona (quiet conditions). From Mariska (1992).

region boundary may decrease over coronal holes and increase over active regions for example.

One of the most important forms of energy transfer/excitation in the transition region and chromosphere is collisional. As stated by Lenz (1999), the *Debye Length* is small in lower coronal regions (~1cm). Radiative forms of excitation are rare due to the lack of a strong radiative field at the wavelengths of important transition region ions (Mariska, 1992). The physics of Coulombic interactions are therefore incorporated in the model proposed in this thesis (Eq. 3.8 demonstrates the application of Coulombic interactions).

1.4 The Corona

The extended corona is obvious during total solar eclipses. During totality the corona will appear as a beautiful, bright and extended atmosphere reaching several solar radii into space. In the simplest view of the lower corona, magnetic flux falls into one of two

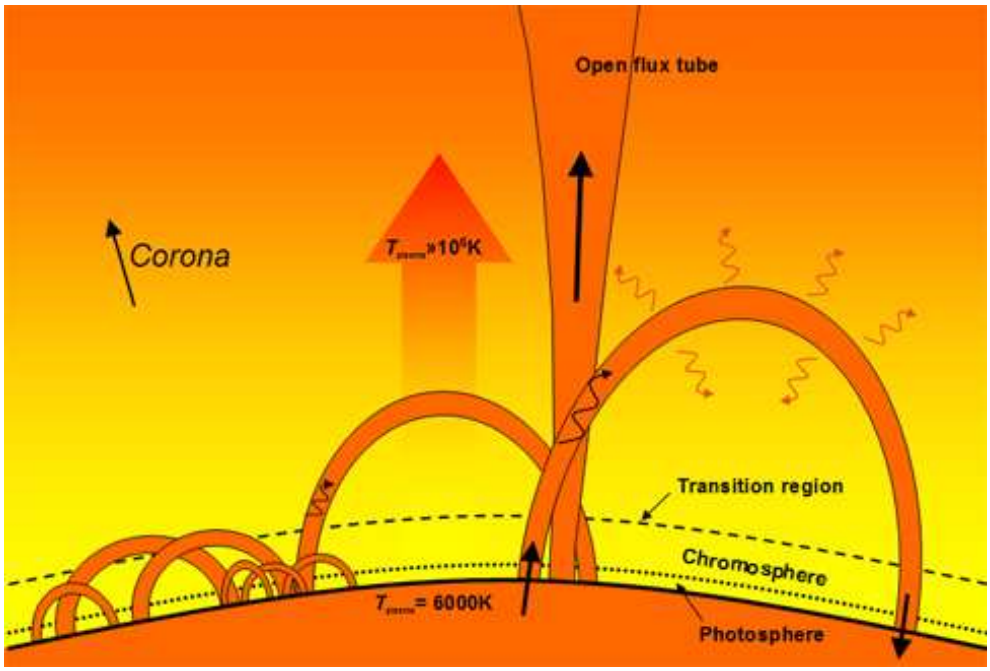

Figure 1.8: A cartoon generalising the region of interest. Many scales of coronal loop co-exist alongside open flux tubes. The loop footpoints are assumed to be anchored in the photosphere and penetrate the chromosphere, transition region and corona. Bold arrows represent possible plasma flow; black wavey lines represent possible wave propagation; orange lines represent plasma radiation.

categories. Magnetic field lines are either *open* or *closed* (Fig. 1.8). As magnetic flux is inextricably linked (or *frozen-in*) with solar plasma, both open and closed flux channel plasma away from the chromosphere. Open field lines are known to be the source of the solar wind, whereas closed lines form intricate loops of coronal matter trapped at low altitudes. Generally open field lines contain high velocity, tenuous plasma and closed field lines contain dense, strongly radiating plasma.

1.4.1 Open Field: The Solar Wind

The solar wind is characterised as a constant flow of plasma from the chromosphere into interplanetary space. Known to be *bi-modal*, the solar wind consists of two distinct streams. The *fast* solar wind (Neugebauer & Snyder, 1962) travels at velocities of between 700-900kms^{-1} (Axford & Mckenzie, 1997) and is associated with open magnetic

flux (i.e. coronal holes located in polar regions). The *slow* solar wind (Habbal *et al.*, 1997) travels at velocities of between 300-400kms^{-1} and is located above equatorial closed magnetic flux regions (i.e. the streamer belt).

1.4.2 Closed Field: Coronal Loops

In contrast, a coronal loop is magnetic flux fixed at both ends, threading through the solar body, protruding into the solar atmosphere. They are ideal structures to observe when trying to understand the transfer of energy from the solar body, through the transition region and into the corona. The cartoon in Fig. 1.8 generalises the region of interest. Many scales of coronal loops exist, neighbouring open flux tubes that give way to the solar wind and reach far into the corona and heliosphere. Anchored in the photosphere (a rigid, *line-tied*, anchor is assumed where the high-β external plasma holds the loop footpoints in place), coronal loops project through the chromosphere and transition region, extending high into the corona.

Also, coronal loops have a wide variety of temperatures along their lengths. Loops existing at temperatures below 1MK are generally known as *cool loops*, those existing at around 1MK are known as *warm loops* and those beyond 1MK are known as *hot loops*. Naturally these different categories radiate at different wavelengths. Vourlidas *et al.* (2001) categorises these loop temperatures with associated observing band passes (refer to Fig. 1.9). Observational band passes are described in Section 1.5.

Coronal loops populate both active and quiet regions of the solar surface. Active regions on the solar surface take up small areas but produce the majority of activity and are often the source of flares and CMEs due to the intense magnetic field present. Aschwanden (2001) states that active regions produce 82% of the total coronal heating energy. Coronal holes are open field lines located predominantly in the polar regions of

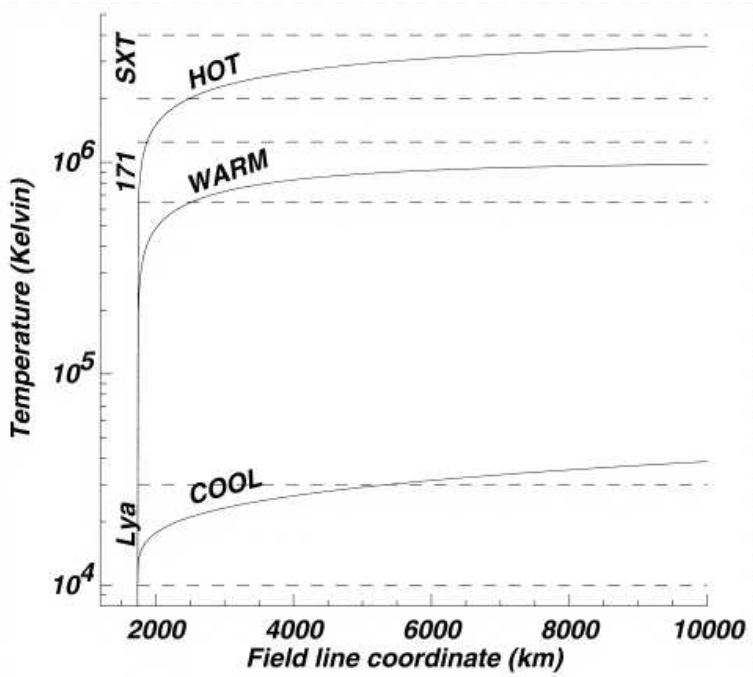

Figure 1.9: Coronal loop temperature and the associated *TRACE* band passes. The terms *cool* (<1MK), *warm* (≈1MK) and *hot* (>1MK) loops are used throughout this thesis (Vourlidas *et al.*, 2001).

the Sun and are known to be the source of the fast solar wind. The quiet Sun makes up the rest of the solar surface. As stated by Aschwanden (2004), the quiet Sun, although less active than active regions, is awash with dynamic processes and transient events (bright points, nanoflares and jets). As a general rule, the quiet Sun exists in regions of closed magnetic structures, active regions are highly dynamic sources of explosive events.

It is important to note that observations suggest the whole corona is massively populated by open and closed magnetic fieldlines. A closed fieldline does not constitute a coronal loop however, closed flux must be filled with plasma before it can be called a coronal loop. With this in mind it becomes clear that coronal loops are a rarity on the solar surface as the majority of closed flux structures are *empty*. This means the mechanism that heats the corona and injects chromospheric plasma into the closed magnetic flux is highly localised (Litwin & Rosner, 1993). The mechanism behind plasma fill-

ing, dynamic flows and coronal heating remains a mystery. The mechanism(s) must be stable enough to continue to feed the corona with chromospheric plasma and powerful enough to accelerate and therefore heat the plasma from 6000K to well over 1MK over the short distance from chromosphere, transition region to the corona. This is the very reason coronal loops are targeted for intense study. They are anchored to the photosphere, are fed by chromospheric plasma (Aschwanden, 2001), protrude into the transition region and exist at coronal temperatures after undergoing intensive heating.

The idea that the coronal heating problem is solely down to some coronal heating mechanism is misleading. Firstly, the plasma filling overdense loops is drained directly from the chromosphere. There is no coronal mechanism known that can compress coronal plasma and feed it into coronal loops at coronal altitudes. Secondly, observations of coronal upflows (Saba & Strong, 1991, Spadaro *et al.*, 2000, Winebarger *et al.*, 2002) points to a chromospheric source of plasma. The plasma is therefore chromospheric in origin, there must be consideration of this when looking into coronal heating mechanisms. As pointed out by Aschwanden (2001), this is a *chromospheric energization* **and** *coronal heating* phenomenon possibly linked through a common mechanism.

1.5 Observing Coronal Loops

Many strides have been made by ground-based telescopes (such as the *Mauna Loa Solar Observatory, MLSO,* in Hawaii; MacQueen *et al.* 1998) and eclipse observations of the corona, but to escape the obscuring effect of the Earth's atmosphere, space-based observations have have become a necessary evolution for solar physics. Beginning with the short (7 minute) Areobee rocket flights in 1946 and 1952, spectrograms measured solar EUV and Lyman-α emissions (Aschwanden, 2004). Basic X-ray observations were at-

tained by 1960 using such rockets. The British *Skylark* rocket missions from 1959-1978 also returned mainly X-ray spectrometer data (Boland *et al.*, 1975). Although successful, the rocket missions were very limited in lifetime and payload. During the period of 1962-1975, the satellite series *Orbiting Solar Observatory* (*OSO-1* to *OSO-8*) were able to gain extended EUV and X-ray spectrometer observations. Then in 1973, *Skylab* was launched and began a new multi-wavelength campaign which typified future observatories (Vaiana *et al.*, 1973, Bray *et al.*, 1991). This mission only lasted a year and was superceded by the *Solar Maximum Mission* (Strong *et al.*, 1999) which became the first observatory to last the majority of a solar cycle (from 1980-1989). A wealth of data was accumulated across the whole range of emission.

The solar community was rocked by the launch of *Yohkoh* (Solar A) from Kagoshima Space Centre (Southern Japan) in August 1991. It was lost on 14th December 2001 due to battery failure, but revolutionised X-ray observations in its decade of operations. *Yohkoh* (or 'Sunbeam') orbited the Earth in an elliptical orbit, observing X-ray and gamma-ray emissions from solar phenomena such as solar flares. *Yohkoh* carried four instruments. The Bragg Crystal Spectrometer (BCS), the Wide Band Spectrometer (WBS), the Soft X-Ray Telescope (SXT) and the Hard X-Ray Telescope (HXT) were operated by a consortium of scientists from Japan, USA and UK. Of particular interest is the SXT instrument for observing X-ray emitting coronal loops.

The SXT instrument observed X-rays in the 0.25-4.0keV range, resolving solar features to 2.5 arc seconds with a temporal resolution of 0.5-2 seconds. SXT was sensitive to plasma in the 2-4MK temperature range (as demonstrated in the full-disk image in Fig. 1.10), making it an ideal observational platform to compare with data collected from *Transition Region And Coronal Explorer* (*TRACE*) coronal loops radiating in the EUV wavelengths (Aschwanden, 2002a).

The next major step in solar physics came at the launch of the *Solar and Heliospheric*

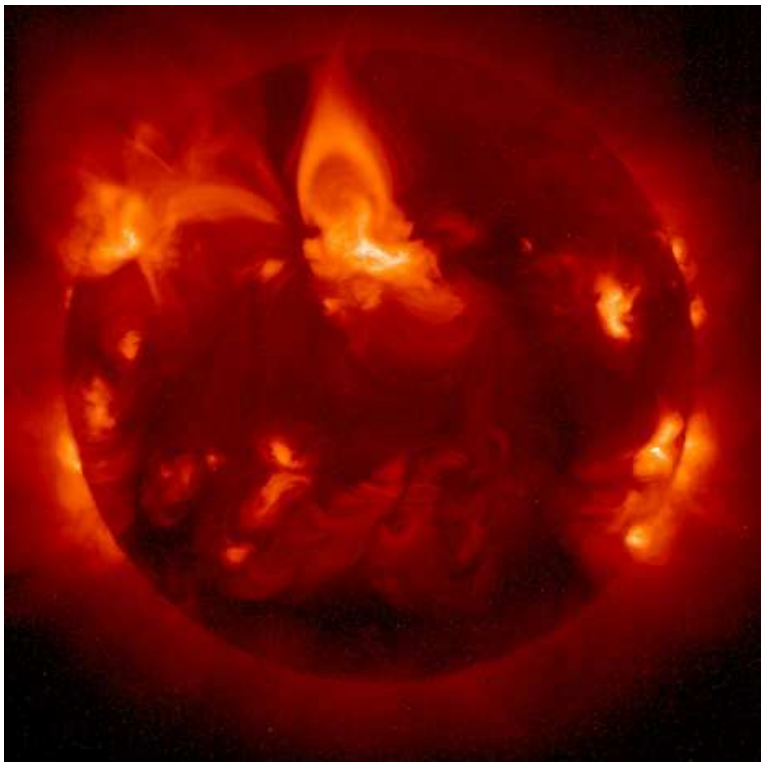

Figure 1.10: A full-disk image of the X-ray emitting Sun as observed by the SXT instrument on board *Yohkoh*. Source: `http://ydac.mssl.ucl.ac.uk/ydac/`.

Observatory (*SOHO*) in December 1995 from Cape Canaveral Air Station in Florida, USA. *SOHO* originally had an operational lifetime of two years. The mission was extended to March 2007 due to its resounding success allowing *SOHO* to observe a complete 11 year solar cycle. *SOHO* continually faces the Sun holding a slow orbit around the First Lagrangian Point (L1) where the gravitational balance between the Sun and Earth provides a stable position for *SOHO* to orbit. *SOHO* is continually eclipsing the Sun from the Earth at a distance of approximately 1.5 million kilometres.

SOHO is managed by scientists from the European Space Agency (ESA) and NASA. Comprising of more instruments than both *TRACE* and *Yohkoh*, this large solar mission was designed to look at the chain from the solar interior, the solar corona to the solar wind. *SOHO* has 12 instruments on board including the Coronal Diagnostic Spectrometer (CDS), the Extreme ultraviolet Imaging Telescope (EIT), the Solar Ultraviolet

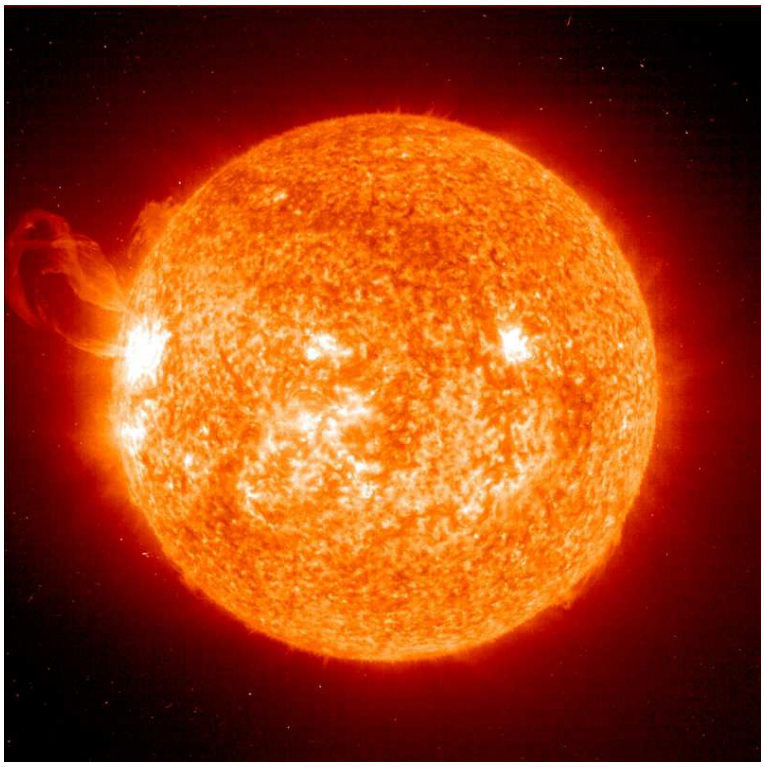

Figure 1.11: A full-disk image of the chromospheric network (304Å) as captured by the EIT instrument onboard *SOHO*. A cool solar prominence is evident to the left of the image. Source: `http://umbra.nascom.nasa.gov/eit/`.

Measurements of Emitted Radiation (SUMER) and the UltraViolet Coronagraph Spectrometer (UVCS) which are all used extensively in the study of the transition region and corona.

The EIT instrument is used extensively in coronal loop observations. EIT images the transition region through to the inner corona by utilising four band passes, 171Å FeIX, 195Å FeXII, 284Å FeXV and 304Å HeII (Fig. 1.11), each corresponding to different EUV temperatures, probing the chromospheric network (304Å at $T \sim 20,000$K) to the lower corona (171Å at $T \sim 2$MK).

The *Transition Region And Coronal Explorer* (*TRACE*) was launched in April, 1998 from Vandenberg Air Force Base as part of NASA's Goddard Space Flight Center Small Explorer (SMEX) project. The small orbiting instrument has a 30×160cm, 8.66m focal length Cassegrain telescope with a 1200×1200px CCD detector. The timing of the

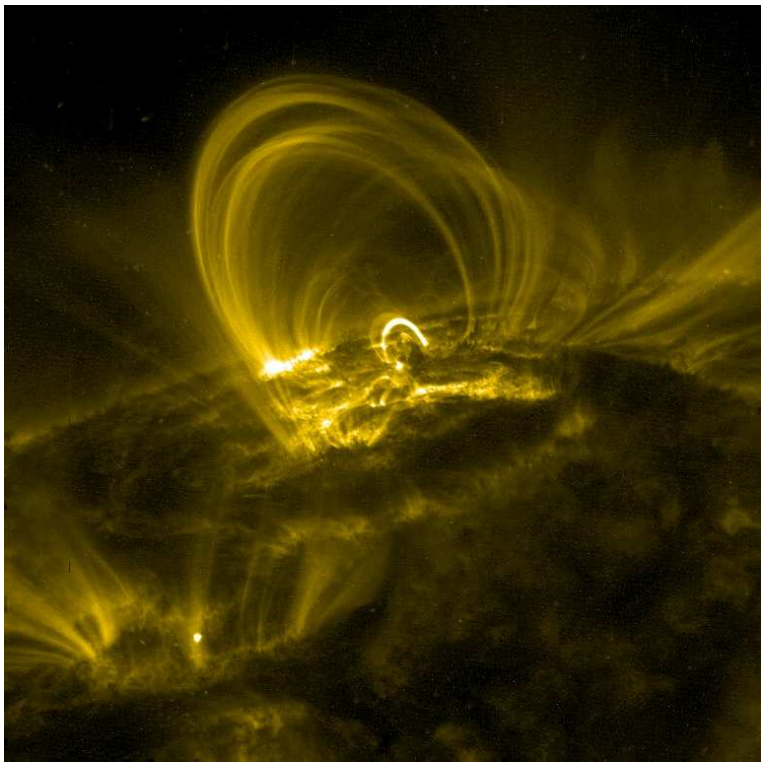

Figure 1.12: Typical *TRACE* coronal loops near the limb of the Sun viewed in the 171Å FeIX band pass. Source: `http://trace.lmsal.com/`.

launch was planned to coincide with the rising phase of the solar maximum. Observations of the transition region and lower corona could then be carried out in conjunction with *SOHO* to give an unprecedented view of the solar environment during this exciting phase of the solar cycle.

Due to the high spatial (1 arc second) and temporal resolution (1-5sec), *TRACE* has been able to capture highly detailed images of coronal structures, whilst *SOHO* provides the global (lower resolution) picture of the Sun. Figure 1.12 is such an example of the fine detail imaged by *TRACE*. Figure 1.13 is a series of images taken by *TRACE* over the course of 24 hours. This campaign demonstrates the observatory's ability to track the evolution of steady-state (or quiescent) coronal loops.

TRACE utilizes filters that are sensitive to electromagnetic radiation in the 171Å FeIX, 195Å FeXII, 284Å FeXV, 1216Å HI, 1550Å CIV and 1600Å range. Of particular

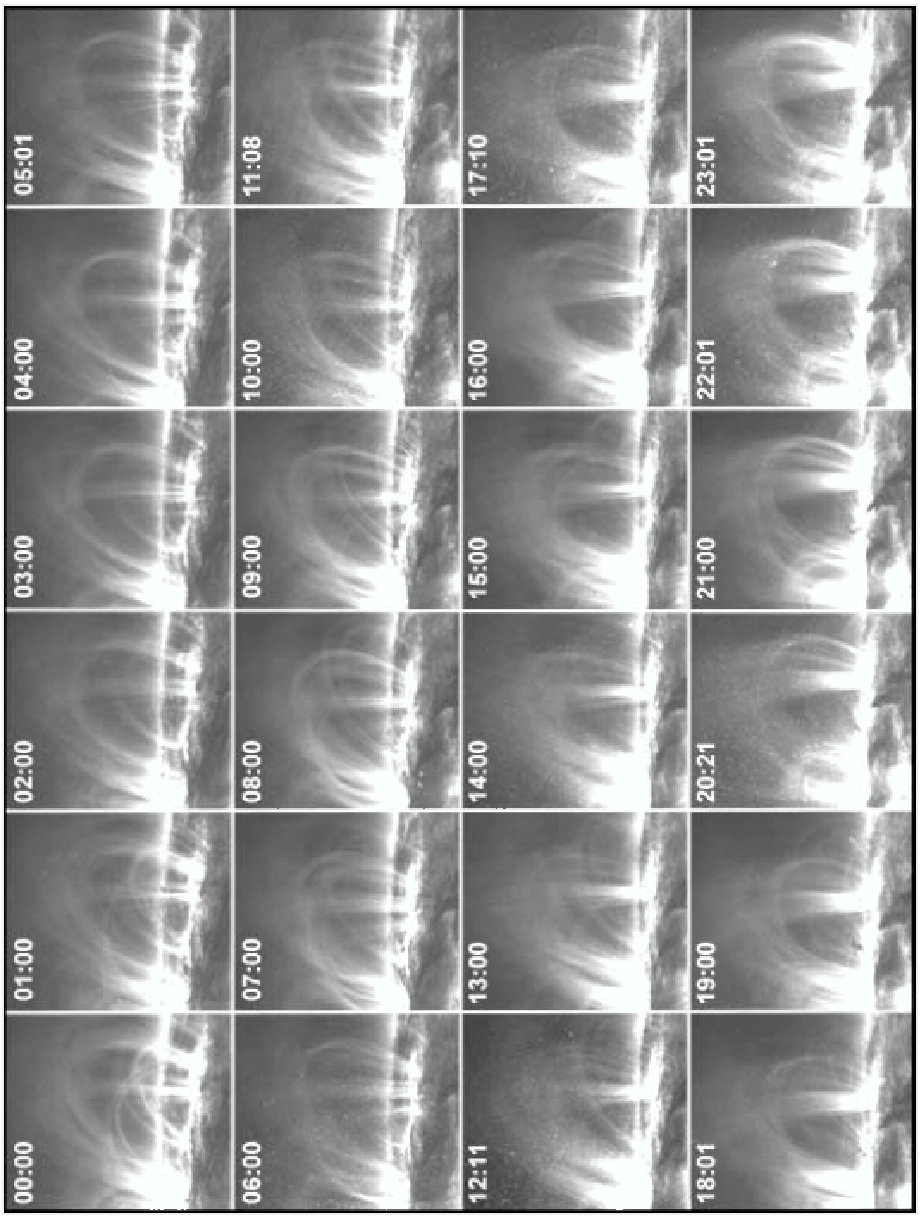

Figure 1.13: An active region as observed by the *TRACE* 171Åfilter over 24 hours on 26 July 1998 (Lenz, 2004). During this sequence of images, no appreciable change in coronal loop morphology is obvious. The loops are therefore deemed to be quiescent.

interest are the 171Å, 195Å and 284Å band passes as they are sensitive to the radiation emitted by quiescent coronal loops.

All of the above space missions have been highly successful in observing strong plasma flows and highly dynamic processes in coronal loops. For example, SUMER observations suggest flow velocities of 5 - 16kms^{-1} in the solar disk (Spadaro *et al.*, 2000), other joint SUMER/*TRACE* observations detect flows of 15-40kms^{-1} (Winebarger *et al.*, 2002). Very high velocities have been detected by the Flat Crystal Spectrometer (FCS) on board the Solar Maximum Mission where plasma velocities were found in the range of 40 - 60kms^{-1} (Saba & Strong, 1991). Dynamic coronal loops are commonplace over the solar surface in both active and quiet regions. Steady plasma flow may be a key component to these observed "overdense" loops (Winebarger *et al.*, 2002). Overdense coronal loops are structures that are observed to be several orders of magnitude more dense than expected from hydrostatic models (Rosner *et al.*, 1978, Winebarger *et al.*, 2003). The converse is true for X-ray coronal loops where the plasma density is found to be "underdense" when compared with hydrostatic models (Kano & Tsuneta, 1996).

1.6 Coronal Loop Analysis

This section will briefly outline some of the current ideas that have arisen from observations of the lower corona. Coronal loops possess a wealth of information about the fundamental properties of our star's hot atmosphere, this is why such scrutiny is applied to the interpretation of data returned from instruments described previously in Section 1.5.

Observed EUV (warm) loops are generally isothermal along their lengths (Neupert *et al.*, 1998, Lenz *et al.*, 1999, Aschwanden *et al.*, 2000a) and are heated non-uniformly. Much work has been carried out to define where heating occurs and how quickly the

mystery heating mechanism dissipates and heats the coronal loop plasma. Isothermal loops are a result of non-uniform heating (Serio *et al.*, 1981) but not of uniform heating (Rosner *et al.*, 1978). Aschwanden *et al.* (2001) states that non-uniform heating can be expected in both active and quiet Sun regions. X-ray (hot) loops on the other hand have generally been observed to have a temperature maximum at the loop apex (Kano & Tsuneta, 1996) suggesting focused heating at the loop top.

In an attempt to understand the isothermal nature of some observations of EUV coronal loops, Schmelz *et al.* (2005) carries out a study using the CDS instrument on *SOHO*. The coronal loop is observed through 12 band passes, sensitive to the wavelengths of a range of ions from the hottest (and clearest) MgIX to FeXVI. Cooler plasma can be seen emitting in the OV, NeVI and CaX band passes. These are observations of one coronal loop, suggesting loops possess a multi-thermal nature, not only along the line of sight, but along the length of the coronal loop. Many observations suggest EUV loops are in fact approximately isothermal along their coronal lengths (Lenz *et al.*, 1999), but there is a debate that suggests the analysis of coronal loop *TRACE* data may be flawed (Schmelz *et al.*, 2001, Martens *et al.*, 2002, Schmelz, 2002, Aschwanden, 2002). Warren *et al.* (2002) and Del Zanna & Mason (2003) highlight the difficulty of measuring the localised emission from coronal loops. As the observation is taken remotely, there will be contributions to the total emission along the Line Of Site (LOS). There will therefore be errors in results. It can however be argued that the overdense loop plasma is radiating sufficiently to swamp any LOS contribution by tenuous extended corona plasma.

Weber *et al.* (2005) build on work by Schmelz *et al.* (2005) and conclude that there is a statistical bias in the generally used "filter ratio method" toward isothermal temperatures along EUV loops and state the need for further coronal loop models. By disputing the commonly understood characteristic of EUV loops having isothermal structures, the

possibility of multi-thermal, non-isothermal coronal loops must be considered. In support of this, *TRACE* images show coronal loops consisting of bundled and fine strands (many small-scale, and often sub-resolution, "fibrils" of magnetic flux bundled together to form a coronal loop). Pre-*TRACE* observations have been unable to distinguish between the fine structure and large-scale emission from the loop due to a shortfall in spatial resolution. Since 1998, *TRACE* has transformed our understanding of the fine structure of coronal loops. Coronal loop fibrils are thought to have differing temperature profiles, even when coexisting in a very confined environment (Reale *et al.*, 2000, Aschwanden, 2002), so this may be an important factor to bear in mind when observing loops. For instance, Reale *et al.* (2000) model 6 thin parallel *hydrostatic* filaments. Due to minimum transmission of heat across fieldlines, each filament remains insulated from their neighbour. Once the temperature profile for each filament is summed together, a total temperature profile can be arrived at. This study finds that 6 filaments of different temperature profiles (T=0.8-5MK) can indeed produce a large-scale isothermal coronal loop remaining at approximately 1MK for the coronal section. This simple simulation may help in the understanding as to why some studies suggest non-isothermal loops and others strongly suggest isothermal loops.

Kano & Tsuneta (1995) investigates the relationship between coronal loop length, pressure and maximum temperature and find a similar scaling law to classical models (e.g. Rosner *et al.* 1978) and find similar apex heating of coronal X-ray loops (as observed by *Yohkoh*). Generally it would appear X-ray (*Yohkoh*) loops fulfill the criteria outlined by authors such as Rosner *et al.* (1978) but EUV (*TRACE*) loops do not. Winebarger *et al.* (2002) highlight the role of plasma flow around EUV loops and emphasises that loop dynamics are likely to play a very important role in any proposed heating mechanism. From previous studies it is obvious that X-ray and EUV loops have contrasting characteristics. Klimchuk *et al.* (2003) states that hot (>2MK) coronal loops as observed by *Yohkoh* are underdense (when compared with equilibrium theory) and

quasi-static whereas warm (1MK) coronal loops as observed by *TRACE* and EIT tend to be *overdense* and dynamic. The loops are found to be underdense when they are hot (as they cool primarily by conduction) and overdense when they are warm (as they cool primarily by radiation). This finding is supported by Winebarger *et al.* (2003), but suggest the two classes of coronal loop may be heated by different heating functions or indeed by different heating mechanisms (although Klimchuk *et al.* 2003 attributes both classes to nanoflare heating).

1.7 Discussion

This chapter overviews the Sun's dynamic nature by detailing how energy is generated and how it influences the evolution of coronal loops. Section 1.2 to 1.4 follows the energy transport from solar core to solar surface where the strong relationship between coronal plasma and magnetic field is introduced. Somehow the corona is heated two orders of magnitude hotter than the chromosphere (as observed by the advanced armada of observational platforms, Section 1.5), the relationship between coronal plasma and magnetic flux must therefore be investigated as a possible cause to the coronal heating problem. Coronal loops will always be the source of intense study as they are highly observable (dense and bright when compared the tenuous extended corona) and will be open to debate until *in-situ* observations are possible in the corona (Section 1.6).

Without delving into the details of data analysis, the following chapters will attempt to explain how dynamic quiescent loops may be heated by a simple hydrodynamic coronal loop model. A range of coronal loop heating profiles can be attributed to MHD wave propagation and dissipation providing some answer as to how isothermal and non-isothermal loops may be heated by the same mechanism.

Chapter 2

Alfvén Waves and Turbulence in Coronal Loops

2.1 Introduction

Coronal loops are closed magnetic structures feeding into the base of the corona providing a link from the inner Sun to the corona. The biggest issue when gaining measurements of plasma parameters in coronal loops is that there can be **no** *in-situ* measurements. All observations are taken remotely due to the extreme temperatures physically limiting the distance any solar probe can get to the Sun. Coronal loop plasma parameters are therefore open to debate. The basic parameters such as density, velocity and temperature can be measured from observables such as radiation and Doppler broadening of spectral lines, but we lack direct measurements of magnetic field strength, turbulence, electric currents and wave activity. All these parameters must be inferred from complex numerical models and solar averages, increasing the ambiguity in coronal understanding.

This chapter relates coronal observations over the years with proposed coronal heating mechanisms. The interaction between Alfvén wave and coronal loop plasma is the main focus of this thesis but a broad understanding of other mechanisms is required to com-

plete our knowledge. Section 2.2 quickly introduces Alfvén waves and their relation to other natural wave modes in coronal plasmas and overviews the mechanism of ion cyclotron resonance. Section 2.3 describes the proposed turbulent mechanism responsible for the cascade of wave energy in the solar wind and argues how it may operate in highly conductive coronal loops. Section 2.4 investigates how non-thermal velocities observed in the chromosphere and transition region may be related to MHD activity, thus providing an observable to measure Alfvén wave activity low in the corona. Section 2.5 overviews current models and observations of turbulence-driven coronal loops, highlighting the strengths and weaknesses of our current understanding of this complex issue. Section 2.6 completes this chapter by giving a brief assessment of other models and how they may influence work with the turbulent loops in this study.

2.2 Alfvén Waves and Ion Cyclotron Resonance

As one would expect, waves will readily propagate along magnetic flux. There is a range of natural wave modes present in magnetised fluids which have massive implications for the plasma parameters. One of the most fundamental and important waves to propagate in coronal plasma (and laboratory plasma alike) is the Alfvén wave (Alfvén, 1947).

Magnetosonic waves are driven by a pressure gradient and propagate in all directions. Alfvén waves are not driven by a pressure gradient and the direction of propagation is restricted by the magnetic field. Alfvén waves also do not cause density fluctuations, it is for this reason that Alfvén waves are difficult to detect. Alfvén wave propagation is given away by velocity perturbations correlating with magnetic fluctuations. Alfvén wave activity can also be detected when (in the high-frequency range) interacting with coronal particles.

An excellent review on MHD waves in the corona and the solar wind by Tu & Marsch (1995) examines early evidence of Alfvén wave activity. Belcher & Davis (1971) and Marsch *et al.* (1982) report early observations of the signature of Alfvén waves populating the solar wind. α-particles (He nuclei) were found to be moving faster than protons and the velocity difference between α-particles and protons approximated the local Alfvén velocity (known as *differential streaming*). The local Alfvén velocity (v_{A}) is given by

$$v_{\mathrm{A}} = \frac{B_0}{\sqrt{\mu_0 \rho}} \tag{2.1}$$

where B_0 is the magnetic field, μ_0 is the permeability of free space and ρ is plasma density. This suggests that solar wind ions are being preferentially accelerated. As an analogy, ions are *surfing* on propagating Alfvén waves, exhibiting a velocity difference approximating that of the wave velocity (Isenberg & Hollweg, 1983). Reisenfeld *et al.* (2001) confirms a relationship between v_{A} and $v_{\alpha\mathrm{p}}$ from *Ulysses* data, but finds $v_{\alpha\mathrm{p}}$ to be lower than v_{A}. It is important to note that $v_{\alpha\mathrm{p}}$ is closely correlated with the variations in v_{A}.

Further evidence for the existence of Alfvén waves populating the corona is provided by Ulrich (1996) where a systematic search for magnetic field oscillations is carried out. Using the Mount Wilson Observatory magnetograph (California, USA), magnetic and velocity oscillations can be measured. Ulrich finds that the 5-minute oscillations observed have typical Alfvénic characteristics and originate from the periodic shaking of coronal loop footpoints (Ionson, 1978). The phase relation between velocity and magnetic variation is very close to what would be expected for a flux of outward propagating Alfvén waves in the corona.

Before the postulated mechanism of ion cyclotron resonance is explained, we must ex-

plore Alfvén waves, how they are generated and how they can be understood to interact with coronal plasma.

2.2.1 Alfvén Waves

By linearising the continuity equation, momentum equation and Faraday's Law from Maxwell's equations, one can include a small perturbation in the plasma. Compressible (driven by a pressure gradient) and non-compressible (driven by magnetic tension) wave propagation both result. With the assumption we are dealing with a plane wave propagating in the x direction, oscillations will take the form of $e^{ikx}e^{-i\omega t} = e^{i(kx-\omega t)}$, where $k = 2\pi/\lambda$ and $\omega = 2\pi f$. Two independent solutions are possible from the roots of the dispersion relation. These roots provide expressions for the phase velocity for MHD waves in a "cold", or low-β plasma ($v_A \gg v_S$)

$$\left(\frac{\omega}{k}\right)^2 = v_A^2 \cos^2\theta \tag{2.2}$$

and

$$\left(\frac{\omega}{k}\right)^2 = v_A^2 \tag{2.3}$$

Eq. 2.2 is known as the *shear Alfvén wave* and Eq. 2.3 is known as a *compressional Alfvén wave*. The shear Alfvén wave does not change the plasma density as the fluid is set in motion in the direction perpendicular to **B** and k plane. The compressional Alfvén wave changes the fluid density by setting the plasma in motion within the **B**-k plane (gas pressure and magnetic pressure fluctuations are also in phase signifying this mode is also a *fast mode wave*).

The group velocity ($\mathbf{v_g}$) of these waves provide a physical meaning as to the propagation

of energy. By simply looking at the vectors in the direction of $\hat{\mathbf{k}}$ and $\hat{\mathbf{B}}$ the direction of propagation becomes obvious. For the shear wave, $\mathbf{v_g} = v_\mathrm{A}\hat{\mathbf{B}}$ and for the compressional (fast) wave $\mathbf{v_g} = v_\mathrm{A}\hat{\mathbf{k}}$. This means, in the case of the shear wave, that energy (and information) is strictly guided by the background magnetic field (even when θ directs the phase fronts in an arbitrary direction). The compressional wave is able to propagate in all directions without any such restriction.

High-β ("warm") plasmas have their associated wave modes too, but will not be detailed here as magnetic pressure dominates in the corona and this thesis only assumes low-β plasma. More specifically, the parallel propagating Alfvén wave is used in the model outlined in this study as Alfvén waves have very useful qualities when trying to explain the mechanism that may be heating coronal loops and the extended corona. One such property focuses on the interaction between high frequency Alfvén waves and ions (or protons). This mechanism is known as *ion cyclotron resonance*.

2.2.2 Ion Cyclotron Resonance

The resonant condition between the wave and plasma species is

$$\omega\left(k_{\|}\right) - k_{\|}v_{\|} = \pm\Omega_s \tag{2.4}$$

The ± sign in Eq. 2.4 refers to the polarity of the wave, '–' for right-hand (whistler mode) waves and '+' for left-hand waves. ω is the wave frequency, $k_{\|}$ the wave number (parallel to B_0), $v_{\|}$ is the wave velocity and Ω_s is the plasma species gyrofrequency.

Resonance between Alfvén wave and particle can only be achieved if the wave (*a*) has a frequency (ω) matching that of the gyrating particle (Ω) and (*b*) a polarisation matching that of the direction of particle gyration. Figure 2.1 demonstrates that, as the Alfvén

wave propagates, its electric field (**E**, perpendicular to **B**) traces a spiral path. As one would expect, if a charged particle is injected into an electric field, depending on the sign of its charge, it will be accelerated. If resonance is achieved (fulfilling both of the conditions (*a*) and (*b*) mentioned above), one can expect the gyrating particle to experience an increase in its Larmor radius. This interaction may lead to significant acceleration and therefore heating.

Ion cyclotron resonance is the suspected mechanism driving the temperature anisotropy as observed in the solar wind. By measuring the ratio of the coronal plasma's parallel and perpendicular (to the magnetic field) temperatures ($T_\perp/T_\parallel$), an anisotropy may result. If $T_\perp/T_\parallel > 1$ it is evident that the plasma ions are being accelerated perpendicular to the magnetic field signifying passage of resonant waves (as the electric field of the propagating wave precesses around the magnetic flux perpendicular to the direction of propagation, Fig. 2.1). Interestingly, in the extended solar wind, Li *et al.* (1999) suggest that modelled ion cyclotron resonance may be responsible for observations that show $T_{p\perp} \gg T_{p\parallel}$ in the inner corona and $T_{p\perp} < T_{p\parallel}$ at 1AU. Li *et al.* assume low-frequency Alfvén waves carry most of the energy to heat the fast solar wind and must undergo a non-linear cascade process so energy can be transported to the high frequency resonant waves.

Ion cyclotron resonance has been extensively studied in the solar wind (Tu & Marsch, 1995, Allen *et al.*, 2000, Liewer *et al.*, 2001, Li, 2002) and is very successful in accounting for observed characteristics of protons and heavier ions. However, as discussed by Habbal & Woo (2004), the heating of electrons remains problematic as modelled electron temperatures are lower than observation.

The velocity and magnetic fluctuations in the solar wind are correlated and the non-compressive nature of the fluctuations uncover Alfvénic interactions (Belcher, 1971, Belcher & Davis, 1971). This phenomenon is not restricted to the open flux of the solar

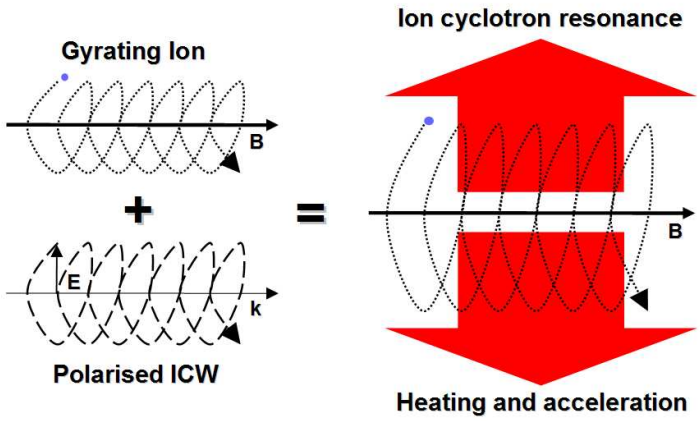

Figure 2.1: The principal of ion cyclotron resonance.

wind however. The highly magnetised and conductive environment of closed magnetic structures readily exhibit Alfvén wave propagation. As stated by Hollweg (1986), waves will propagate symmetrically around coronal loops promoting the development of turbulence and non-linear heating mechanisms (Section 2.3).

2.2.3 Mode Coupling, Phase Mixing and Resonant Absorption

The idea that Alfvén waves heat the corona is not only restricted to ion cyclotron resonance, there must be an awareness that coronal heating may be attributed to more than one wave heating process.

It is well known that magnetic flux footpoints undergo an intense expansion in cross section from photosphere to corona. Bray *et al.* (1991) states that as the density sharply decreases, the magnetic flux flares out causing a change in waves propagating along the flux. The original wave mode may split into a mixture of modes in response to the change in local conditions. This is known as *mode coupling*. It is understood that Alfvén waves become partially longitudinal as they encounter field curvature. This longitudinal component will act locally as a highly dispersive fast mode wave, thus amplifying the

heating effect on coronal plasma.

Phase mixing and *resonant absorption* are two other possible mechanisms transferring wave energy to plasma (Ionson, 1978, Heyvaerts & Priest, 1983, Erdélyi, 2005). As one would expect, the magnetic flux is likely to be highly structured across the solar surface, varying the magnetic field from point to point. Heyvaerts & Priest (1983) describe the theorised mechanism of phase mixing that can arise from structuring of magnetic flux. One field line may be situated next to another field line of differing strength. As Alfvén waves propagate along the flux, different frequencies will exist and move out of phase with one another. A gradient of Alfvén velocity will appear across the fieldlines, high v_A in regions of strong magnetic flux, low v_A in regions of weak magnetic flux (Fig. 2.2a). This gradient may cause phase mixing of wave fronts, dissipation and therefore heating. As the magnetic flux expands exponentially into the corona, this effect is amplified by the exponentially increasing k of the propagating waves. Phase mixing appears to be an excellent mechanism for the dissipation of MHD wave energy in open flux regions such as the solar wind (Erdélyi, 2005).

Resonant absorption may also contribute to the coronal heating phenomenon (Ionson, 1978, Walsh & Ireland, 2003). In this case, MHD waves propagate along the surface of bundled magnetic flux (in a coronal loop or open flux tube for example). Energy from the surface MHD waves pass perpendicular to direction of propagation, exciting natural modes of oscillation in neighbouring fieldlines of different B_0 and v_A (Fig. 2.2b). This will have a damping effect on the propagation of the surface MHD wave as its energy is transmitted through the resonant layers. Heating will result. Resonant absorption may also lead to phase mixing as a gradient will be set up though the layers of bundled flux, enhancing the heating process.

For the above two energy dissipation mechanisms, there must be a process that decreases the length scales so energy can be transferred from wave to plasma. For heating

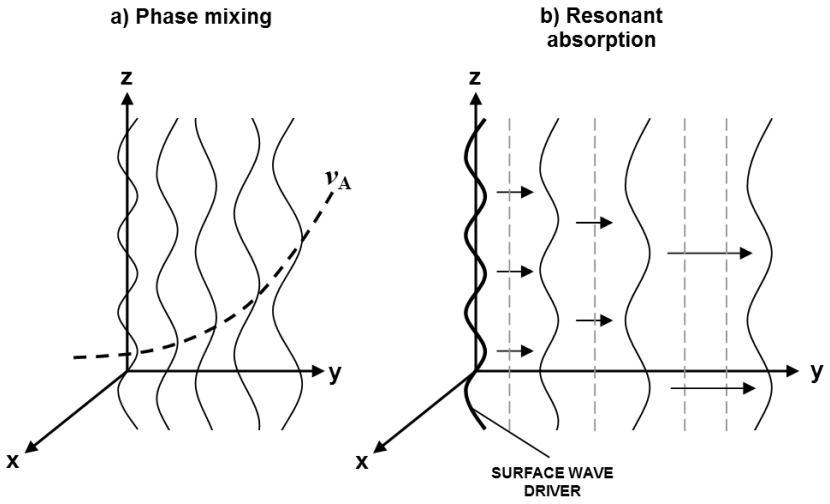

Figure 2.2: *a) Phase mixing.* Magnetic field lines of different strengths exhibiting a gradient in v_A. In this figure, B_0 increases in strength from left to right. *b) Resonant absorption.* A surface Alfvén wave transmits energy perpendicular to the direction of propagation (horizontal arrows), exciting the neighbouring flux's natural modes of oscillation, absorbing wave energy. Vertical dashed lines represent non-resonant flux.

to occur, from both phase mixing and resonant absorption, length scales in order of kilometers must be attained to make dissipation possible (Abdelatif, 1987).

2.2.4 Alfvén Wave Generation

The discovery that Alfvén waves do indeed propagate in the extended corona led to the discussion as to where these waves originate and how they are generated. The waves in this study are assumed to originate from a photospheric loop footpoint. It is widely believed that MHD waves exist in the chromosphere and transition region due to the signature of non-thermal velocities measured by instruments such as SUMER (see Section 2.4), leading to the thought that MHD wave generation may begin near the surface of the Sun. Ionson (1978) theorises oscillations generated in the chromosphere, with a required velocity of 6kms^{-1}, will propagate MHD waves into the corona of sufficient energy to explain the observed heating (through resonant absorption). Ulrich (1996) postulates that footpoint oscillations may cause the propagation of Alfvén waves high into

the corona. Observations by Muller *et al.* (1994) imply the corona may be heated very efficiently by turbulent granular motions generating MHD waves in the photosphere. By observing the motions of network bright points and assuming they are associated with magnetic flux, Muller *et al.* gain results suggesting the photospheric magnetic flux has turbulent motion with velocities up to 3kms^{-1}. Known as *footpoint shuffling* (Parker, 1987), magnetic flux motions may be associated with the footpoints of coronal loops, generating MHD waves at photospheric altitudes.

Alternative views on Alfvén wave generation include the possibility of *velocity shear* on current sheets near the surface of the Sun, generating inward and outward propagating waves (Belcher & Davis, 1971). Matthaeus & Goldstein (1983) suggest the existence of a 'minority species' mechanism producing outward propagating waves. The theorised mechanism of Alfvén wave generation is out of the scope of this work however and is worthy of more detailed study. The fact remains that Alfvén waves are generated near the solar surface and evidence of this can be attributed to the non-thermal motions measured by modern observatories.

2.3 Non-Linear Turbulent Cascade

Turbulence is common in nature and the solar environment is an excellent laboratory to study turbulent flow. Plasma in the solar wind undergoes turbulence on all scales, energy from plasma waves cascade, dispersing the energy and heating the corona through a dissipation process such as ion cyclotron resonance. Turbulent systems organise themselves in similar patterns of eddies, vorticies and flows no matter what scale (spatial and temporal) they are viewed at. This *self-similar* behaviour is characteristic of a chaotic system; unpredictable analytically but exhibiting a pattern nonetheless. Turbulent systems are also very sensitive to initial conditions. No turbulent flow can be the same,

they develop non-linearly. If a data set is acquired of magnetic fluctuations in the solar wind for the period of a year, say, and compared with a data set over the course of a day or even an hour (assuming the instrument observing is sensitive enough), there will be very little difference in the patterns displayed. The magnetic variations are self-similar regardless of scale. This is some indication of the turbulent processes at work in the solar wind. This behaviour is also thought to exist in coronal loops (although *in-situ* measurements to verify this are not possible).

From *in-situ* observations of the solar wind, turbulence can be detected when analysing the measured spectra of magnetic fluctuations. Figure 2.3 demonstrates the increase in wave number (k) when assuming the energy spectrum is from Alfvén waves interacting non-linearly. Figure 2.3 is a generalisation of results gained from the *Helios 1* (Tu & Marsch, 1995) mission where magnetic fluctuations were measured. Beginning in the "energy containing" range, the waves are mainly non-interacting Alfvénic and freely propagating in the solar wind. As k increases, interactions between outward propagating and inward propagating waves become possible, promoting the formation of turbulence, cascading wave energy to higher frequency waves. This is known as the "inertial range" (Matthaeus & Goldstein, 1982, Hollweg, 1986). As k increases, energy is lost from the dissipating waves as momentum is transferred from the wave to the plasma. As wave frequency approaches the gyrofrequency of the plasma, resonance occurs (through a process such as cyclotron resonance), heating and accelerating the plasma (Section 2.2). This is known as the "dissipation range". Wave energy is lost very quickly during resonance, so wave flux must be high and the turbulent cascade must be extensive.

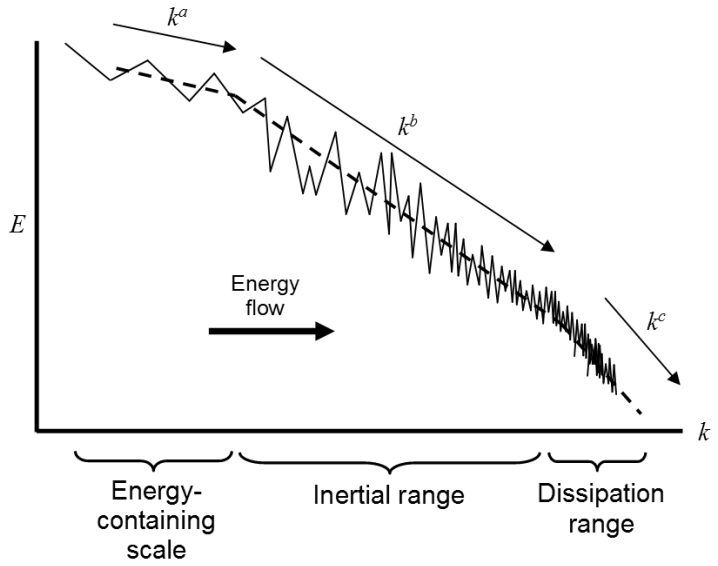

Figure 2.3: Summary plot of data collected by a range of observations, namely the study by Tu & Marsch (1995) where data from the *Helios 1* mission is evaluated. The k^b slope represents the inertial range where energy is cascaded to higher wavenumbers. The dissipation range is represented by a steeper k^c slope where ion cyclotron resonance dissipates wave energy into the plasma.

2.3.1 Kolmogorov vs. Kraichnan

By analysing the slope of the inertial range of a magnetic spectrum, a measure of the length scales of turbulence and the speed of energy cascade within a medium can be arrived at. The inertial range is not influenced by external input or output. This means that the turbulence creating a given spectra is supported solely by internal nonlinear dynamics, not by external turbulence driving the system or some dissipation mechanism releasing energy. The inertial range supports its own non-linear cascade.

It is generally agreed that there are 3 regimes of turbulence at work in the corona (see Chae *et al.* 1998 for discussion), each depending on the dominance of plasma velocity or dominance of the magnetic field and each demonstrating a different inertial range slope. The two regimes of most relevance are *selective decay* (Gómez & Ferro Fontán, 1988) and *dynamic alignment* (Heyvaerts & Priest, 1992). The *Navier-Stokes* regime (where kinetic energy dominates) will not be discussed as we are dealing with

a magnetic corona. Direct measurements of turbulence in the solar wind have been taken, but no direct measurements of turbulence are available in the corona or transition region. It is still not known which regime dominates, so many turbulence simulations model both Kolmogorov and Kraichnan turbulence scales (Chae *et al.*, 1998, Li *et al.*, 1999).

In the case of selective decay, magnetic energy dominates, in the case of dynamic alignment, there is an equipartition between magnetic and kinetic energies. A generally agreed characteristic of a non-linear cascade (in the selective decay regime) is that the slope of the inertial-range will tend to $k^{-5/3}$ and is known as the Kolmogorov cascade rate (Kolmogorov, 1941). The $k^{-5/3}$ decay of turbulence energy is typical of a hydrodynamic system. However when considering *magneto*hydrodynamic systems, although similar arguments and assumptions can be made from the Kolmogorov regime, Kraichnan (1965) finds as the sub-inertial wavenumbers exceed the total energy in the inertial range, the slope tends to a $k^{-3/2}$ rule. This occurs in the dynamic alignment regime and is known as the Kraichnan cascade rate.

The energy spectrum in any nonlinear system can be described as

$$k^a_{\text{containing}} < k^b_{\text{inertial}} < k^c_{\text{dissipation}} \tag{2.5}$$

where k represents the 3 sections of the energy spectrum in Fig. 2.3. The values of a, b and c get progressively greater, indicating progressively steeper slopes as we move to higher wavenumbers in the spectrum. It can be expected that $b = -5/3$ for the Kolmogorov regime and $b = -3/2$ for the Kraichnan regime. How these cascade rates are arrived at requires an understanding of how the microscopic interactions between turbulent "eddies" pass energy to higher wave numbers. In the case of dynamic alignment, Elsässer variables are used to explain these interactions due to the Alfvénic nature of

the eddies.

2.3.2 Elsässer Variables

Alfvén waves cannot undergo a non-linear turbulent cascade by themselves, there must be some interaction between counter propagating waves. As we are dealing with MHD turbulence theory in an incompressible plasma, the most important wave mode is the Alfvén mode. The basic perturbed plasma equations must therefore be scaled into *Alfvén units*.

If wave propagation is purely Alfvénic, Eq. 2.1 becomes $\delta v = \pm \delta B/\sqrt{4\pi\rho}$, where δv and δB are fluctuations in the velocity and magnetic field respectively. This does not promote the development of a non-linear cascade as it represents the propagation of a wave in one direction. Non-linear interactions are only possible if there is an interaction between inward and outward propagating waves, breaking the relationship, $\delta v \neq \pm \delta B/\sqrt{4\pi\rho}$.

Elsässer (1950) derived the *Elsässer variables* to explain the nature of inward and outward propagating Alfvén wave contributions to a turbulent cascade of energy. For a full review of Elsässer variables refer to Bruno & Carbone (2005). In brief, the Elsässer variables ($z^{\pm}$) are defined as

$$\mathbf{z}^{\pm} = \mathbf{v} \pm \frac{\mathbf{b}}{\sqrt{4\pi\rho}} \tag{2.6}$$

where **v** is the proton velocity and **b** is the magnetic field in an inertial reference frame. The ± sign in front of **b** is decided by the wave direction, counter-intuitively *minus* ($-\mathbf{k} \cdot \mathbf{B_0}$) for *outward* propagating waves and *plus* ($+\mathbf{k} \cdot \mathbf{B_0}$) for *inward* propagating waves. However, this is confusing and the magnetic field vector, $\mathbf{B_0}$, is rotated 180^{o}

when directed away from the Sun. Therefore a wave with a '–' sign will always be an inward propagating wave and a wave with a '+' sign will be outwardly propagating regardless of the direction of the magnetic field vector.

A complete description of the interacting waves can be arrived at when **b** is normalised by $\sqrt{4\pi\rho}$ (**b** will be measured in Alfvén units). Equation 2.6 will become $\mathbf{z}^{\pm} = \mathbf{v} \pm \mathbf{b}$. The velocity field will be $\mathbf{v} = (\mathbf{z}^{+} + \mathbf{z}^{-})/2$ and magnetic field will be $\mathbf{b} = (\mathbf{z}^{+} - \mathbf{z}^{-})/2$. The MHD equations must also be normalised with respect to the Alfvén time (τ_{A}), so the parameters (length, time, magnetic field and pressure) are treated as

$$\frac{s}{L} \rightarrow s, \quad \frac{t}{\tau_{\mathrm{A}}} \rightarrow t, \quad \frac{b}{B_0} \rightarrow b, \quad \frac{p}{(\rho_0 v_{\mathrm{A}}^2)} \rightarrow p \tag{2.7}$$

From this, the second order moments such as kinetic energy, magnetic energy, z^{+} or z^{-} energies and the normalised MHD equations can be derived.

If we assume that the dynamics of the turbulent cascade is due to the non-linear interaction and scattering of Alfvén waves, the system will relax into an aligned state (Dobrowolny *et al.*, 1980, Biskamp, 2003). The z^{+} and z^{-} components will only interact non-linearly with one another (there are no self-interactions). Only Alfvén waves propagating in opposite directions will interact, but *how* is the energy cascaded to smaller scales, decaying the turbulence formed by these interacting waves?

Two timescales are at work when considering the cascade of energy, the Alfvén time ($\tau_{\mathrm{A}} = l/v_{\mathrm{A}}$) and the time it takes for a wave packet (δz^{+}, also known as an 'eddy') of scale l to distort an equal but opposite eddy (δz^{-}). The time period of this interaction will be $\tau_l^{\pm} = l/\delta z_l^{\mp}$. Generally, $\tau_{\mathrm{A}} \ll \tau_l^{\pm}$, where τ_{A} indicates the time for opposite propagating waves to interact fully. There will be a small change in amplitude of $\Delta\delta z_l$ after each consecutive collision, therefore

$$\frac{\Delta\delta z_l^{\pm}}{\delta z_l^{\pm}} = \frac{\tau_{\rm A}}{\tau_l^{\pm}} \ll 1 \tag{2.8}$$

To produce a relative (and significant) change in amplitude of the order of unity, $N \approx (\delta z_l/\Delta\delta z_l)^2$ elementary interactions are needed. From this, the energy-transfer time ($T_l^{\pm}$) can be arrived at

$$T_l^{\pm} \sim N\tau_{\rm A} \sim (\tau_l^{\pm})^2/\tau_{\rm A} \tag{2.9}$$

In brief, energy is cascaded by interacting eddies causing a change in amplitude of each daughter eddy, thus passing energy down the cascade to higher k.

A significant conclusion is made from this analysis, if $\delta z_l^+ > \delta z_l^-$ (i.e. more outward than inward propagating waves), δz_l^- is depleted more rapidly, leading to a dominance of the δz_l^+ spectrum. This will continue till the cascade is exhausted into an outward propagating Alfvén state.

Voyager 1 and 2 collected magnetometer data as they travelled from 1 to 11AU (Roberts *et al.*, 1987). By measuring the energy spectrum of solar wind magnetic field, the cross-helicity and total energy of magnetic fluctuations could be calculated (from the Elsässer variables). The cross-helicity and total energy is given by $H_c = \langle\delta\mathbf{v}\cdot\delta\mathbf{b}\rangle/2$ and $E = \langle\delta\mathbf{v}^2 + \delta\mathbf{b}^2\rangle/2$ respectively. By simply taking a ratio of the cross helicity and total energy, the *normalised cross-helicity* ($\sigma_c = 2H_c/E$) can be calculated. This is a useful tool to analyse the Alfvénicity of the fluctuations in the solar wind. If $|\sigma_c| \approx 1$, the fluctuations are Alfvénic in nature.

A key result to arise from Roberts *et al.* (1987) is that 10-15% of the data accumulated suggests perfect-aligned Alfvén waves. 85-90% of the data shows inward and outward propagating Alfvén waves and a mix of other modes. There is however a dominance

of outward propagating waves in the inner heliosphere. There is a far higher percentage of mixed inward and outward propagating waves than pure non-interacting waves suggesting a turbulent energy cascade may be dominant in the solar wind.

We now know the energy may be cascaded by means of small scale wave packet interactions and these small scale interactions vastly effect the turbulent spectra of the magnetic field. As we are dealing with stationary turbulence, any rapid change in energy input (in the energy containing region of the spectrum) will cause a near-instantaneous change in the inertial range. Therefore, where ε is the energy transfer rate, $\varepsilon_{\text{containing}} = \varepsilon_{\text{inertial}} = \varepsilon_{\text{dissipation}}$ (corresponding to Eq. 2.5), energy transfer is conserved within the stationary system.

2.3.3 Turbulent Heating Rates

In a hydrodynamic turbulent system, Kolmogorov (1941) describes general turbulent spectra where the cause of the turbulence is not important, it is a general interpretation of fluid turbulence. In this case, assuming the energy transfer is local and discrete, the inertial range can be divided into small scale lengths, l_n (where $l_0 > l_1 ... > l_{N-1} > l_N$). The relationship between l_n and k_n will be $l_n = k_n^{-1}$. As already stated, energy is passed via distortions of interacting eddies, so energy will be passed between neighbouring scales (i.e. l_n and l_{n+1}). The time for the interaction to occur can be approximated by $\tau_n \sim l_n/\delta v_n$, where δv_n is called the distortion time. Knowing the energy flux is constant across the inertial range, by rearranging the relationship $E_n/\tau_n \sim \delta v_n^3/l_n \sim \varepsilon$, a scaling relation becomes apparent

$$\delta v_n \sim \varepsilon^{1/3} l_n^{1/3} \quad - \textit{The Kolmogorov scaling relation} \tag{2.10}$$

To arrive at an energy spectrum for this regime (E_k), the eddy energy is integrated via a

Fourier transform ($E_n = \int_{k_n}^{k_{n+1}} E_k dk$) which leads to

$$E_k \sim \varepsilon^{2/3} k^{-5/3} \tag{2.11}$$

Kraichnan (1965) modifies this idea by specifically assuming the turbulence is caused by interacting Alfvén waves. The small scale fluctuations are strongly effected by the macro-scale magnetic field feeding through the system, thus small scale fluctuations in magnetic field behave Alfvénically. This is where Elsässer variables are called into use (Section 2.3.2). Similar assumptions are made in the Kolmogorov regime, but Kraichnan specifically develops this idea for an MHD system. δv is replaced with the wave packet equivalent δz and the energy transfer time (τ_l) is longer and changed to T_l. Therefore, using the relation described in Eq. 2.9 ($T_l \sim (\tau_l)^2/\tau_\mathrm{A}$) and rearranging $E_l/\tau_l \sim \delta z_l^4 \tau_\mathrm{A}/l^2 \sim \varepsilon$, another scaling relation becomes apparent

$$\delta z_l \sim (\varepsilon v_\mathrm{A})^{1/4} l^{1/4} \quad - \textit{The Kraichnan scaling relation} \tag{2.12}$$

which leads to the spectrum (following from Eq. 2.11)

$$E_k \sim (\varepsilon v_\mathrm{A})^{1/2} k^{-3/2} \tag{2.13}$$

Initially introduced for the extended solar wind, a non-linear heating mechanism was required to explain observed solar wind velocity and density at a distance of 0.1AU (Hollweg, 1986, Hollweg & Johnson, 1988). The heating rate (Q) required to heat the solar wind plasma is assumed to be turbulent in nature leading to the assumption that the turbulence is generated by interacting Alfvén waves (now in both Kolmogorov and Kraichnan regimes). It is worth noting the *energy injection rate* in the inertial range (ε in Eq. 2.11) has the units of 'energy injection rate per unit mass' (erg cm^{-3} s^{-1}) which is iden-

tical to the 'heating rate per unit mass'. As detailed by Chae *et al.* (1998) and Gómez & Ferro Fontán (1988), the spectrum in Eq. 2.11 is integrated over the inertial range so the heating rate for a selective decay regime can be found (Eq. 2.14)

$$Q = \Gamma \frac{\rho \langle \delta \mathbf{v}^2 \rangle^{3/2}}{L_{\mathrm{corr}}} \tag{2.14}$$

where $\langle \delta \mathbf{v}^2 \rangle$ is the variance in the velocity field of a propagating Alfvén wave, Γ is a dimensionless factor of the order of unity and L_{corr} can be related to the magnetic structures in the photosphere. It is assumed by Hollweg (1986) that L_{corr} is the mean distance between photospheric flux tubes. The proposed wave generation via flux tube footpoint shuffling will therefore create waves of these scales.

Now, substituting $\langle \delta \mathbf{v} \rangle$ with ξ

$$Q = \Gamma \frac{\rho \xi^3}{L_{\mathrm{corr}}} = \frac{\rho \xi^3}{l_{\mathrm{drive}}} \tag{2.15}$$

where $l_{\mathrm{drive}} = \Gamma / L_{\mathrm{corr}}$ is the *driving scale* of the dissipating waves (Li & Habbal, 2003). Γ is assumed to be absorbed into L_{corr}, therefore creating l_{drive} and is assumed to be of the dimensions approximating photospheric granulation cells.

The dynamic alignment regime can be treated in the same manner. Integrating the spectrum (Eq. 2.13), the Kraichnan cascade rate can be derived (Heyvaerts & Priest, 1992, Chae *et al.*, 1998, Biskamp, 2003)

$$Q = \Gamma \frac{\rho \langle \delta \mathbf{v}^2 \rangle^2}{v_{\mathrm{A}} L_{\mathrm{corr}}} \quad \rightarrow \quad \frac{\rho \xi^4}{v_{\mathrm{A}} l_{\mathrm{drive}}} \tag{2.16}$$

Note, the Kraichnan cascade rate will cascade energy on a different scale to the Kolmogorov cascade rate. v_{A} is very large in the lower corona and the influence of this

parameter will vastly affect the value of the driving scale (l_{drive}). A quick deduction will conclude that the driving scales associated with the Kraichnan regime will be two orders of magnitude lower than the driving scales associated with the Kolmogorov regime for the Kraichnan regime to have any heating effect. In general, it is expected that the Kolmogorov cascade rate operates over scales from hundreds to thousands of kilometres. The Kraichnan cascade rate operates over tens of kilometres. As discussed by Chae *et al.* (1998), the determined value of Kolmogorov scales is approximately 1200km, well within observational capabilities of instrumentation. This scale also relates to photospheric granulation distancing (as proposed by Hollweg 1986 and assumed by Li & Habbal 2003), therefore linking the region of wave excitation with a physical (and measurable) feature on the solar surface. Kraichnan scales are below observational resolutions so can only be guessed at. This is not to say waves excited in the Kraichnan regime do not exist (the Kraichnan cascade rate is used to great effect by Chae *et al.* 2002). It is however hard to propose a mechanism for wave production at these scales if there is little observational evidence to support theory.

2.4 Spectroscopic Non-Thermal Velocities

This work is based on the assumption that non-thermal motions in the chromosphere and transition region are due to the interactions of Alfvénic turbulence with plasma. Non-thermal motions are evident from analysis of broad, Doppler-shifted spectral lines. Once thermal motions are accounted for, an excess of broadening remains. *Non-thermal* broadening of spectral lines are attributed to wave activity within the chromosphere and transition region. These wave driven motions have an associated velocity and can be linked with Alfvén wave propagation.

The Alfvén wave amplitude, ξ, given in Eq. 2.15, can be directly taken from the non-

thermal velocity observations described by Chae *et al.* (1998), Chae *et al.* (2000) and Chae *et al.* (2002) (and references therein). Although these motions are not thermal in origin, they are a function of chromospheric temperature where the Alfvén waves propagate through. As demonstrated in Fig. 2.4, between the temperature range of 10^4-10^6K, ξ has a range of 0-30kms^{-1}. As outlined in Section 3.2.1, the parameter ξ is derived from Chae *et al.* (1998) for the desired loop footpoint temperature.

Non-thermal velocities are observed in the solar chromosphere by a variety of instruments. Spectrometers on board early spacecraft such as the *Skylark* missions (Boland *et al.*, 1975), the *Spacelab-2* Shuttle mission (the NRL High Resolution Telescope and Spectrograph; Dere *et al.* 1987), the *Solar Maximum Mission* (the Ultraviolet Spectrometer and Polarimeter; Doyle *et al.* 1997) to more recently *SOHO* (the SUMER instrument; Section 1.5; Chae *et al.* 1998) have shown non-thermal broadening of spectral lines to be commonplace.

Extreme non-thermal velocities have been measured by a number of authors. Off-limb UV measurements by Kjeldseth Moe & Nicolas (1977) using *Skylab* data find non-thermal velocities of 23-75kms^{-1} and Acton *et al.* (1981) find X-ray non-thermal velocities of approximately 50kms^{-1} when analysing *Solar Maximum Mission* data. For the time being, the non-thermal velocities as measured by Chae *et al.* (1998) are the most applicable signatures of MHD waves, but there must be an awareness of high-ξ values.

Under the assumption that non-thermal motions have a Gaussian distribution, the *most probable non-thermal velocity* (Mariska, 1992, Erdélyi *et al.*, 1998) can simply be added to the observed Doppler width given by

$$\Delta\lambda_{\mathrm{D}} = \frac{\lambda_0}{c}\left(\frac{2kT}{M} + \xi^2\right)^{1/2} \tag{2.17}$$

Put simply, the non-thermal velocity may be described as a root-mean-square velocity,

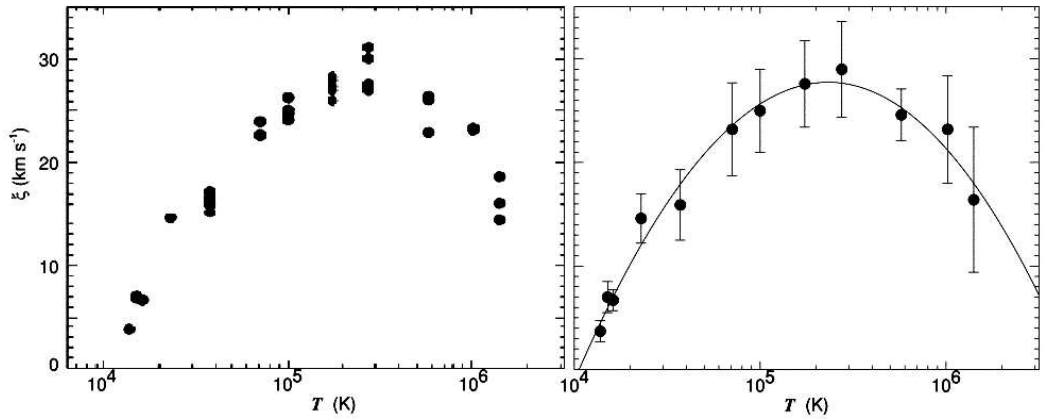

Figure 2.4: The ξ (non-thermal velocities) vs. temperature curve adapted from Chae *et al.* (1998) (original data; *left panel*) and Chae *et al.* (2002) (plot used to read off ξ/T values in this thesis; *right panel*)

$v_{rms} = (3/2)^{1/2}\xi$. Other authors such as Boland *et al.* (1975), Doschek *et al.* (1976), Mariska *et al.* (1978) and Cheng *et al.* (1979) have measured a similar relationship between chromospheric temperature and ξ as indicated by Chae *et al.* (1998) and Chae *et al.* (2002) (Fig. 2.4). The non-thermal velocity can also be described as the *velocity variance associated with the wave field* ($\langle \delta \mathbf{v}^2 \rangle$, Eq. 2.14) or the *Alfvén wave amplitude* (ξ in Eq. 2.15).

Non-thermal broadening of spectral lines is not necessarily isotropic (i.e. the broadening observed at the solar disk may not be the same when measured at the limb). Erdélyi *et al.* (1998) find a general broadening of line widths from disk centre to solar limb when using data from SUMER and attribute the broadening to Alfvén wave propagation. This contradicts earlier work by authors such as Boland *et al.* (1975) where it is assumed wave heating is the cause of non-thermal broadening, but find it to be isotropic in nature. Doyle *et al.* (2000) supports the non-isotropic findings and indicates the broadening may not be uniform across all plasma ion lines. Doyle *et al.* find the CIV and HeI lines both exhibit disk-to-limb broadening, but the high temperature NeVIII line remains constant. However the variation is small and attributed to opacity effects in the solar atmosphere and conclude mass motions in the chromosphere and

transition region may indeed be isotropic. There may also be a height dependence on line broadening. Work by Harrison *et al.* (2002) support Alfvén wave dissipation theory by analysing spectroscopic data at increasing altitudes from the solar surface. It is found that non-thermal broadening (and therefore Alfvén wave amplitude) generally decreases with height. This suggests that if the non-thermal broadening is associated with MHD wave activity, the waves are dissipated in some way as they propagate in the corona (although this effect is disputed by Wilhelm *et al.* 2004, 2005).

Although the measurement and interpretation of non-thermal velocities may be open to debate, non-thermal observations in the chromosphere and transition region remain a very useful tool when trying to understand proposed MHD wave activity in solar plasmas. Now the theorised source of MHD waves and the mechanism of a non-linear turbulent cascade has been explored, it seems prudent to research present coronal loop models to focus on how they might be improved by applying a method as described in this thesis.

2.5 Coronal Loops Heated by Turbulence

Steady chromospheric and coronal heating models can be separated into 2 groups. The first group encompass hydrodynamic heating mechanisms. This group deals with shock dissipation of acoustic waves which propagate from the solar surface and heat the chromospheres of stars with weak or no magnetic field. As mentioned by Narain & Ulmschneider (1990, 1996), this may be the case for late-type slowly rotating stars, but is not thought to be a main contender in our magnetically dominated Sun. Acoustic shock heating will therefore be discounted. The second group encompass magnetic heating mechanisms. This group is further divided into *DC heating* (magnetic field dissipation) mechanisms and *AC heating* (MHD wave dissipation) mechanisms.

DC heating mechanisms rely on impulsive releases of energy where electric currents appear steady along the loop length. Energy is injected to cause an irreversible change in loop evolution. AC heating mechanisms rely on a continuous supply of energy propagating from the photosphere. In this case, electric currents are oscillating (due to the wave nature of the disturbance) and the timescales of the oscillations are lower than the time taken for an Alfvén wave to travel along the length of the loop.

DC heating of coronal loops assumes some form of potential energy release caused by the displacement of loop footpoints. Magnetic field lines become twisted, shifted, braided or forced together by photospheric convection currents, differential rotation or horizontal plasma flows. This build-up of potential energy may generate reconnection events (such as intermittent explosive events) due to magnetic instabilities. Aschwanden (2001) argues that although these may be important mechanisms, they produce uniform heating rates along the loop length, disputing the observed non-uniform heating function (Parker, 1988).

AC heating of coronal loops on the other hand provides a viable mechanism for describing the non-uniform and footpoint heating observations. The energy for AC mechanisms can be generated by photospheric motion and turbulence transmitting waves into the corona. The propagating waves are assumed to be the carrier of energy used to heat the coronal plasma. Alfvén waves are considered to be the best candidate as they do not suffer reflection off lower layers of the transition region (Aschwanden, 2001). Due to the steep gradient of temperature and density through the transition region, MHD waves would normally reflect off this boundary, severely hindering any energy propagation into the corona. This boundary resembles a wavelength-dependent reflection and transmission filter where certain Alfvén wave wavelengths can resonate in the leaky cavity of the coronal loop. This, and providing there is sufficient twist in the magnetic flux (Litwin & Rosner, 1998a,b), Alfvén waves are able inject large energy flux into the

corona due to high v_A in the region.

If footpoint motions are of a high enough frequency, the waves propagating through the coronal loop will be able to set up turbulence in the AC regime. Hollweg (1984) suggests turbulent heating by Alfvén waves and that 85% of the energy flux entering the loop will be dissipated in the loop. However it is found that the majority of the heating is not near the footpoints, but high in the loop, near the apex. This defies current observational and model evidence of EUV loops. Aschwanden *et al.* (2001) find the heating mechanism to be concentrated in the locality of the loop footpoint. The heating scale height operates in the lower 20% of the loop length ($s_H/L = 0.2 \pm 0.1$) suggesting a strong non-uniform heating rate. Other authors confirm this finding (Antiochos & Klimchuk, 1991, Neupert *et al.*, 1998, Lenz *et al.*, 1999, Aschwanden *et al.*, 2000a). Chapter 4 models coronal loops with a range of heating profiles and find that loops maintained by non-uniform (and focused footpoint) heating can approximate observed isothermal temperature profiles for a particular range of loops. It is difficult to balance the turbulent heating parameters (i.e. the driving scale length and Alfvén wave amplitude) to maintain the isothermal profile. Isothermal temperature is also highly dependent on loop length, a complication not currently observed (Section 5.3), although loop inclination (Reale 1999 and Section 5.4) may be a contrubuting factor.

To acquire an answer for the heating of coronal loops, the chromosphere, transition region and corona must all be incorporated in loop models (Aschwanden, 2001). There is a known chromospheric source of plasma feeding coronal loops, an observed non-uniform heating profile (often with strong footpoint heating) and a sudden temperature enhancement through the transition region. Also, if Alfvén waves are to be the prime candidate for coronal heating, some form of turbulence may be at work to cascade wave energy so it can be dissipated. As highlighted by Bray *et al.* (1991), most coronal loop models focus on energy being carried into coronal loops from outside the corona (i.e.

injected from the chromosphere), but some suggest coronal loop heating from turbulent generated waves formed well within the corona (van Tend, 1980). Li & Habbal (2003) approach this challenge by modelling a coronal loop where waves are generated outside of the corona, but then assume a non-linear process *within* the corona which cascades energy into resonant waves (Section 2.2.2). This model is unique in that it addresses the multicomponent structure of a coronal loop, incorporates gravitational stratification and is self-consistent.

Turbulent heating of coronal loops have been modelled before (Heyvaerts & Priest, 1992, Inverarity *et al.*, 1995, Inverarity & Priest, 1995, Dmitruk & Gómez, 1997, 1999). However, these loop models assume a homogeneous electron density and a homogeneous axial magnetic field, thus producing a uniform heating rate along the loop length.

Heyvaerts & Priest (1992), Inverarity *et al.* (1995) and Inverarity & Priest (1995) assume convective motions at the photosphere drag magnetic fieldlines. This motion may cause net storage of energy (to be released after a period of time) or instant wave propagation, via DC or AC heating mechanisms respectively. To balance the coronal loop in a quiescent state, a heating mechanism strong enough to counteract radiative and conductive losses is required. In this case, Inverarity *et al.* (1995) and Inverarity & Priest (1995) model Alfvén waves propagating back and forth along an arcade of coronal loops driven by rapid photospheric motions. As the waves propagate through the turbulent plasma, a cascade reduces the scale of waves till the plasma absorbs (or damps) the waves. Results from these studies suggest turbulence within coronal loops amplify Alfvén wave heating. Inverarity & Priest (1995) however encounter some difficulty in implementing Kraichnan cascade rates when considering large eddy scales.

Dmitruk & Gómez (1997) approach turbulent heating of coronal loops also by shuffling the loop footpoints. As the magnetic Reynolds number is assumed to be very large ($R_{\rm m} \approx 10^{10} - 10^{12}$), footpoint shuffling is found to promote strong turbulence within the

loop. After a period of time, the coronal loop reaches a "turbulent stationary regime". Within the modelled results, Dmitruk & Gómez find the turbulent nature of the loop promotes intermittent heating events (a.k.a. nanoflares) and have a turbulent spectrum approximating that of a Kolmogorov cascade ($k^{-3/2}$).

Flare, nanoflare and microflare heating is also commonly investigated as possible coronal heating mechanisms and are often attributed to turbulence and MHD wave activity (Moriyasu *et al.*, 2004, Reale *et al.*, 2005). With the advent of high resolution imaging by instruments on board missions such as *SOHO*, *TRACE* and *Yohkoh*, a plethora of transient, small scale heating events have been discovered. The three flare categories mentioned above are basically the same event but of different energy classes. Flares have an energy range of 10^{30} – 10^{33}erg and will typically reach temperatures between 8 – 40MK, microflares have energies in the range of 10^{27} – 10^{30}erg and reach temperatures between 2 – 8MK and nanoflares have energies in the range of 10^{24} – 10^{27}erg, reaching temperatures of 1 – 2MK (Parker, 1988, Aschwanden, 2004). Naturally each class will radiate at a particular frequency. Nanoflares radiate in the EUV wavelengths and can be detected by instruments such as *TRACE* (Parnell, 2002), microflares emit soft X-rays and can be detected by instruments such as SXT on *Yohkoh* and large flare events may be observed across a range of frequencies (Aschwanden, 2004). Parnell & Jupp (2000) suggest approximately 20% of the required coronal heating may come from nanoflares and microflares. Parnell & Jupp also state that many more subtle flare events may occur out of the scope of current instuments. Only flares of sufficient density and temperature can be observed through the observational bandpasses, there may be many more sub-resolution events heating the corona. These processes are all symptomatic of rapid magnetic reconnection and my produce secondary processes such as MHD wave activity, perhaps amplifying wave-wave interactions in the corona (such as the non-linear cascade as investigated in Section 2.3).

Reale *et al.* (2005) relates nanoflare activity along coronal loops with the dissipation of MHD turbulence. Again it is assumed photospheric footpoint motions promote MHD disturbances and non-linear interactions further along the loop structure. These turbulent motions cause reconnection events, creating nanoflares and heating along the $L = 30$Mm loop. Current research appears to be drifting in the direction of a strong relationship between nanoflare events and wave activity. MHD wave activity may cause non-linear effects, creating instabilities and triggering intermittent releases of energy. Nanoflare activity may cause MHD wave pulses, creating a source of inward and outward propagating Alfvén waves. This two-way relationship requires further study and a requirement should be set on modern simulations for the inclusion of the wave-nanoflare mechanism.

As Aschwanden (2001) and Li & Habbal (2003) agree, coronal loop models must be multi-component (including chromosphere and transition region) so the loop heating profile can be focused near the loop footpoint (in the case of overdense and isothermal EUV coronal loops) and they must be dynamic. There must be another process causing the observed densities and velocities as so far existing coronal loop models cannot explain loop dynamics. This thesis takes the view that the model described here implements all of the above factors but through self-consistent wave propagation, momentum deposition from wave to plasma occurs to further enhance coronal loop density.

2.6 Other Coronal Loop Models

The previous section focuses on turbulence as an ideal tool to model the heating of coronal loops. Beginning with the categorisation of AC and DC heating mechanisms, it becomes evident there may be an inter-relationship between the two families. One such example is the idea nanoflares (DC heating) may be the cause of, or be caused by, wave

propagation (AC heating). However, not all models neatly 'fit' into these categories, so a brief overview of other relevant coronal loop models will now be presented.

Chae *et al.* (2002) take a direct approach of modelling coronal loops by simply inferring the heating rates from observed turbulent MHD energy spectra for a given loop. They find strong footpoint heating maintains a dense and isothermal loop profile, generally agreeing with observations. An isobaric profile is assumed, this is not realistic as the gravitational stratification will cause pressure variation along the loop. Another limiting and very important factor is the non-inclusion of the chromosphere and transition region. Most models do not take the transition region into account, but if we consider the chromosphere as the reservoir of coronal loop plasma, this region must be taken seriously and modelled accordingly (Aschwanden, 2001).

Inferring the heating profile along coronal loops from observation or simply applying an *ad-hoc* heating function to match observations is not a recent idea however. The classical paper by Rosner *et al.* (1978) underpins modern simulations of the corona and makes an attempt at explaining early *Skylab* observations of basic loop structures emitting X-rays in the base of the corona. A quiescent, inhomogeneous solar corona is modelled, whereas before *Skylab* (Vaiana *et al.*, 1973) a homogeneous corona was assumed. The thermally insulated coronal loops observed are assumed to be in hydrostatic equilibrium with constant pressure. From observations, Rosner *et al.* are able to fit a variety of possible heating functions and arrive at the conclusion that the X-ray loops observed are maintained by uniform heating creating a temperature maximum at the loop apex. From this study two hydrostatic scaling relations could be constructed relating maximum temperature, pressure, loop length and heating rate (detailed in Chapter 4). Serio *et al.* (1981) advanced these scaling relations to allow for footpoint heating and pressure variation along the loop length. This modification to the hydrostatic model appeared to confirm observations until work by Porter & Klimchuk (1995) found dis-

crepancies when fitting with SXT (*Yohkoh*) loops.

Craig *et al.* (1978) model a simple quasi-static coronal loop with a constant cross section, similar to the model used by Rosner *et al.* (1978) and derive a contrasting scaling relation of loop length, density and temperature ($T^{9/4}/nL \approx constant$, when compared with $T/[nL]^{1/2} \approx constant$ from Rosner *et al.* 1978) and find results to be consistent with active region X-ray observations of the time. Hood & Priest (1979) build on the work by Rosner *et al.* (1978) also assuming quasi-static equilibrium and loops of constant pressure. Hood & Priest advance these ideas to include the effects of loop lengthening and twisting to find model calculations appear to produce loops with cool cores (i.e. a temperature reduction *inside* the loop). This leads to the reckoning that the cool plasma contained within the loop model would appear as active region filaments (or prominences) when surrounded by hot and highly radiating plasma.

These original coronal loop models set the scene for further investigation and led to the motivation to simulate dynamic loops as modern instrumentation improved observations (such as EIT on *SOHO* and SXT on *Yohkoh*). Naturally, numerous coronal loop models simulating plasma flow have been conceived in recent years. Orlando *et al.* (1995a) for example construct a model which simulates siphon flow around a simple semi-circular loop with constant cross-section. Siphon flows are driven by a pressure gradient between loop footpoints. This model simulates gravity, conduction and radiative losses in the hope of supporting new UV and X-ray observations and relating the results with classical scaling relations (Rosner *et al.*, 1978, Craig *et al.*, 1978, Serio *et al.*, 1981). Four classes of coronal loops are constructed: subsonic, critical, supersonic and unphysical. The subsonic solutions exhibit flow velocities below the local Mach number ($M = v/c_s < 1$), critical solutions are found where $M \approx 1$ (on the boundary between subsonic and supersonic flow), supersonic solutions are found where plasma flow exceeds M all round the loop and unphysical solutions result where the parame-

ters are not numerically sound. Orlando *et al.* (1995b) expands this study to work with shocked solutions (at the critical point, $M \approx 1$) where shock fronts form in regions of the loop where flow velocity exceeds the sound speed (refer to Chapter 5, Section 5.7, for shocked solutions arising from the study outlined in this thesis).

More advanced hydrodynamic models are constantly being developed. Patsourakos *et al.* (2004) for example model a loop of coronal length $L = 300$Mm (assuming a 60Mm chromospheric section for each footpoint, increasing the total length to 420Mm) with plasma flow in the hope to explain *TRACE* and EIT observations of EUV loops. As such loops are commonly found to have high densities, plasma flow driven by a highly assymetric heating rate is assumed. An *ad-hoc* heating rate is applied where there is concentrated footpoint heating and a degradation in heating along the loop length. Generally there appears to be an enhancement in loop density over static solutions, but a discrepancy remains. Patsourakos *et al.* concludes steady flow models cannot reproduce observed loop densities and indicate time-dependent, small scale releases of energy (i.e. nanoflares) may hold the key to observed plasma flow and EUV loop overdensity. Winebarger *et al.* (2002) approach a similar situation but with a shorter ($L = 150$Mm) loop. To maintain coronal loop flows of the order of observed quantities, an asymmetric heating function must be applied. This study find similar results as Patsourakos *et al.* (2004), but rather than indicating nanoflares may enhance loop densities, wave momentum deposition is indicated as a possible candidate.

This section has so far focused on loops heated by an assumed heating rate, whether it be uniform in the case of X-ray loop modelling (Rosner *et al.*, 1978) or non-uniform in the case of EUV loop modelling (Winebarger *et al.*, 2002, Patsourakos *et al.*, 2004) and results from these models have been highly successful in their aims. However, there must be an awareness of the physical effect a modelled mechanism will have on the heating rate. Priest *et al.* (2000) make an important statement:

> "*One of the paradigms about coronal heating has been the belief that the mean or summit temperature of a coronal loop is completely insensitive to the nature of the heating mechanisms... ...the temperature profile along a coronal loop is highly sensitive to the form of heating.*"

This means that for a given heating mechanism, the heating profile will be unique. In this case, Priest *et al.* use data from observations to deduce the heating profile along coronal loops and then attempt to link the profile with a mechanism that has the ability of producing such a profile. Other models take a likely heating mechanism candidate and model it *self-consistently*. For example, Ofman *et al.* (1998) carries out a self-consistent study of resonant absorption in coronal loop flux (Section 2.2.3) whilst including the effect of the chromosphere on the coronal loop. The chromosphere acts as a source and a sink of loop plasma ('chromospheric evaporation' and 'chromospheric condensation' respectively). The mechanism of resonant absorption characterises the plasma parameters. Ofman *et al.* find a single frequency of Alfvén wave to be insufficient for sustained resonance and heating in favour of a random (broadband) spectrum of Alfvén waves in order to maintain heating and loop density. In a different model, Bradshaw & Mason (2003) simulate the self-consistent modelling of 15 abundant coronal ion species cooling time-dependently and exhibiting significant non-equilibrium. The results from this lead to the conjecture that the reason why some models predict loop cooling in minutes (Warren *et al.*, 2002) whereas observations suggest hours (Lenz *et al.*, 1999) may be that contributions from non-equilibrium between plasma species have been overlooked.

These examples show self-consistent models to be more 'realistic' as the modelled heating mechanism characterises the plasma parameters and generate unique heating profiles. The model discussed in this thesis does not implement a heating profile, the waves propagating along the loop *create* the heating profile.

2.7 Discussion

It is evident that the solar corona is a complex system. Many theories exist for the heating mechanism of the coronal plasma and this chapter has mainly focused on wave heating, but has addressed the main candidates (including nanoflare heating). Many factors contribute to the eventual interaction between waves and particles. The first main obstacle is how the energy of non-interacting, low frequency (below the proton gyrofrequency) Alfvén waves can be dissipated. A non-linear turbulent cascade is a good candidate if counter-propagating Alfvén waves interact (Section 2.3). Through a non-linear cascade, energy can be transferred (cascaded) to high frequency waves allowing processes such as ion cyclotron resonance to occur, dissipating wave energy from the dispersionless to dispersive domain (Section 2.2.2).

Solar wind studies suggest a high degree of Alfvénic turbulence (Tu & Marsch, 1995). Although there is no *in-situ* observations of Alfvén wave interactions in the lower corona and coronal loops, it is assumed similar processes exist in this region. One such measurement of Alfvén wave activity in the lower corona, transition region and chromosphere are observations of non-thermal broadening of spectral lines (Section 2.4). If we attribute these observations to MHD wave activity, an origin of the wave energy necessary to heat the extended corona can be theorised. During propagation, if the waves undergo a non-linear process, the population of ion cyclotron waves can be maintained as a continuous heating mechanism.

It is important to be mindful that it is highly unlikely coronal loops are heated by a single wave heating process. It is more probable that this complex system supports a host of mechanisms all sharing a portion of the net heating effect. An interesting development in the search for the main heating mechanism is the inter-relationship between wave heating mechanisms. Perhaps wave interactions cause non-linear effects, destabilising

the magnetic flux, spurring reconnection and local explosive events such as nanoflares. This in turn may launch secondary waves that dissipate via another mechanism, amplifying the heating (Section 2.5).

Chapter 1 explored the energy transfer from the solar core to the corona and explained the baffling coronal heating phenomenon. This chapter has taken the standpoint of MHD wave heating via resonance with plasma particles (Alfvén waves as the main candidate) as the *only* heating mechanism capable of heating the solar atmosphere to millions of degrees. This is a very purest view, but Chapter 3 will expand these ideas into a functional coronal loop model in the aim of accounting for the observed heating. It is worth noting that this study is not discounting the contribution of other coronal heating mechanisms to the *total* heating, but it is hoped this work will explain the *main* mechanism is wave heating though a turbulent process.

Chapter 3

The Two-Fluid Numerical Method

3.1 Introduction

Modern numerical simulations of plasma interactions in the solar corona are a key element when understanding solar observations. As computational power increases, numerical methods of increasing complexity are at the disposal of a growing modelling community. The method used throughout this study is no exception. Originally used for solar wind acceleration models (Hu *et al.*, 1997), this one-dimensional full-implicit numerical method has been adapted for the coronal loop environment to great effect. The numerical method is constructed and compiled in the Fortran 77 (F77) programming language (using an Intel® Fortran Compiler for Linux installation[*]) and post-computation analysis (i.e. plotting and data manipulation) is carried out in IDL (Interactive Data Language[†] version 5.4 for Microsoft Windows). For the most part, computation and processing of the numerical method could be completed with a basic office PC (with a 1.24GHz AMD Athlon™ processor).

In the previous chapter, the theorised mechanisms at work in coronal loops are investigated. In this chapter, the physics of dynamic coronal loops will be reduced into

[*] http://www.intel.com/
[†] http://www.rsinc.com/

their constituent equations and modelled. Section 3.2 will detail the basic equations (continuity, momentum, energy), describe the numerical method used in this study and demonstrate how the "code" casts the parameters into a manageable structure. Section 3.3 outlines how outputted solutions from the model are arrived at and managed by applying an iterative approach. Section 3.4 gives a brief explanation into *Numerical Simulation Units* and how this unit system relates to conventional systems. Section 3.5 explains how the primary loop solution is arrived at and how it relates to two-fluid solar wind modelling. This brief overview leads on to how the loop could be lengthened and shortened (Section 3.6) and justifies the range of L selected for experimentation. In any coronal loop model it is essential that tests are carried out to verify simulation stability and accuracy. In this steady-state model energy conservation must be maintained along the whole loop length, Section 3.7 investigates this. Finally, Section 3.8 focuses on the greatest energy sink (radiation) and its implications for the model.

3.2 The Numerical Method

This full-implicit scheme for a one-dimensional two fluid conductive coronal loop is time dependent. This model is self consistent in that Alfvén waves travel along the coronal loops to set up a fully developed turbulent cascade and characterise the plasma parameters along the length of a thin coronal loop. This is the only mechanism heating the plasma. No *ad hoc* heating function is used to mimic a possible heating mechanism. This is useful to see if wave interactions in the corona may be contributing toward the coronal heating problem. The role waves play in the corona is not fully understood (Winebarger *et al.*, 2002), so the application of a method such as this seems prudent. Also, the two-fluid approach is justified as approximately 87% of positively charged particles populating the corona are ionized hydrogen (protons), contributing 77% of the total electron population (McWhirter *et al.*, 1975). Bray *et al.* (1991) con-

firms this result for cool coronal loops. Many two-fluid simulations have been developed for the solar wind (see for example Hollweg & Johnson 1988) and much of the physics remain the same for closed flux.

For a particular coronal loop solution, the code is allowed to reach steady-state before results can be taken and analysed. Details on the systematic approach of the iterative method adopted can be found in Section 3.3.

3.2.1 Basic Equations

The modelled time dependent continuity equation can be written as

$$\frac{\partial \rho}{\partial t} + \frac{1}{a}\frac{\partial (\rho v a)}{\partial s} = 0 \tag{3.1}$$

where ρ is the plasma mass density ($\rho \approx n_p m_p$ as $m_p \gg m_e$), v is the plasma velocity, a is the loop cross section (assumed to remain constant) and s is the position along the axis of the loop. Figure 3.1 demonstrates the loop structure and terms used for the modelled loops. Early work by authors such as Krieger *et al.* (1971), Poletto *et al.* (1975) and Rosner *et al.* (1978) strongly imply the existence of loops with constant cross sections. More recently, studies of *TRACE* data (Aschwanden *et al.*, 2000a) support early research. Chae *et al.* (2002) and Testa *et al.* (2005), for example model loops with this important finding in mind.

The momentum equation can be written as

$$\frac{\partial v}{\partial t} + v\frac{\partial v}{\partial s} = -\frac{1}{\rho}\frac{\partial \left(p_e + p_p + p_w\right)}{\partial s} - g_{\parallel} \tag{3.2}$$

where p_e, p_p and p_w are the electron, proton and turbulent wave pressure respectively

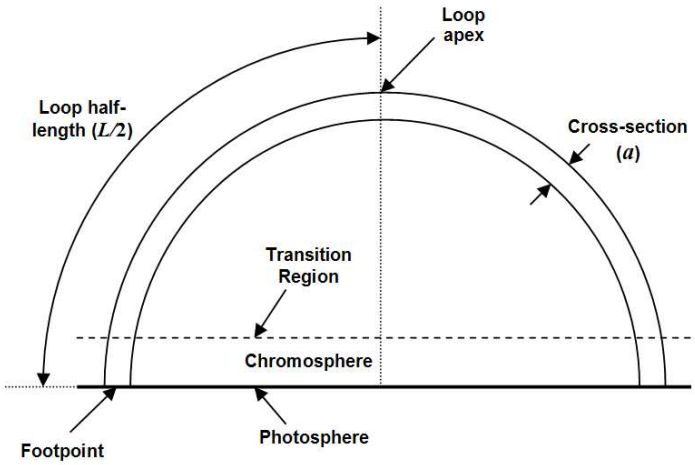

Figure 3.1: A schematic noting the nomenclature of coronal loop terms as used throughout this thesis. A semi-circular structure is assumed.

and $g_{\|}$ is the gravitational component acting on the plasma. $g_{\|}$ is expected to have a maximum deceleration (acceleration) effect on upflowing (downflowing) plasma. Naturally, $g_{\|} = 0$ at the loop apex (Eq. 3.10 demonstrates the specific way in which this parameter is treated). Our model is unique in that Alfvén waves are used. These waves will introduce momentum deposition to the loop plasma. Momentum deposition may play a very important role in pulling plasma from the chromosphere to the corona (Belcher & Davis, 1971, Belcher, 1971, Litwin & Rosner, 1998a,b, Winebarger *et al.*, 2002, Li & Habbal, 2003).

The electron and proton energy equations can be written as

$$\frac{\partial T_e}{\partial t} + v\frac{\partial T_e}{\partial s} + \frac{(\gamma-1)\,T_e}{a}\frac{\partial (va)}{\partial s}$$

$$= \frac{(\gamma-1)}{k_{\rm B} n a}\frac{\partial}{\partial s}\left[a\kappa_e \frac{\partial T_e}{\partial s}\right] + 2\nu_{pe}\left(T_p - T_e\right) - \frac{(\gamma-1)}{k_{\rm B} n} L_{\rm rad} \qquad (3.3)$$

$$\frac{\partial T_p}{\partial t} + v\frac{\partial T_p}{\partial s} + \frac{(\gamma-1)\,T_p}{a}\frac{\partial (va)}{\partial s}$$

$$= \frac{(\gamma-1)}{k_{\rm B} n a}\frac{\partial}{\partial s}\left[a\kappa_p \frac{\partial T_p}{\partial s}\right] + 2\nu_{pe}\left(T_e - T_p\right) + \frac{(\gamma-1)}{k_{\rm B} n} Q \tag{3.4}$$

where T_e and T_p are the electron and proton temperatures, n is the plasma density (plasma quasi-neutrality applies, $n_p \approx n_e = n$), k_B is the Boltzmann constant, κ_e and κ_p are the collision dominated electron and proton heat flux conductivities ($\kappa_e = 7.8{\times}10^{-7} T_e^{5/2}$, $\kappa_p = 3.2{\times}10^{-8} T_p^{5/2}$; Spitzer 1962). γ is the ratio of specific heats and for fully ionised hydrogen, $\gamma_{\rm H} = 5/3$. This value is used throughout. $L_{\rm rad}$ is the radiative energy loss from the loop and is considered to be one of the largest energy sinks in coronal loops. This parameter is strongly influenced by the density of electrons and is considered to be optically thin. Primarily, the value of $L_{\rm rad}$ used in this work is replicated from Rosner *et al.* (1978) (RTV)

$$L_{\rm rad}({\rm RTV}) = \begin{cases} 10^{-21.85} & \left(10^{4.3} < T < 10^{4.6}{\rm K}\right) \\ 10^{-31} T^2 & \left(10^{4.6} < T < 10^{4.9}{\rm K}\right) \\ 10^{-21.2} & \left(10^{4.9} < T < 10^{5.4}{\rm K}\right) \\ 10^{-10.4} T^{-2} & \left(10^{5.4} < T < 10^{5.75}{\rm K}\right) \\ 10^{-21.94} & \left(10^{5.75} < T < 10^{6.3}{\rm K}\right) \\ 10^{-17.73} T^{-2/3} & \left(10^{6.3} < T\right) \end{cases} \tag{3.5}$$

$L_{\rm rad}$ is determined from plasma abundances in the corona. Rosner *et al.* use coronal abundances as calculated from spectroscopic analysis. Fludra & Schmelz (1999) for example use the Bragg Crystal Spectrometer on *Yohkoh* to derive absolute coronal abundances for sulfur, calcium and iron using a filter ratio method. As one would expect, the different elements contained within solar plasma will radiate at different wavelengths (and therefore emit differing quantities of energy) and is very dependent on temperature. Equation 3.5 for example is an analytical expression for the abundance approximation and is therefore not exact and is dependent on the instrumentation available at

the time. Coronal abundance measurements improve with technology advances.

As a comparison, another radiative loss function is incorporated. More recent observed coronal abundances are used by Klimchuk & Cargill (2001) (KC)

$$L_{\rm rad}({\rm KC}) = \begin{cases} 10^{-30.96}T^{2} & \left(T \leq 10^{4.97}{\rm K}\right) \\ 10^{-16.05}T^{-1} & \left(10^{4.97} < T \leq 10^{5.67}{\rm K}\right) \\ 10^{-21.72} & \left(10^{5.67} < T \leq 10^{6.18}{\rm K}\right) \\ 10^{-12.45}T^{-3/2} & \left(10^{6.18} < T \leq 10^{6.55}{\rm K}\right) \\ 10^{-24.46}T^{1/3} & \left(10^{6.55} < T \leq 10^{6.90}{\rm K}\right) \\ 10^{-15.26}T^{-1} & \left(10^{6.3} < T\right) \end{cases} \tag{3.6}$$

In this case, Klimchuk & Cargill use more recent abundance data. A direct comparison is made between the two radiative loss functions in Section 3.8.

Additionally, work by Moriyasu *et al.* (2004) (MTTK) addresses an issue with a chromospheric imbalance in wave heating and excessive radiative loss (see Section 4.2)

$$L_{\rm rad}({\rm MTTK}) = 10^{9.69}\rho \quad ({\rm T} \leq 10^{4.6}{\rm K}) \tag{3.7}$$

Q is the turbulent heating rate of the dissipating wave (Hollweg, 1986), energy is therefore absorbed by the proton gas and emitted by the electron gas. Primarily, Q will be assumed to follow a Kolmogorov turbulent spectrum and defined as $Q = \rho\xi^3/l_{\rm drive}$ (Eq. 2.14).

We will work under the assumption that the non-thermal velocities observed by Chae *et al.* (1998) is the fingerprint of ξ (Section 2.4). Chae *et al.* find spectral lines observed in the transition region and corona (by the SUMER instrument on board *SOHO*) exhibit excess broadening of spectral lines beyond thermal broadening. The temperatures

analysed in this study range from 2×10^4K to 10^6K and the corresponding ξ range from 5kms^{-1} to 30kms^{-1}. The ξ vs. temperature curve for quiet-Sun disk observations plot is used, as detailed in Fig. 2.4, to read off the desired temperature and corresponding value of ξ.

ν_{pe} is the Coulomb collision frequency given by (Braginski, 1965)

$$\nu_{pe} = \frac{16\sqrt{\pi}}{3} \frac{ne^4 \ln \Lambda}{m_p m_e} \left[\frac{2k_B T_e}{m_e} \right]^{-3/2} \tag{3.8}$$

ν_{pe} is an important parameter as a mechanism to transport energy from protons (energized by resonant Alfvén waves) to the lower mass electrons. $\ln \Lambda$ is the Coulomb logarithm ($\ln \Lambda$=23 in this study as the lower corona is considered to be collision dominated).

Finally, the Alfvén wave energy equation can be written as

$$\frac{\partial p_w}{\partial t} + \frac{1}{a} \frac{\partial}{\partial s} \left[a \left(1.5v + v_A \right) p_w \right] - \frac{v}{2} \frac{\partial p_w}{\partial s} + \frac{Q}{2} = 0 \tag{3.9}$$

where v is the plasma flow speed, p_w is the wave pressure (given by $p_w = \rho \xi^2/2$; Li & Habbal 2003) and v_A is the local Alfvén velocity (Eq. 2.1).

Figure 3.2 shows the inclination (and arc length, s) in relation to the loop structure. The inclination angle (χ) is taken as the angle from the vertical. As investigated by Tsiklauri & Nakariakov (2001), it was found that the small difference in gravitational acceleration has a large influence on coronal loop dynamics, particularly when considering MHD waves. Of particular interest is how the plasma flow and loop temperature may be affected by a non-zero χ. Aschwanden *et al.* (2000a) performed a detailed analysis on 35 loops in the temperature range of 1.5-2.5MK. It was found that the average inclination was ~35°, ranging from 0° to 80°, therefore suggesting most loops are not vertical.

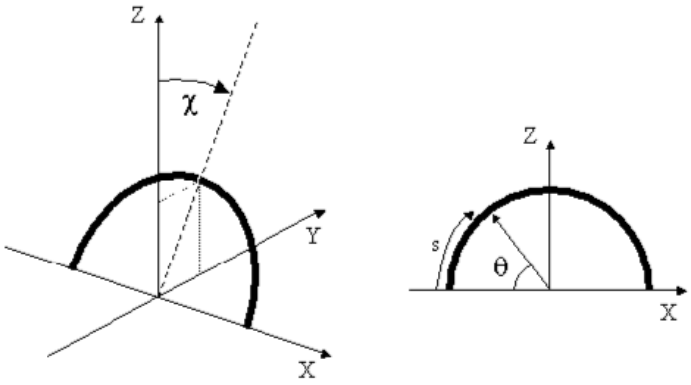

Figure 3.2: Schematic of the coronal loop described by the gravity equation (Eq. 3.10).

Some results from this study are presented in Fig. 4.15.

The gravity term in Eq. 3.2 can be treated as follows

$$g_{\parallel} = \frac{GM_{\odot}}{[R_{\odot} + h(s)\cos\chi]^2}\cos\theta\cos\chi \tag{3.10}$$

It should be noted that there is an extra $\cos\chi$ term in the denominator of Eq. 3.10. We are dealing with an inclined loop (non-zero χ), therefore there will be a small decrease in the vertical extent (h) of the loop. This will affect the gravity term only very slightly, but has been included for completeness as long loops may be affected strongly by this factor.

3.2.2 Compact Form of Basic Equations

To introduce the numerical method (the full implicit treatment is detailed in Section 3.2.4), the basic equations (Section 3.2.1) are cast into the following compact form

$$\frac{\partial U}{\partial t} + W\left(U, \frac{\partial U}{\partial s}, \frac{\partial^2 U}{\partial s^2}\right) = 0 \tag{3.11}$$

where t is time and s is the arc length of the loop. U represents the plasma parameters and W is derived from the basic equations. U and W are given by

$$U = \begin{bmatrix} n \\ v \\ T_e \\ T_p \\ p_w \end{bmatrix}, \quad W = \begin{bmatrix} W_1 \\ W_2 \\ W_3 \\ W_4 \\ W_5 \end{bmatrix} \tag{3.12}$$

W_i is expressed in the following manner

$$W_1 = n\frac{\partial v}{\partial s} + v\frac{\partial n}{\partial s} + \frac{nv}{a}\frac{\mathrm{d}a}{\mathrm{d}s} \tag{3.13}$$

$$W_2 = v\frac{\partial v}{\partial s} + \frac{k_\mathrm{B}T_p}{m_p n}\frac{\partial n}{\partial s} + \frac{k_\mathrm{B}}{m_p}\frac{\partial T_e}{\partial s} + \frac{k_\mathrm{B}T_p}{m_p n}\frac{\partial n}{\partial s} + \frac{k_\mathrm{B}}{m_p}\frac{\partial T_p}{\partial s} + \frac{1}{m_p n}\frac{\partial p_w}{\partial s} + g_\parallel \tag{3.14}$$

$$W_3 = v\frac{\partial T_e}{\partial s} + (\gamma-1)T_e\frac{\partial v}{\partial s} - \frac{(\gamma-1)\kappa_e T_e^{5/2}}{k_\mathrm{B}n}\frac{\partial^2 T_e}{\partial s^2} - \frac{5(\gamma-1)\kappa_e T_e^{3/2}}{2k_\mathrm{B}n}\left(\frac{\partial T_e}{\partial s}\right)^2$$

$$-\frac{(\gamma-1)\kappa_e T_e^{5/2}}{k_\mathrm{B}na}\frac{\mathrm{d}a}{\mathrm{d}s}\frac{\partial T_e}{\partial s} + \frac{(\gamma-1)vT_e}{a}\frac{\mathrm{d}a}{\mathrm{d}s} - 2C_{pe}T_e^{-3/2}n\left(T_p - T_e\right) + \frac{(\gamma-1)}{k_\mathrm{B}n}L_\mathrm{rad} \tag{3.15}$$

$$W_4 = v\frac{\partial T_p}{\partial s} + (\gamma-1)T_p\frac{\partial v}{\partial s} - \frac{(\gamma-1)\kappa_p T_p^{5/2}}{k_\mathrm{B}n}\frac{\partial^2 T_p}{\partial s^2} - \frac{5(\gamma-1)\kappa_p T_p^{3/2}}{2k_\mathrm{B}n}\left(\frac{\partial T_p}{\partial s}\right)^2$$

$$-\frac{(\gamma-1)\kappa_p T_p^{5/2}}{k_\mathrm{B}na}\frac{\mathrm{d}a}{\mathrm{d}s}\frac{\partial T_p}{\partial s} + \frac{(\gamma-1)vT_p}{a}\frac{\mathrm{d}a}{\mathrm{d}s} + 2C_{pe}T_e^{-3/2}n\left(T_p - T_e\right) + \frac{(\gamma-1)}{k_\mathrm{B}n}Q \tag{3.16}$$

$$W_5 = \left(\frac{v_\mathrm{A}}{a}\frac{1}{\sqrt{n}} + v\right)\frac{\partial p_w}{\partial s} + \frac{3p_w}{2}\frac{\partial v}{\partial s} - \frac{v_\mathrm{A} p_w}{2an}\frac{1}{\sqrt{n}}\frac{\partial n}{\partial s} + \frac{3vp_w}{2a}\frac{\mathrm{d}a}{\mathrm{d}s} \tag{3.17}$$

where C_{pe} is the conductivity between proton and electron given by

$$C_{pe} = \frac{4\sqrt{2\pi m_e}e^4 \ln\Lambda}{3m_p k_\mathrm{B}^{3/2}} \tag{3.18}$$

3.2.3 Expressions for the Derivatives of W ($\partial W/\partial U$)

The derivatives of W can now be summerised. The elements of $\partial W/\partial U$ can be cast into the following matrix

$$\frac{\partial W}{\partial U} = \begin{bmatrix} \frac{\partial W_1}{\partial n} & \frac{\partial W_1}{\partial v} & 0 & 0 & 0 \\ \frac{\partial W_2}{\partial n} & \frac{\partial W_2}{\partial v} & \frac{\partial W_2}{\partial T_e} & \frac{\partial W_2}{\partial T_p} & 0 \\ \frac{\partial W_3}{\partial n} & \frac{\partial W_3}{\partial v} & \frac{\partial W_3}{\partial T_e} & \frac{\partial W_3}{\partial T_p} & 0 \\ \frac{\partial W_4}{\partial n} & \frac{\partial W_4}{\partial v} & \frac{\partial W_4}{\partial T_e} & \frac{\partial W_4}{\partial T_p} & 0 \\ \frac{\partial W_5}{\partial n} & \frac{\partial W_5}{\partial v} & 0 & 0 & \frac{\partial W_5}{\partial p_w} \end{bmatrix} \tag{3.19}$$

The expressions noted in the $\partial W/\partial U$ matrix (Eq. 3.19) are listed below. For W_1 (Eq. 3.13), $\partial W_1/\partial U$ results in:

$$\frac{\partial W_1}{\partial n} = \frac{\partial v}{\partial s} + \frac{v}{a}\frac{\mathrm{d}a}{\mathrm{d}s}$$

$$\frac{\partial W_1}{\partial v} = \frac{\partial n}{\partial s} + \frac{n}{a}\frac{\mathrm{d}a}{\mathrm{d}s}$$

$$\frac{\partial W_1}{\partial T_e} = \frac{\partial W_1}{\partial T_p} = \frac{\partial W_1}{\partial p_w} = 0 \tag{3.20}$$

For W_2 (Eq. 3.14):

$$\frac{\partial W_2}{\partial n} = -\frac{k_\mathrm{B}\left(T_e + T_p\right)}{m_p n^2}\frac{\partial n}{\partial s} - \frac{1}{m_p n^2}\frac{\partial p_w}{\partial s}$$

$$\frac{\partial W_2}{\partial v} = \frac{\partial v}{\partial s}$$

$$\frac{\partial W_2}{\partial T_e} = \frac{k_\mathrm{B}}{m_p n}\frac{\partial n}{\partial s}$$

$$\frac{\partial W_2}{\partial T_p} = \frac{k_\mathrm{B}}{m_p n}\frac{\partial n}{\partial s}$$

$$\frac{\partial W_2}{\partial p_w} = 0 \tag{3.21}$$

For W_3 (Eq. 3.15):

$$\frac{\partial W_3}{\partial n} = \frac{(\gamma-1)\,\kappa_e T_e^{5/2}}{k_\mathrm{B} n^2}\frac{\partial^2 T_e}{\partial s^2} + \frac{5\,(\gamma-1)\,\kappa_e T_e^{3/2}}{2 k_\mathrm{B} n^2}\left(\frac{\partial T_e}{\partial s}\right)^2$$

$$+\frac{(\gamma-1)\,\kappa_e T_e^{5/2}}{k_\mathrm{B} n^2 a}\frac{\mathrm{d}a}{\mathrm{d}s}\frac{\partial T_e}{\partial s} - 2C_{pe}T_e^{-3/2}\left(T_p - T_e\right)$$

$$\frac{\partial W_3}{\partial v} = \frac{\partial T_e}{\partial s} + \frac{(\gamma-1)\,T_e}{a}\frac{\mathrm{d}a}{\mathrm{d}s}$$

$$\frac{\partial W_3}{\partial T_e} = (\gamma - 1)\frac{\partial v}{\partial s} - \frac{5(\gamma-1)\kappa_e T_e^{3/2}}{2k_{\mathrm{B}}n}\frac{\partial^2 T_e}{\partial s^2} + \frac{15(\gamma-1)\kappa_e T_e^{1/2}}{4k_{\mathrm{B}}n}\left(\frac{\partial T_e}{\partial s}\right)^2$$

$$+\frac{5(\gamma-1)\kappa_e T_e^{3/2}}{2k_{\mathrm{B}}na}\frac{\mathrm{d}a}{\mathrm{d}s}\frac{\partial T_e}{\partial s} + \frac{(\gamma-1)v}{a}\frac{\mathrm{d}a}{\mathrm{d}s} + C_{pe}T_e^{-3/2}n\left(\frac{3T_p}{T_e - 1}\right)$$

$$\frac{\partial W_3}{\partial T_p} = -2C_{pe}n\left(T_p - T_e\right)$$

$$\frac{\partial W_3}{\partial p_w} = 0 \tag{3.22}$$

For W_4 (Eq. 3.16):

$$\frac{\partial W_4}{\partial n} = \frac{(\gamma-1)\kappa_p T_p^{5/2}}{k_{\mathrm{B}}n^2}\frac{\partial^2 T_p}{\partial s^2} + \frac{5(\gamma-1)\kappa_p T_p^{3/2}}{2k_{\mathrm{B}}n^2}\left(\frac{\partial T_p}{\partial s}\right)^2$$

$$+\frac{(\gamma-1)\kappa_p T_p^{5/2}}{k_{\mathrm{B}}n^2 a}\frac{\mathrm{d}a}{\mathrm{d}s}\frac{\partial T_p}{\partial s} + 2C_{pe}T_e^{-3/2}\left(T_p - T_e\right)$$

$$\frac{\partial W_4}{\partial v} = \frac{\partial T_p}{\partial s} + \frac{(\gamma-1)T_p}{a}\frac{\mathrm{d}a}{\mathrm{d}s}$$

$$\frac{\partial W_4}{\partial T_e} = -C_{pe}T_e^{-3/2}n\left(\frac{3T_p}{T_e - 1}\right)$$

$$\frac{\partial W_4}{\partial T_p} = (\gamma - 1)\frac{\partial v}{\partial s} - \frac{5(\gamma-1)\kappa_p T_p^{3/2}}{2k_{\mathrm{B}}n}\frac{\partial^2 T_p}{\partial s^2} + \frac{15(\gamma-1)\kappa_p T_p^{1/2}}{4k_{\mathrm{B}}n}\left(\frac{\partial T_p}{\partial s}\right)^2$$

$$+\frac{5(\gamma-1)\kappa_p T_p^{3/2}}{2k_{\mathrm{B}}na}\frac{\mathrm{d}a}{\mathrm{d}s}\frac{\partial T_p}{\partial s} + \frac{(\gamma-1)v}{a}\frac{\mathrm{d}a}{\mathrm{d}s} + 2C_{pe}n\left(T_p - T_e\right)$$

$$\frac{\partial W_4}{\partial p_w} = 0 \tag{3.23}$$

For W_5 (Eq. 3.17):

$$\frac{\partial W_5}{\partial n} = -\frac{v_{A0}}{2an^{3/2}}\frac{\partial p_w}{\partial s} + \frac{3v_{A0}p_w}{4n^{5/2}a}\frac{\partial n}{\partial s}$$

$$\frac{\partial W_5}{\partial v} = \frac{\partial p_w}{\partial s} + \frac{3p_w}{2a}\frac{\mathrm{d}a}{\mathrm{d}s}$$

$$\frac{\partial W_5}{\partial T_e} = \frac{\partial W_5}{\partial T_p} = 0$$

$$\frac{\partial W_5}{\partial p_w} = \frac{v_{A0}}{an^{3/2}} - \frac{v_{A0}}{2an^{3/2}}\frac{\partial n}{\partial s} + \frac{3v}{2a}\frac{\mathrm{d}a}{\mathrm{d}s} \tag{3.24}$$

3.2.4 The Full-Implicit Scheme

Now the basic equations are cast into the W vector (Eq. 3.12) and then differentiated and cast into the $\partial W/\partial U$ matrix (Eq. 3.19), the numerical method can evaluate these terms to solve the following difference equations in the aim of arriving at a stable (steady-state) solution. From Lindemuth & Killeen (1973) and Hu (1989)

$$\frac{1}{\Delta t}\left[U_j^{n+1} - U_j^n\right] + W_j^{n+1} = 0 \tag{3.25}$$

where

$$U_j^{n+1} \equiv U\left(t^{n+1}, s_j\right), \quad U_j^n \equiv U\left(t^n, s_j\right), \quad t^{n+1} = t^n + \Delta t \tag{3.26}$$

$$W_j^{n+1} = W_j^n + \left(\frac{\partial W}{\partial U}\right)_j^n \left[U_j^{n+1} - U_j^n\right] + \left(\frac{\partial W}{\partial(\partial U/\partial s)}\right)_j^n \left[\left(\frac{\partial U}{\partial s}\right)_j^{n+1} - \left(\frac{\partial U}{\partial s}\right)_j^n\right]$$

$$\left(\frac{\partial W}{\partial(\partial^2 U/\partial s^2)}\right)_j^n \left[\left(\frac{\partial^2 U}{\partial s^2}\right)_j^{n+1} - \left(\frac{\partial^2 U}{\partial s^2}\right)_j^n\right] \tag{3.27}$$

This is a Taylor expansion of the W_j^{n+1} term. $(\partial U/\partial s)_j$ and $(\partial U^2/\partial s^2)_j$ can be evaluated in terms of a central difference approximation as follows

$$\left(\frac{\partial U}{\partial s}\right)_j = \frac{U_{j+1} - U_{j-1}}{s_{j+1} - s_{j-1}}, \quad \left(\frac{\partial^2 U}{\partial s^2}\right)_j = \frac{2}{s_{j+1} - s_{j-1}}\left(\frac{U_{j+1} - U_j}{s_{j+1} - s_j} - \frac{U_j - U_{j-1}}{s_j - s_{j-1}}\right) \tag{3.28}$$

Equations 3.27 and 3.28 are then inserted into the implicit equation (Eq. 3.25) to form a tridiagonal set of algebraic equations

$$A_j U_j^{n+1} + B_j U_{j+1}^{n+1} + C_j U_{j-1}^{n+1} = E_j \tag{3.29}$$

where A_j, B_j and C_j are 5×5 matrices and E_j is a 5 dimensional vector. U_j remains a vector of the 5 plasma parameters used in this model (Eq. 3.12). A_j, B_j, C_j and E_j can be summarised as follows

$$A_j = \frac{I}{\Delta t} + \left(\frac{\partial W}{\partial U}\right)_j^n - \frac{2}{(r_{j+1} - r_j)(r_j - r_{j-1})}\left(\frac{\partial W}{\partial\left(\partial^2 U/\partial r^2\right)}\right)_j^n,$$

$$B_j = \frac{2}{(r_{j+1} - r_{j-1})(r_{j+1} - r_j)}\left(\frac{\partial W}{\partial\left(\partial^2 U/\partial r^2\right)}\right)_j^n + \frac{1}{r_{j+1} - r_{j-1}}\left(\frac{\partial W}{\partial\left(\partial U/\partial r\right)}\right)_j^n,$$

$$C_j = \frac{2}{(r_{j+1} - r_{j-1})(r_j - r_{j-1})}\left(\frac{\partial W}{\partial\left(\partial^2 U/\partial r^2\right)}\right)_j^n + \frac{1}{r_{j+1} - r_{j-1}}\left(\frac{\partial W}{\partial\left(\partial U/\partial r\right)}\right)_j^n,$$

$$E_j = -W_j^n + \left[\frac{I}{\Delta t} + \left(\frac{\partial W}{\partial U}\right)_j^n\right] U_j^n + \left(\frac{\partial W}{\partial\left(\partial U/\partial r\right)}\right)_j^n \left(\frac{\partial U}{\partial r}\right)_j^n + \left(\frac{\partial W}{\partial\left(\partial^2 U/\partial r^2\right)}\right)_j^n \left(\frac{\partial^2 U}{\partial r^2}\right)_j^n \quad (3.30)$$

The set of tridiagonal equations indicated above can be cast into the following form

$$\begin{bmatrix} A_1 & B_1 & 0 & 0 & 0 \\ C_2 & A_2 & B_2 & 0 & 0 \\ 0 & C_{N-2} & A_{N-2} & B_{N-2} & 0 \\ 0 & 0 & C_{N-1} & A_{N-1} & B_{N-1} \\ 0 & 0 & 0 & C_N & A_N \end{bmatrix} \cdot \begin{bmatrix} U_1 \\ U_2 \\ U_{N-2} \\ U_{N-1} \\ U_N \end{bmatrix} = \begin{bmatrix} E_1 \\ E_2 \\ E_{N-2} \\ E_{N-1} \\ E_N \end{bmatrix} \quad (3.31)$$

where the subscript N is the total number of parameters and I is a unit vector. The above equations can be evaluated using a conventional push-pull method. Primarily, the method must define and evaluate the matrix, Q, and the vector, V, from the algebraic equations $AQ = B$ and $AV = E$. The Gaussian elimination method is used to solve matrices of this form. Beginning with the first row in Eq. 3.31, the first expression can be treated as

$$A_1 U_1 + B_1 U_2 = E_1 \quad \rightarrow \quad A_1^{-1} A_1 U_1 + A_1^{-1} B_1 U_2 = A_1^{-1} E_1 \quad (3.32)$$

We can now define $Q_1 = A_1^{-1} B_1$ and $V_1 = A_1^{-1} E_1$. The matrices A_1, B_1 and E_1 will be defined by the boundary conditions. Equation 3.32 becomes

$$U_1 + Q_1 U_2 = V_1 \quad (3.33)$$

The second expression to arise from Eq. 3.31 can be treated as

$$A_2 U_2 + B_3 U_3 + C_2 U_1 = E_2$$

Substituting for U_1 (rearranging Eq. 3.33)

$$A_2U_2 + B_3U_3 + C_2\left(V_1 - Q_1U_2\right) = E_2$$

rearranging

$$\left(A_2 - C_2Q_1\right)U_2 + B_3U_3 = E_2 - C_2V_1 \tag{3.34}$$

Let $Q_2 = (A_2 - C_2Q_1)^{-1}B_3$, rearranging for B_3, Eq. 3.34 becomes

$$U_2 + Q_2U_3 = \left(A_2 - C_2Q_1\right)^{-1}\left(E_2 - C_2V_1\right)$$

Now let $V_2 = \left(A_2 - C_2Q_1\right)^{-1}\left(E_2 - C_2V_1\right)$, Eq. 3.34 can be reduced to

$$U_2 + Q_2U_3 = V_2 \tag{3.35}$$

By comparing Eq. 3.33 and Eq. 3.35, it is evident they share the same form. It is now possible to derive general expressions for the components of the matrix of Eq. 3.31. Therefore

$$U_{j-1} + Q_{j-1}U_j = V_{j-1} \tag{3.36}$$

and

$$Q_j = (A_j - C_jQ_{j-1})^{-1}B_j\,, \quad V_j = (A_j - C_jQ_{j-1})^{-1}(E_j - C_jV_{j-1}) \tag{3.37}$$

where $j = 2, 3...N-1, N$.

At the limit of calculation, where $j = N$ (as is evident at the base of the matrix in Eq. 3.31 where $C_N U_{N-1} + A_N U_N = E_N$), $U_{N-1} + Q_{N-1} U_N = V_{N-1}$. In this case $B_N = 0$ and the matrices A_N, C_N and E_N will be defined by the boundary conditions. Combining these equations results in $C_N(V_{N-1} - Q_{N-1} U_N) + A_N U_N = E_N$. U_N can now be determined. From Eq. 3.36, U_{N-1} can be found. Therefore

$$V_{j-1} - Q_{j-1} U_j = U_{j-1} \tag{3.38}$$

where $j = N, N-1, ...3, 2$.

3.2.5 Boundary Conditions

A steady flow of plasma is assumed during the steady-state phase of the loop lifetime. We also assume a magnetic field strength of 80G (typical magnetic field strengths in coronal loops are 50-100G; Lenz 1999). The footpoints have a starting temperature of 20,000K (both electrons and protons are assumed to be equilibrium), but may change as different values of ξ are used (due to the photospheric temperature and ξ relationship;Chae *et al.* 1998). ξ is fixed at the upflowing footpoint (s=0) but is allowed to change as the waves propagate around the loop, totally dissipating at $s = L$. Both footpoints are free boundaries for density and plasma flow velocity, it is the energy flux of the upflowing waves that characterise the coronal loop density and plasma flow.

3.3 Iterative Method

During experimentation with many solutions, it was found an iterative method had to be applied to the code. If the initial 'guess' solution is too far from steady-state (i.e.

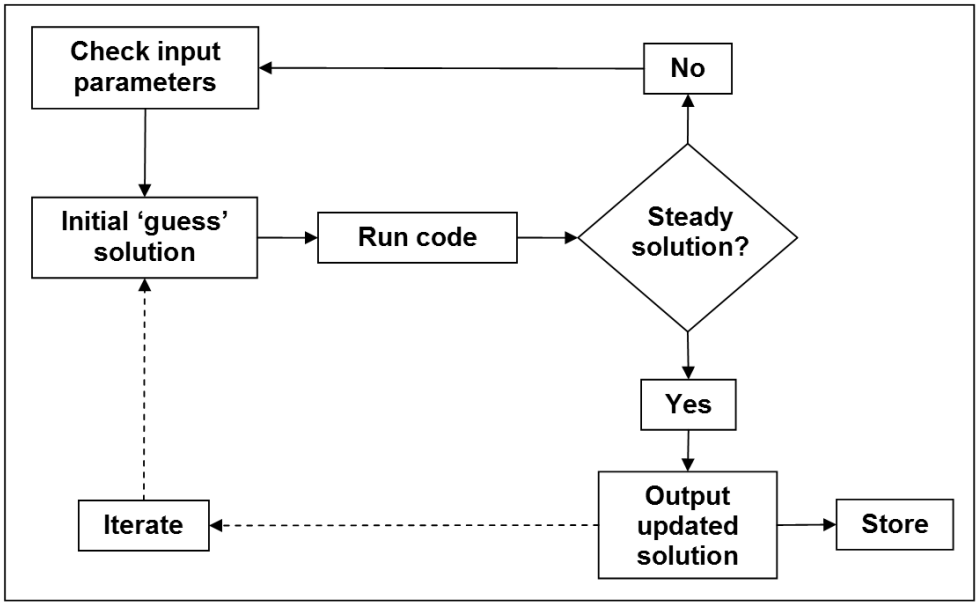

Figure 3.3: Flow chart of the iterative method

after undergoing the lengthening process, Section 3.6, or on attempting to aquire an extreme final solution), the code will break down due to its inability to cope with extreme changes in the plasma parameters. The code is particularly sensitive to any variation in l_{drive} and ξ (Eq. 2.15, i.e. variation in the turbulent heating rate).

Figure 3.3 graphically shows the system used in the iterative method. Firstly we have the initial *guess* solution. Strictly speaking this is not a guess solution, more of an *educated guess* solution. For the numerical method to begin processing the data, the input solution must have ξ and l_{drive} values fairly close to what the code is expecting. For example, if the input solution is taken from a hot loop, heated by very energetic waves with strong turbulence, to apply it to a code that has been set up to output a cool solution heated by low energy waves, it is highly unlikely steady-state will be possible. Therefore there must be some consideration as to how the input solution relates to the output solution. If steady-state is not achieved, the input data must be re-evaluated, altering the variables until a *first-run* is achieved. Once the first solution is computed it is a relatively easy task to tune the parameters toward the desired final values of ξ and

l_{drive} in small iterative steps.

Although each iterative step is necessary to progress to the final desired solution, each iteration need not be wasted. At logical points, each iteration is stored for later use. One such use is apparent during the parameter study carried out in Chapter 4. During the construction of the contour maps in parameter space these iterations could be applied to form the smooth contouring evident in Figs. 4.1, 4.3 and 4.4.

3.4 Numerical Simulation Units (NSU)

Le Systeme International (SI) units are commonly used in most areas of physics. Astrophysical studies often use Gaussian (CGS) units. Within the full-implicit environment of the numerical code outlined in this study, all the parameters are converted and calculated in Numerical Simulation Units (NSU). Once the code has calculated the basic equations (Section 3.2.1), the output parameters are converted from NSU to Gaussian/SI units for further analysis. All units prior to this section have been in the Gaussian regime (centimetres, grams, seconds). During the simulation stage of this study, the units deviate into the NSU regime. Once solutions are gained and analysis of simulation data can begin, parameters such as temperature (T) and loop length (L) are simplified to the units of MK (million Kelvin) and Mm (million metres) respectively. This improves clarity of the large scales under interpretation.

The NSU system is very important in the case of any solar wind/coronal loop models. We are dealing extremely large (in the case of plasma number density, $n \approx 10^{8}\text{cm}^{-3}$) and very small (in the case of particle mass, $m \approx 10^{-24}\text{g}$) numbers, there is therefore a risk of exponential explosions and lack of precision in results. To combat this problem, the following basic units are applied keeping in mind the magnitude of average solar values (Hu, 1989)

(i) Length: d=10^{10}cm

(ii) Velocity: v=10^{7}cms^{-1}

(iii) Mass: m=10^{-24}g

(iv) Number density: n=10^{8}cm^{-3}

(v) Temperature: T=10^{6}K

For example, the proton mass measures $m_{\rm p}$=1.67×10^{-24}g in CGI units. As mass has the unit of 10^{-24}g in the NSU system, the proton mass will now have a reading of 1.67. It is obvious the NSU system will make the parameters far easier to manage and calculate.

The basic units permeate through the derived units. From dimensional analysis, the simple derivation of time to the derivation of magnetic flux demonstrates how the derived units are treated:

Example 1: v=d/t. The dimensions for t are $[d][v]^{-1}$. d has the unit of 10^{10}cm and v has the unit of 10^{7}cms^{-1}. In the NSU system, t will therefore have the unit of 10^{3}s.

Example 2: $v_{\rm A}$=$B/\sqrt{4\pi\rho}$. The dimensions for B are $[v][\rho]^{1/2}$. v has the unit of 10^{7}cms^{-1} and ρ has the unit of 10^{-16}g cm^{-3} (derived from the analysis of ρ=$nm_{\rm p}$). In the NSU system, B will therefore have the unit of 10^{-1}G.

After consideration for the scaling of the NSU system is taken into account, the basic parameters can be arranged in their associated basic equations (Section 3.2.1) and cast into the the numerical method (Section 3.2.4). Once the numerical method converges to steady-state, the outputted NSU results are converted back to Gaussian or SI units for analysis.

3.5 The First Solution

The primary solution to be inputted into the simulation is studied in Li & Habbal (2003). In this work, one loop of length 70Mm is used. As already mentioned, the numerical method (Section 3.2.4) originates from solar wind simulations. This is the starting point for this numerical model in that the very first coronal loop solution originates from a two-fluid solar wind model solution.

The magnetic flux is open in the solar wind, it is closed for coronal loops, but the plasma characteristics are very similar. By manipulating a two-fluid solar wind solution, one can arrive at a coronal loop solution. A solar wind solution can be taken, cropped at a certain altitude, duplicated and mirrored. This can produce a crude but manageable coronal loop primary solution where the solar wind solution will now be anchored at both ends and gravity stratification will govern the plasma dynamics. Rather than beginning at a gravity maximum at the solar surface and decreasing as solar flux extends into interplanetary space (in the solar wind case), the gravity term for a coronal loop dictates that the semi-circular loops gravitational energy will begin at a maximum and end at a maximum (at the solar surface).

The numerical method will have difficulties in converging to a steady solution from this raw data set due to a rapid reversal in plasma parameters (particularly at the loop apex), so very fine adjustments are required during the iterative process (Section 3.3). Once convergence is achieved however, the plasma parameter variation will be minimised, so the output solution will be used for subsequent experimentation.

3.6 Loop Lengthening

For any detailed work, the loop must be lengthened (and shortened) and must have a smooth parameter transition from one grid point to the next. It is a necessary progression in this study to experiment with a range of loop lengths. Aschwanden (2002b) summarises observations of a selection of EUV coronal loops and relevant data is extracted and presented in Table 3.1. This data is an indication of the lengths of EUV loops expected in the corona. From the first row in Table 3.1, the range of loop *half* lengths is 37-291Mm, in which case it seems reasonable to construct loops with *total* lengths of 80-600Mm. Also, observations suggest the existence of shorter, cool loops. Work by Sakai *et al.* (2001) follows up suggestions by Aschwanden *et al.* (2000a) and observations by *TRACE* that a possible unidentified energy source heats the corona at an altitude of no higher than 16Mm. Therefore Sakai *et al.* (2001) work with shorter loops with lengths of just under 10Mm in an attempt to probe the low corona. In this study, lengths will range between 10-600Mm to cater for this observed range.

Table 3.1: Physical parameters averaged for 26 oscillating EUV loops - selected data from Aschwanden (2002b). *The range value for the loop extent is not an observed quantity, found from loop half length data (πr=2L), assuming zero inclination.

Parameter	Average	Range
Loop half length, L:	110±53Mm	37-291Mm
Extent, h*:	-	24-185Mm
Loop width, w:	8.7±2.8Mm	5.5-16.8Mm

In order to lengthen and shorten the loop solutions, an IDL routine is constructed. The main components of the routine involves calculating the exponential increase in grid-point spacing and reading the basic parameter values at each point. The grid spacing is an important factor when considering the scale of perturbations in the modelled coronal loop plasma. The primary solution has enough grid points to support a larger spacing between points. It is therefore an easy task to incorporate a small multiplying factor in

the grid spacing to gradually *stretch* the modelled loop to the desired length. Problems often occur with longer loops (i.e. loops of length L >300Mm required better resolution between points), so extra grid points can be inserted to smooth the transition of plasma parameters from one grid point to the next. The values for each additional grid point is the average value of the two adjacent grid points.

Shorter loops are also required, so the converse action can be taken. When shrinking the loop, a dividing factor can be introduced decreasing in grid point spacing, increasing the resolution. This is not always beneficial. Grid points in this case may be removed in sections of the loop where they are superfluous (particularly in the coronal section). The maximum number of grid points in the longest loops does not exceed 1350 and for the shortest loops considered, the minimum number is no lower than 1160. The range in grid point spacing for long loops used in this study is approximately 15m (at footpoint) to 1Mm (at loop apex). There is sufficient spacial resolution along the coronal loop model to detect small-scale parameter variations low in the corona and large scale parameter variations high in the corona.

It is assumed the Alfvén waves in this thesis propagate in the Wentzel-Kramer-Brillouin (WKB) limit. This approximation requires the propagating wave to have wavelengths smaller than the length-scale of variations in the medium that it is propagating through (hence the attention to higher resolution of grid points close to the surface than to high in the corona). Although McKenzie (1994) states the WKB approximation breaks down close to the Sun, due to small-scale variations in the medium approaching similar scales to the small wavelengths of propagating waves, this work assumes WKB remains a good approximation. Wave momentum deposition will be small close to the Sun (Hollweg, 1986), so any violation of the WKB approximation will be negligible to results.

Grid point spacing will affect the spacial resolution of the model. Although temporal resolution is secondary to this (as we are only modelling steady-state loops, the evolu-

tion plasma parameters is generally ignored), the calculation time-step in the numerical method becomes increasingly important at the boundary between temperature inversion solutions and shocked solutions. As plasma flow increases, shocks may form (as $v > c_s$) causing numerical instabilities. Shocks may only be modelled by this numerical method if the temporal resolution is increased (i.e. decreasing the calculation timestep). The range of shocked solutions are small (as discontinuities in plasma parameters are very difficult to model) but are detailed in Section 5.7.

3.7 Confirmation of Steady State

After rigorous testing of the numerical method as applied in this fashion, it was found that for all the loops of various lengths, steady state could be achieved very quickly when running the code. In reality, quiescent coronal loops have lifetimes of the order of hours to days (see Fig. 1.13 in Chapter 1 for a time series of 24 hours where the coronal loop morphology does not change appreciably). The *total simulation time* is not required to be as long as the *total lifetime* of the coronal loop, only as long as it takes for there to be no appreciable change in parameter stability over time (i.e. the achievement of steady state). The model is very efficient at reaching steady state, so generally, the total simulation time is set to the minimum time for any fluctuation in parameters or wave propagation to traverse the whole loop length. Steady state is reached within minutes, but the model time is usually set in the order of hours, so steady state is assured. Even though a steady solution may be outputted by the code, confirmation of a balance between the energy sources and sinks along the loop length must be arrived at. Only then will the final solution be considered to be in a steady state time- and parameter-wise.

In the coronal loop body, energy sources include gravity, wave, enthalpy and kinetic

energy flux. Energy sinks include conduction and radiation. For steady state to be achieved, all these energy fluxes must balance and be constant along the loop length. Equation 3.39 describes the energy flux balance

$$\underbrace{\left[\underbrace{\left(3+\frac{2}{M_A}\right)p_w}_{\text{Wave}}+\underbrace{\frac{\gamma nk\left(T_e+T_p\right)}{\gamma-1}}_{\text{Enthalpy}}+\underbrace{\int_0^s\frac{nm_pGM_o\cos\theta(s)\cos\chi}{\left[R_0+h(s)\cos\chi\right]^2}}_{\text{Gravity}}+\underbrace{\frac{1}{2}nm_pv^2}_{\text{KE}}\right]va}$$
$$\underbrace{-\kappa_e a\frac{dT_e}{ds}-\kappa_p a\frac{dT_p}{ds}}_{\text{Conductivities}}+\underbrace{a\int_0^s L_{rad}ds}_{\text{Radiation}}=H \tag{3.39}$$

where $M_\mathrm{A}=v/v_\mathrm{A}$ is the Alfvén Mach number and H is a constant. The above energy fluxes can be plotted and analysed to see if the H term does indeed remain *constant*. The degree of how constant H remains reflects the accuracy of the numerical method. Conductive energy flux is influenced by the temperature gradient along the loop (i.e. $-dT_e/ds$) and will therefore be negative in the upflowing footpoint (as temperature increases rapidly) and positive in the downflowing footpoint (as temperature decreases rapidly). Any large deviation in the total energy flux would reveal inaccuracies or errors in the code. Figure 3.4 is an example plot of the energy analysis of a 600Mm loop in steady state. The total energy flux remains constant within an error margin of 1%, demonstrating the very high accuracy of this method.

The loop length described in Fig. 3.4 demonstrates an obvious *double-hump* in temperature profile. During preliminary studies it was assumed the local temperature minimum and secondary local temperature maximum (above the right footpoint) was due to transfer of kinetic energy from near-supersonic plasma flow. Generally, all modelled loops beyond 200Mm in length exhibit a similar *double-hump* temperature profile at very low driving scales and high flow velocities. However, on analysis of loop energy flux across all loop lengths, it is obvious kinetic energy flux is minuscule when compared to gravity flux and enthalpy flux. It is logical to conclude that *it is the release of gravitational*

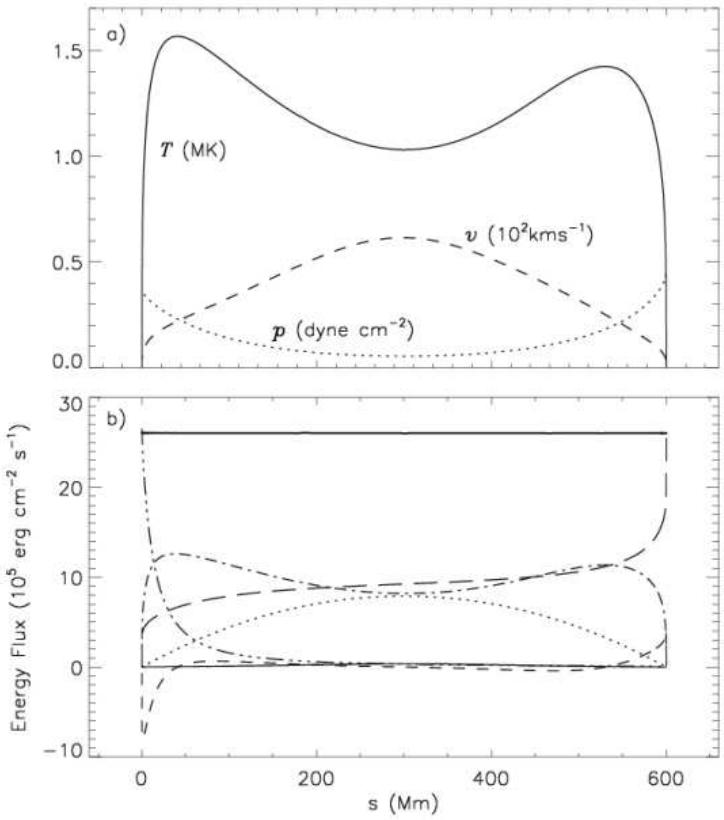

Figure 3.4: Balance of energy flux along a loop of length $L = 600$Mm. In the top frame (a), proton temperature (*solid line*), pressure (*dotted line*) and velocity (*dashed line*) along the loop are plotted. The bottom frame (b) compares the plasma parameters with the various energy fluxes. Kinetic energy flux (*thin solid line*), gravitational flux (*dotted*), conduction flux (*short-dash*), radiative flux (*long-dash*), enthalpy flux (*dot-dash*) and wave flux (*triple-dot-dash*) all contribute toward the total energy flux (*thick solid line*).

energy flux that increases the enthalpy flux within the modelled loop and not an effect loop heating due to kinetic energy transfer. Patsourakos *et al.* (2004) carries out energy flux analysis on a long loop model with a local temperature minimum at the loop apex and comes to a similar conclusion. Kinetic energy flux is low whereas gravity and enthalpy dominate. The wave heating profile of this interesting feature is investigated in Section 4.4.

3.8 Radiation Function

As already described, the radiative loss function is a very important factor in coronal loop modelling and measurements of $L_{\rm rad}$ are constantly evolving through improvements of coronal abundance observations. Section 3.7 also indicates radiative losses to be the main energy sink along the highly radiating, dense coronal loops. The parameter study in Chapter 4 uses Rosner *et al.* (1978) classical radiative losses (Eq. 3.5), but it is useful to directly compare the classical radiative loss function with more recent studies. Klimchuk & Cargill (2001) uses modified values of $L_{\rm rad}$ (Eq. 3.6) for their nanoflare heating model, so these two radiative loss functions are compared by modifying the numerical method accordingly. Three loop lengths are selected (L =10Mm, 300Mm and 600Mm) and the characteristics of the turbulent heating is kept at $l_{\rm drive}$ = 100km and ξ = 8kms^{-1}. Figure 3.5 shows the results from this comparison. Generally, short coronal loops (L = 10Mm in this case) experience lower temperatures and lower densities when radiating with $L_{\rm rad}$(KC), there appears to be a decrease in temperature of approximately 0.1MK and a decrease in density of approximately 8×10^{8}cm^{-3}. The situation changes for higher temperatures. $L_{\rm rad}$(RTV) causes the lower temperature solutions in both the L = 300Mm and 600Mm loops, but maintains higher densities than the $L_{\rm rad}$(KC) solutions. This comparison is interesting as there is a comparable difference in results and the dominance of one radiation function over another is dependent on

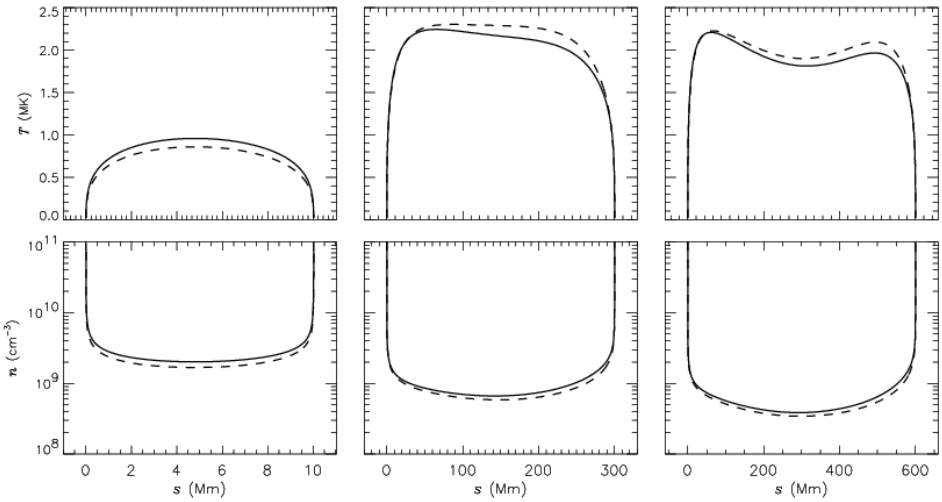

Figure 3.5: Comparison between two radiative loss functions for a selection of loop lengths. Loops radiating with $L_{\rm rad}$ by Rosner *et al.* (1978) (Eq. 3.5) are plotted with a *solid* line and loops radiating with $L_{\rm rad}$ by Klimchuk & Cargill (2001) (Eq. 3.6) are plotted with a *dashed* line. Both proton temperature (T_p, top) and density (n, bottom) are plotted for each loop. The three example loops (L =10Mm, 300Mm, 600Mm) are all heated by $\xi = 8{\rm kms}^{-1}$, $l_{\rm drive} = 100$km waves.

plasma temperature.

During preliminary tests of the numerical method, it was found that the stability of the model worsened as the iterative procedure (Section 3.3) approached high-$l_{\rm drive}$ values. It can be expected that the method will not simulate hydrostatic loops. As the code reaches $l_{\rm max}$ the loops will approach a quasi-hydrostatic state ($\partial v/\partial s \sim 0$, Eq. 3.2) but there is also the concern that there is insufficient heating near the loop footpoints to balance the radiative losses. The radiative loss function used by Moriyasu *et al.* (2004) (Eq. 3.7, $L_{\rm rad}$(MTTK)) addresses this issue. Rather than setting the radiative response for certain plasma temperatures, $L_{\rm rad}$(MTTK) varies with the density of the emitting plasma at temperatures below 0.04MK. Although there was some success with the implementation of $L_{\rm rad}$(MTTK), the numerical method still becomes unable to arrive at a steady-state due to the quasi-hydrostatic nature of coronal loops driven at maximum driving scales ($l_{\rm drive}$).

3.9 Discussion

This chapter details the numerical method applied to the coronal loops modelled in this study. The reader is guided through the main mathematical steps during manipulation and application of the compact form of the basic equations (Section 3.2.1 and 3.2.2). Each element in the numerical method can then be cast into a matrix where the derivatives can be managed and evaluated. Only when the basic equations have undergone this rigorous manipulation can the full-implicit scheme be applied (Section 3.2.4). Due to constraints on this method it can often be difficult to arrive at a desired final solution from scratch, so the iterative method as explained in Section 3.3 must be used to gradually adapt the independent variables toward a final (and steady) solution. It is found that this approach is very effective, and although time consuming, one can probe the limits of numerical stability with great accuracy. From manipulation of the full-implicit scheme described here, rigorous testing and development is required to adapt this model for simulating coronal loops of various lengths and turbulence criteria. Some of the initial results arriving from this study are also presented during tests of numerical stability and energy conservation (Section 3.7). A good foundation is acquired so a thorough parameter study can be carried out to see the ability of the model to simulate coronal loops that may explain the characteristics of observed quantities (Chapter 4).

Chapter 4

Coronal Loop Parameter Mapping

4.1 Introduction

After development and testing, the next task for this study is to explore the advantages and limitations of the numerical method outlined in Chapter 3. The resonant Alfvén waves are maintained by a turbulent cascade as described in Section 2.3. The parameters of Alfvén wave amplitude (ξ) and driving scale (l_{drive}) characterise the dynamics of the quiescent coronal loops under study. There is a massive parameter space to explore (especially when considering the range of loop lengths that are available) so a method is required to quantify the response of the basic parameters (temperature, T, density, n, velocity, v, and pressure, p) to ξ and l_{drive} variation. It is assumed that the turbulence will develop by the Kolmogorov regime as the typical scales in question are well within the resolution limits of current observatories, but very small scales (down to $l_{\mathrm{drive}} \sim 10$km) will also be probed so a full picture of the system can be evaluated. Section 4.3 justifies this choice.

This chapter is devoted to an extensive parameter study where the effect of the variables ξ, l_{drive} and loop length (L) on coronal loop plasma are analysed in a series of contour

plots. These plots provide an ideal visual basis to develop subsequent loop case studies and analysis giving a better understanding of any patterns and/or relationships between the independent variables. Section 4.4 examines the heating profiles generated by this method for a range of loops also detailing the dependence of the evolving ξ on loop temperature and loop length. This chapter concludes with a comprehensive comparison with the classical hydrostatic scaling relation derived by Rosner *et al.* (1978) in Section 4.5.

4.2 Parameter Mapping

It is important that an overview is acquired of the response of this range of loop lengths for different Alfvén wave amplitudes (ξ) and driving scales (l_{drive}). This numerical method does not allow us to select a desired output temperature and/or density due to the self-consistent nature of the physics used. The governing turbulence equation (Eq. 2.3) characterises the loop output parameters, not vice-versa. A problem presents itself. To arrive at any steady-state solution, values for ξ and l_{drive} must be decided on and then the simulation started (assuming, firstly, that the variables are not too extreme for the input solution to converge to). This is a major limitation, one cannot simply see how an arbitrary value of ξ and an arbitrary value of l_{drive} produces a reasonable output solution. The iterative method described in Section 3.3 is a very effective way to slowly adapt a solution toward the desired output parameters, but this can be an arduous cycle of running the simulation, slightly altering the variables, running the simulation, slightly altering the variables and so on. Producing the desired output temperatures and/or loop densities can be difficult and highly improbable (over a small number of iterations in any case), one is effectively taking 'shots in the dark' and guessing at the parameters that are outputted. So, the maximum temperature (T_{max}), minimum density (n_{min}), maximum velocity (v_{max}) and minimum pressure (p_{min}) must be plotted for many

steady solutions (storing the output data over each iteration) to the ξ and $l_{\rm drive}$ independent variables in parameter space. A visual 'map' of the expected final solutions can be acquired.

The results presented in this chapter are wide ranging and will take on 3 sections. The response of a number of different coronal loop lengths (from 'short' $L = 10$Mm to 'long' $L = 600$Mm) to the variables ξ and $l_{\rm drive}$ are evaluated whilst assuming a Kolmogorov turbulent spectrum. The first section demonstrates the sensitivity of loop length to a range of driving scales ($l_{\rm drive} = 10 - 8000$km) whilst being held at a constant Alfvén wave amplitude ($\xi = 10$kms^{-1}; corresponding to a footpoint temperature of 20,000K; Chae *et al.* 1998). The second section again plots L against $l_{\rm drive}$, but the Alfvén amplitude is increased to $\xi = 14$kms^{-1} (corresponding to a footpoint temperature of approximately 30,000K). The results of $\xi = 10$kms^{-1} can be compared with $\xi = 14$kms^{-1}. In the third section, one loop length ($L = 40$Mm) is studied to find the parameter response to both ξ and $l_{\rm drive}$ variables. By 'mapping' $T_{\rm max}$, $n_{\rm min}$, $v_{\rm max}$ and $p_{\rm min}$, comparisons can be made with the results of other authors (i.e. Winebarger *et al.* 2003 ran tests on a $L = 40$Mm loop and compared their dynamic model results with observation).

Warm ($T_{\rm max} \approx 1$MK) and dense ($n_{\rm min} > 10^9$cm^{-3}) short, EUV loops ($L < 100$Mm) are readily simulated. Hot ($T_{\rm max} > 2$MK) and less dense ($n_{\rm min} \approx 10^9$cm^{-3}) long, SXT loops ($L > 200$Mm) are also evident. Through mapping the coronal loop parameters, an insight to the reaction of loops of a range of lengths to the turbulent heating variables can be gained.

Figure 4.1 shows the response of loop lengths $L = 10 - 600$Mm to driving scales $l_{\rm drive} = 10 - 8000$km. In this case, all solutions are held at constant $\xi = 10$kms^{-1}. There are 277 steady solutions that form this analysis. The area with no data in the top left hand corner of each plot are hydrostatic solutions and could not be computed with this code. The area with no data in the bottom right hand corner are unstable solutions due

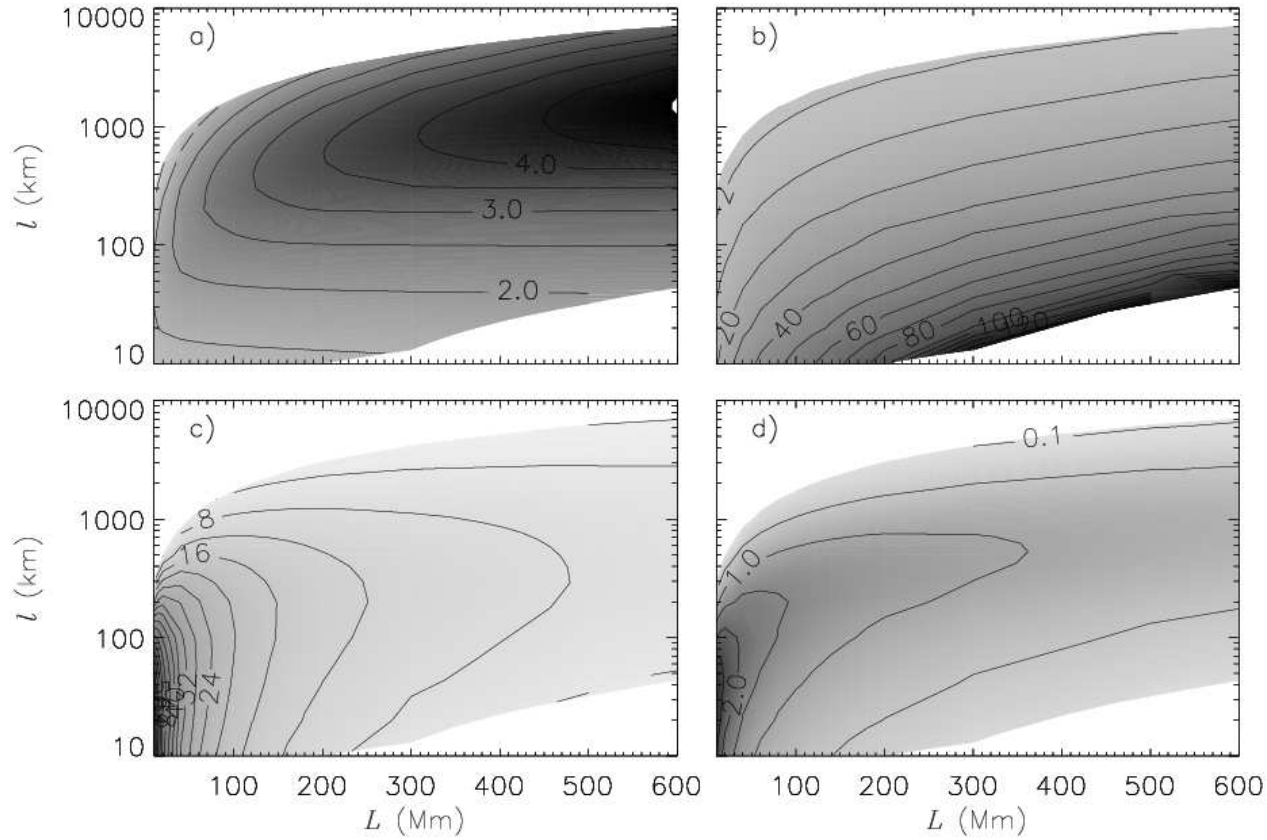

Figure 4.1: Contour plot of the ξ=10kms^{-1} dataset. a) Maximum proton temperature (MK), b) maximum proton velocity (kms^{-1}), c) minimum proton density ($\times 10^8$cm^{-3}), d) minimum pressure (dyne cm^{-2}). Note: l in the above plot is equivalent to $l_{\rm drive}$ in Eq. 2.15. This is the case for all subsequent parameter plots in this chapter.

to extreme plasma flow (Fig. 4.2). Short (long) loops with very high (low) $l_{\rm drive}$ causes the code to break down. Short loops with very high $l_{\rm drive}$ lead to insufficient heating near the boundaries to balance the radiative loss (radiative energy loss far exceeds wave energy gain). There is some improvement on results when the radiative loss function as adopted by Moriyasu *et al.* (2004) (Section 3.8) is incorporated in the footpoint region of the loops, but problems persist as maximum-$l_{\rm drive}$ is approached. This issue is therefore a problem with the code not finding steady state for hydrostatic solutions. At low-$l_{\rm drive}$ and long loop lengths ($L \geq 300$Mm) however the opposite action occurs. Plasma flow becomes shocked ($v \sim c_{\rm s}$), causing instabilities and loss of steady-state. Some shocked solutions can be modelled after further refinement of the code (Section 5.7).

In Fig. 4.1, $T_{\rm max}$, $v_{\rm max}$, $n_{\rm min}$ and $p_{\rm min}$ are plotted in frames *a*), *b*), *c*) and *d*) respectively. It is worth noting that these maximum and minimum values are not necessarily at the loop apex. Loops with extreme asymmetry in their heating profiles will cause a heating maximum closer to the loop footpoint. This is not obvious in this figure, but with reference to Fig. 4.2, generalised regions of heating profiles are plotted. Figure 4.2 is assembled by scanning through the loop temperature and heating profiles. Temperature inversion, footpoint, non-uniform and quasi-uniform heating profiles are identified according to the profiles evident in the $\xi = 10{\rm kms}^{-1}$ data. This is produced 'by eye' and is only intended to illustrate the general regions of heating profile. The criteria for identifying different heating profiles can be found in Section 4.4.

This model predicts generally high plasma temperatures for the whole range of coronal loops, with a maximum value of 5MK located at $l_{\rm drive} = 1000$km for the longest loop, $L = 600$Mm. The coolest solution is located at $l_{\rm drive} = 280$km for a short loop of length $L = 10$Mm, where the maximum (apex) temperature does not exceed $T = 0.75$MK. This cool loop solution is investigated in Section 5.5.

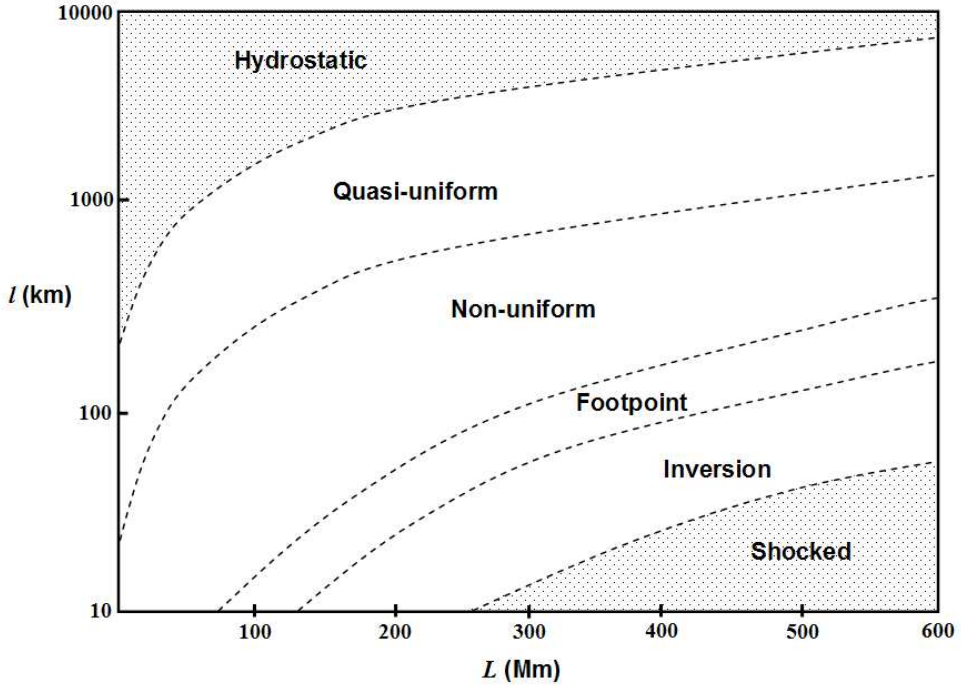

Figure 4.2: The generalised regions of modelled loop heating. The shaded zones indicate where the numerical method has difficulty producing steady-state solutions and could not be plotted. A similar pattern in heating profiles is observed across all values of ξ.

As investigated by Neupert *et al.* (1998), Lenz *et al.* (1999), Aschwanden *et al.* (2000a), Aschwanden (2001), the driving scale has a strong influence on the mass of plasma flow into the coronal loop. Winebarger *et al.* (2003) use the variable 'scale height' ($s_{\rm H}$), which is analogous to $l_{\rm drive}$ as described in Eq. 2.3. Winebarger *et al.* (2003) state a small $s_{\rm H}$, has the ability to pull more mass from the chromosphere. This process is reflected in work by Antiochos & Klimchuk (1991), where it is found that an increase in heating (i.e. reducing the driving scale) focuses the energy deposition above the upflowing footpoint, pulling more plasma into the loop. However, Fig. 4.1c shows that this dependence is not monotonous. For a loop of fixed length, there is a particular value of $l_{\rm drive}$ which optimises plasma density around the loop apex. For short loops at low $l_{\rm drive}$, there is a huge amplification in the apex density, $n_{\rm apex}$ ($n_{\rm apex} \approx n_{\rm min}$ in this case). As L is increased, $n_{\rm apex}$ diminishes very quickly. The density for the shortest

(L = 10Mm) loop approaches $n_{apex} = 8{\times}10^9 cm^{-3}$ at low l_{drive}. However, for the longest loop the density drops to around $n_{apex} = 4{\times}10^8 cm^{-3}$ at low l_{drive}.

At maximum-$l_{drive(max)}$ for the whole range of loops the wave energy seems to be too weak to drive the plasma around the loop, n_{min} is reduced to a minimum as the plasma flow is close to zero. Maximum-l_{drive} appears to be highly dependent on L. From this analysis, the contrast between short, cool loops and long, hot loops can be seen. This predicts cool and very dense loops for $L < 60$Mm at $l_{drive} < 100$km. Also, very hot, less dense loops exist at $L > 200$Mm, with 'optimised heating' at approximately $l_{drive} = 1000$km.

Figure 4.3 shows the results for $\xi = 14 kms^{-1}$. A similar pattern as $\xi = 10 kms^{-1}$ exists, but more energy is injected into the corona. This effect is demonstrated in the temperature profile (Fig. 4.3a). The maximum temperature for this range of L has now increased to 6.5MK, for $L = 600$Mm at $l_{drive} = 4000$km.

This analysis is composed of 285 steady solutions. A greater range of solutions exist; maximum-l_{drive} is increased by an average of 62%. The coronal loops are able to support higher driving scales. If ξ is increased, the energy carried by the wave is increased. This explains why there is such an increase in $l_{drive(max)}$ as ξ is raised from $\xi = 10 kms^{-1}$ to $\xi = 14 kms^{-1}$.

Although this is the case, for solutions $L < 40$Mm at $\xi = 14 kms^{-1}$, the code breaks down. As L and l_{drive} are small, a massive amount of plasma is dragged from the chromosphere to produce very dense coronal loops (Fig. 4.3c). Although compared to the other solutions in this analysis they appear 'cool', these short loops have temperatures in the region of $T < 2$MK (this is an approximation as loops below $L = 40$Mm have been ommitted from this plot). If the loop temperature is lowered too far, the solution becomes unstable. Cool loops are a direct result of lower ξ. The maximum density pulled from the chromosphere by Alfvén waves at $\xi = 14 kms^{-1}$ is $n_{min} = 6.0{\times}10^9 cm^{-3}$.

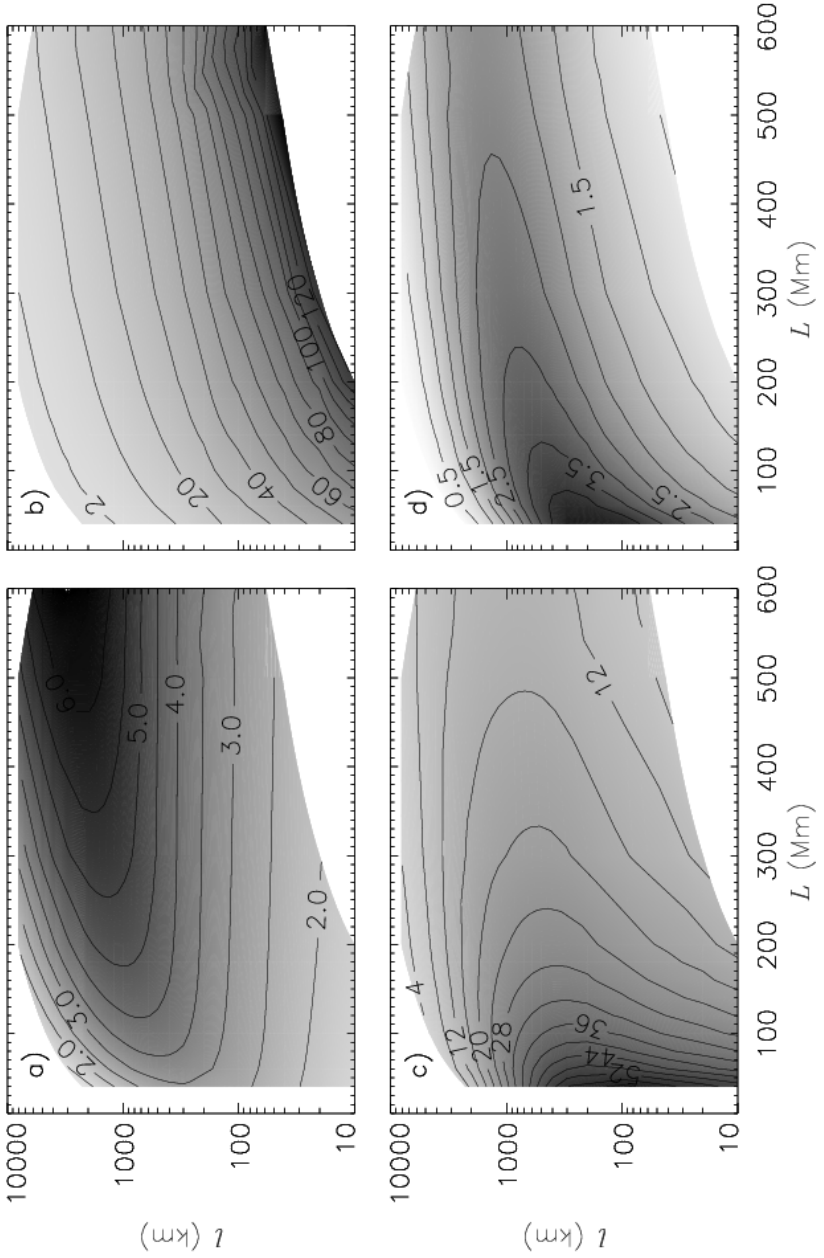

Figure 4.3: Contour plot of the ξ=14kms^{-1} dataset. a) Maximum proton temperature (MK), b) maximum proton velocity (kms^{-1}), c) minimum proton density ($\times 10^8$cm^{-3}), d) minimum pressure (dyne cm^{-2}).

As detailed in Chapter 1 (Section 1.5), plasma flow velocities along observed steady state coronal loops are believed to be in the range of $5-60\text{kms}^{-1}$ (Saba & Strong, 1991, Spadaro *et al.*, 2000, Winebarger *et al.*, 2002). In this model, if the driving scale is low, higher plasma flow velocities can be expected. With reference to Fig. 4.1b and 4.3b, velocities are enhanced at minimum-l_{drive} to $v_{\text{max}} = 150\text{kms}^{-1}$. The solutions appear to have a very sharp cut-off at low l_{drive} where the code breaks down due to the production of shocked plasma flow. The solutions over $L = 200\text{Mm}$ demonstrate higher v_{max} for higher l_{drive}, but the maximum velocity remains below 170kms^{-1} ($v \leq c_{\text{s}}$).

To further this method, a loop of length $L = 40\text{Mm}$ is analysed (Fig. 4.4). Again, T_{max}, v_{max}, n_{min} and p_{min} are plotted in frames *a*), *b*), *c*) and *d*) respectively. ξ and l_{drive} are varied so a picture is built as to how a loop of this length responds. 142 steady solutions form this analysis. $\xi = 5 - 12\text{kms}^{-1}$ and $l_{\text{drive}} = 10 - 1000\text{km}$ are chosen as the variable range. The range of ξ corresponds to chromospheric temperatures of $T = 15000 - 22000\text{K}$ (Chae *et al.*, 1998).

As one would expect, the maximum temperature can be found at maximum ξ (12kms^{-1}). There is a region of optimised heating at approximately $l_{\text{drive}} = 200\text{km}$, lower l_{drive} tends to cooler solutions. This pattern can be seen for all L, optimised heating occurs at mid-l_{drive} for each solution, before the code runs into the hydrostatic region (in the top left-hand corner). As observed in Fig. 4.4a and 4.4c, a high temperature ($T_{\text{max}} = 2.5\text{MK}$) region coincides with a high density ($n = 4.5\times10^{9}\text{cm}^{-3}$) region. This confirms as ξ is increased, greater energy is injected into the coronal plasma, causing greater heating and more mass to be driven from the chromosphere. As T and n are in correlation for this test, the total plasma pressure ($p = nkT$) is greatly enhanced at high ξ (Fig. 4.4d). As can be expected, plasma velocity is high at low l_{drive} (Fig. 4.4b), reaching a maximum of $v_{\text{max}} = 42\text{kms}^{-1}$ at $l_{\text{drive}} = 10\text{km}$ and $\xi = 12\text{kms}^{-1}$.

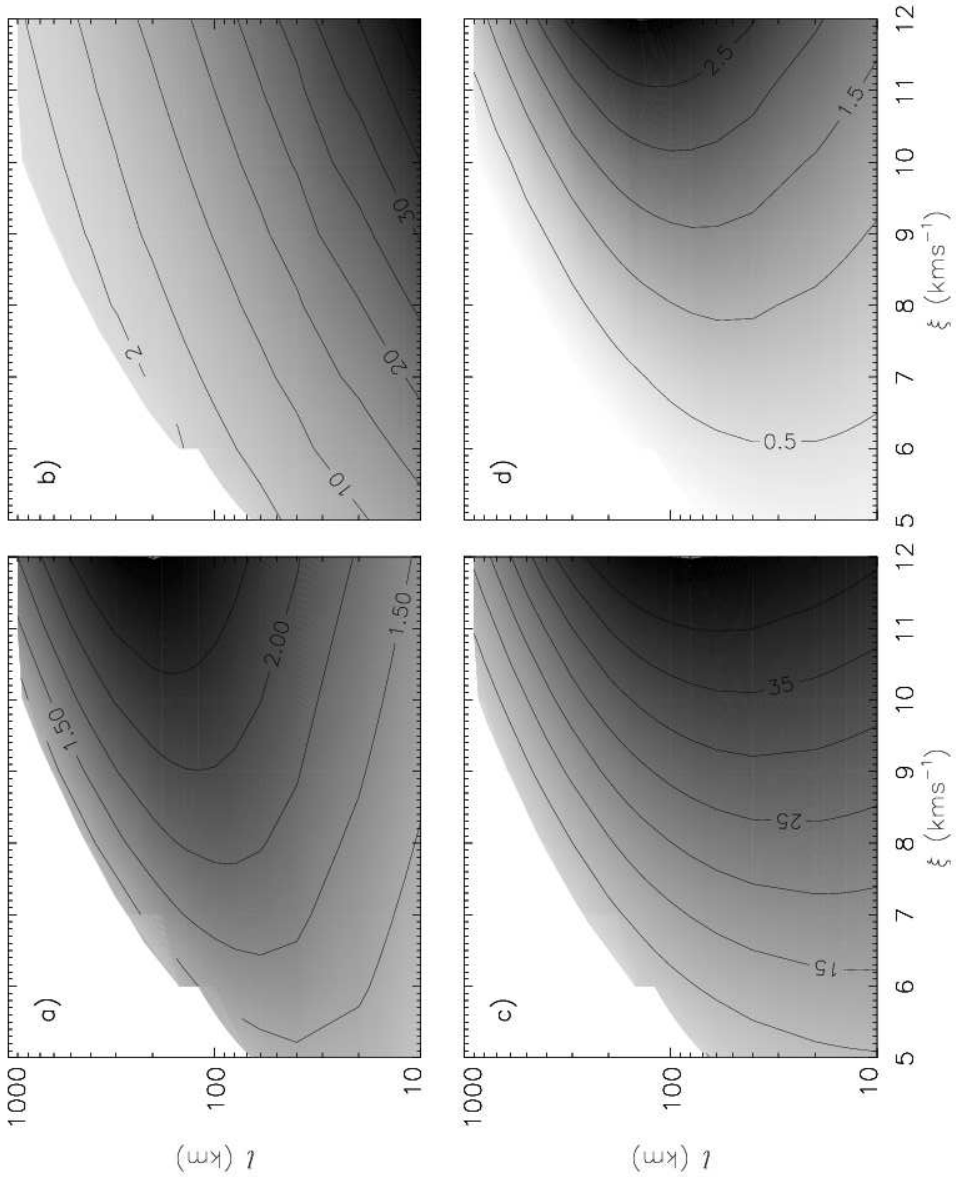

Figure 4.4: Contour plot of the L=10kms^{-1} dataset. a) Maximum proton temperature (MK), b) maximum proton velocity (kms^{-1}), c) minimum proton density ($\times 10^8$cm^{-3}), d) minimum pressure (dyne cm^{-2}).

4.3 Kolmogorov vs. Kraichnan II

Section 2.3.1 explored the current understanding of Kolmogorov and Kraichnan turbulence (Kolmogorov, 1941, Kraichnan, 1965) and suggests that Kraichnan turbulence operates over scales that may be associated with sub-resolution structures. To focus this work, Kolmogorov scales are assumed to dominate the modelled coronal loops in this study and applied to the parameter study in Section 4.2. This section will detail the reaction of the modelled loops to the Kraichnan turbulent regime and justify why Kolmogorov turbulence is assumed in Section 4.2.

The Kraichnan turbulent cascade equation ($Q = \rho\xi^4/v_A l_{\rm drive}$) is applied to an isothermal loop solution for the $L = 300$Mm loop (see Chapter 5, Table 5.1). A comparison can then be made between the loop heated in the Kraichnan regime and the loop heated by the Kolmogorov regime to verify the difference in driving scales required to maintain the heating of a steady state loop at isothermal temperatures. The motivation behind using one of the isothermal loops from Section 5.3 is that there needs to be a very delicate balance of $l_{\rm drive}$ and ξ to acquire an isothermal coronal temperature. For a given magnetic field strength there appears to be a unique temperature where the balance between wave energy flux and gravitational energy flux forms the isothermal state. By applying Kraichnan heating to one solution and gradually adapting the input variables to match the isothermal temperature with the Kolmogorov solution, a comparison between plasma parameters can be made whilst being certain similar heating is being applied.

Figure 4.5 shows a direct comparison of loop temperature, heating rate, density and velocity (from top to bottom) for the $L = 300$Mm loop solution. The left column shows the loop heated by the Kolmogorov regime, the right column shows the loop heated by the Kraichnan regime. There is very little difference in parameter values once the isothermal temperatures are matched at approximately 1.6MK. The Kolmogorov loop

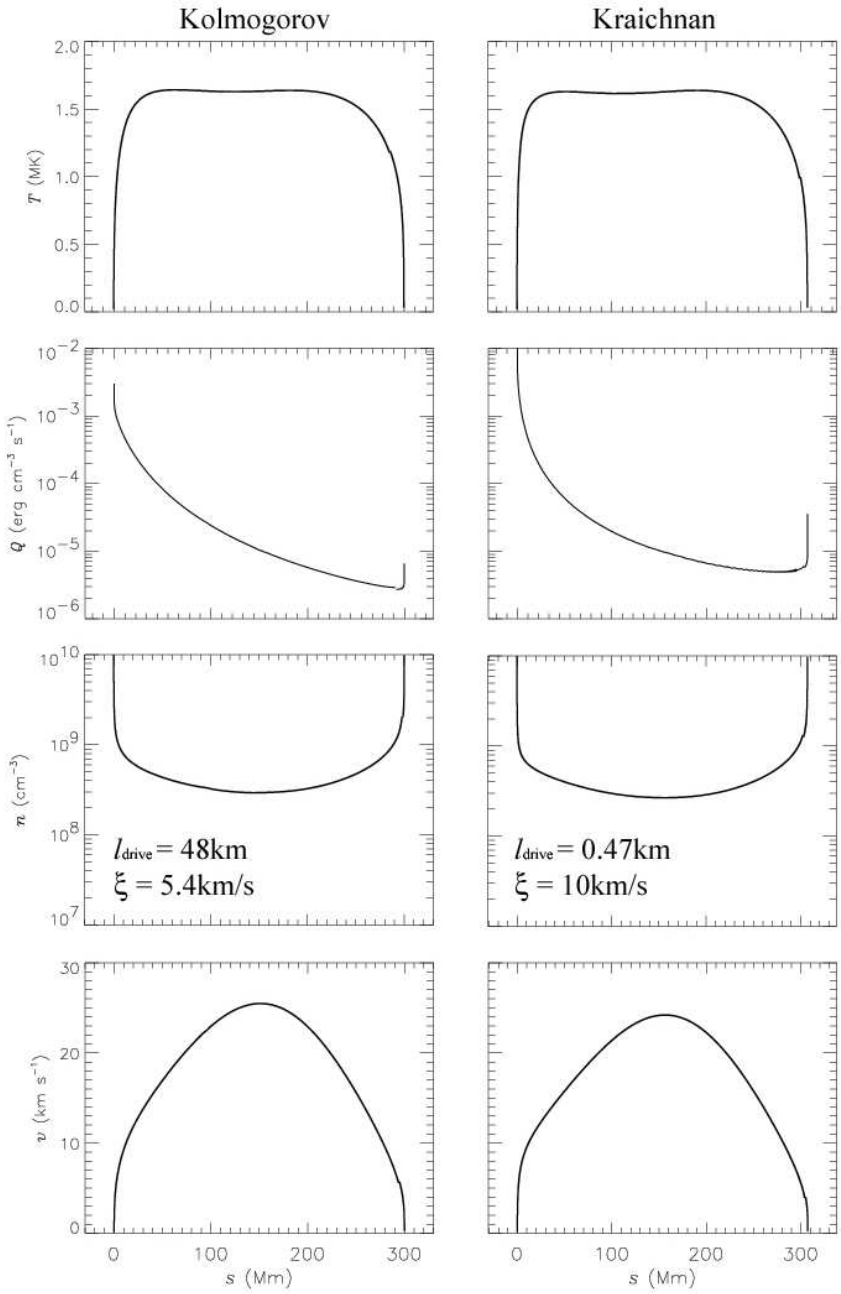

Figure 4.5: A direct comparison of a 300Mm loop heated with Kolmogorov turbulence (*left column*) and Kraichnan turbulence (*right column*). Proton temperature, heating rate, density and flow velocity are plotted from top to bottom.

is held at $l_{\rm drive}$ = 48km, ξ = 5.4kms^{-1} and B_0 = 80G. The Kraichnan loop is held at $l_{\rm drive}$ = 0.47km, ξ = 10kms^{-1} and B_0 = 34.5G. No other isothermal temperatures seem possible apart from the solution with these characteristics. Note the Kraichnan loop can only be maintained in an isothermal state if the magnetic field strength is decreased to approximately half that of the Kolmogorov solution. At higher B_0, hotter isothermal solutions result. On comparison of $l_{\rm drive}$ for both cases, it becomes clear that the prediction in Section 2.3.1 is accurate. Due to the $v_{\rm A}$ term in the denominator of Eq. 2.16, $l_{\rm drive}$ must be decreased by two orders of magnitude (in Fig. 4.5 from 48km down to 0.47km). It would appear that Kraichnan turbulence requires higher energy waves of higher ξ to support equivalent heating as Kolmogorov turbulence.

Loops of various temperatures and lengths are put through the same comparison and the results are similar. For Kraichnan loops, $l_{\rm drive}$ is two orders of magnitude lower than Kolmogorov loops, magnetic field strength must be lower to attain similar heating, and ξ must be increased to support the low driving scales. This study suggests waves cascaded under the Kraichnan regime are less efficient at heating the coronal plasma than the Kolmogorov regime (higher ξ is required for the low $l_{\rm drive}$). Figure 4.5 demonstrates a steeper temperature gradient above the upflowing footpoint for the Kraichnan solution however. Also, with reference to the heating rate along the loop, the profile appears to be far more exponential than the Kolmogorov profile. Both these features may be symptomatic of the small scales wave energy is dissipated over.

Generally, Kraichnan heating does not return favorable results as the scale lengths are very small. In addition, Cho *et al.* (2003) confirm that Kolmogorov turbulence is a good approximation of coronal turbulence as numerical experiments are consistent with the $k^{-5/3}$ spectra. As the corona is highly magnetic one would expect MHD (Kraichnan) turbulence evolving in the plasma, magnetic field interfering with turbulent eddy motions, but this does not appear to be a factor. Therefore Kolmogorov turbulence (a

non-magnetised description) is assumed to be a very good approximation for the incompressible plasma in this study even whilst assuming the turbulence is Alfvénic in character.

4.4 Heating Profiles

The temperature profiles relating to each of the heating rates noted in Fig. 4.2 will now be presented from solutions for the 600Mm loop and plotted. The solutions in this comparison are heated by $\xi = 14\text{kms}^{-1}$ waves and have been extracted from the data in Fig. 4.3. The longest loop and highly energetic waves are used so modelled features will be highlighted. Figure 4.6 shows 5 solutions as the driving scale is increased through $l_{\text{drive}} = 60 - 8000\text{km}$. Each of the heating profile regions are captured in this plot.

Starting with a driving scale of $l_{\text{drive}} = 60\text{km}$, the obvious local temperature minimum is present in the temperature profile (Section 3.7). This is labelled 'temperature inversion' in Fig. 4.2. From the upflowing footpoint to the loop apex, the temperature drops over 1MK from $T_{\text{max}} = 2.5\text{MK}$ to $T_{\text{apex}} = 1.4\text{MK}$. From the loop apex, there is a slow increase in temperature to $T = 1.75\text{MK}$ above the downflowing footpoint. The heating rate is extremely exponential indicating localised heating above the upflowing footpoint. Due to high flow velocities it would be easy to mistake the second heating enhancement (above the downflowing footpoint) as kinetic energy transfer. Section 3.7 disputes this in favour of a dominating gravitational energy flux causing an increase in enthalpy energy flux. As l_{drive} is decreased further, shocks may develop as plasma flow becomes supersonic (Section 5.7).

As the driving scale is increased to $l_{\text{drive}} = 200\text{km}$, the temperature maximum is again above the upflowing footpoint ($T_{\text{max}} = 3.4\text{MK}$), but the 'dip' in the temperature profile has decreased significantly. This profile is labelled 'footpoint heating' in Fig. 4.2. This

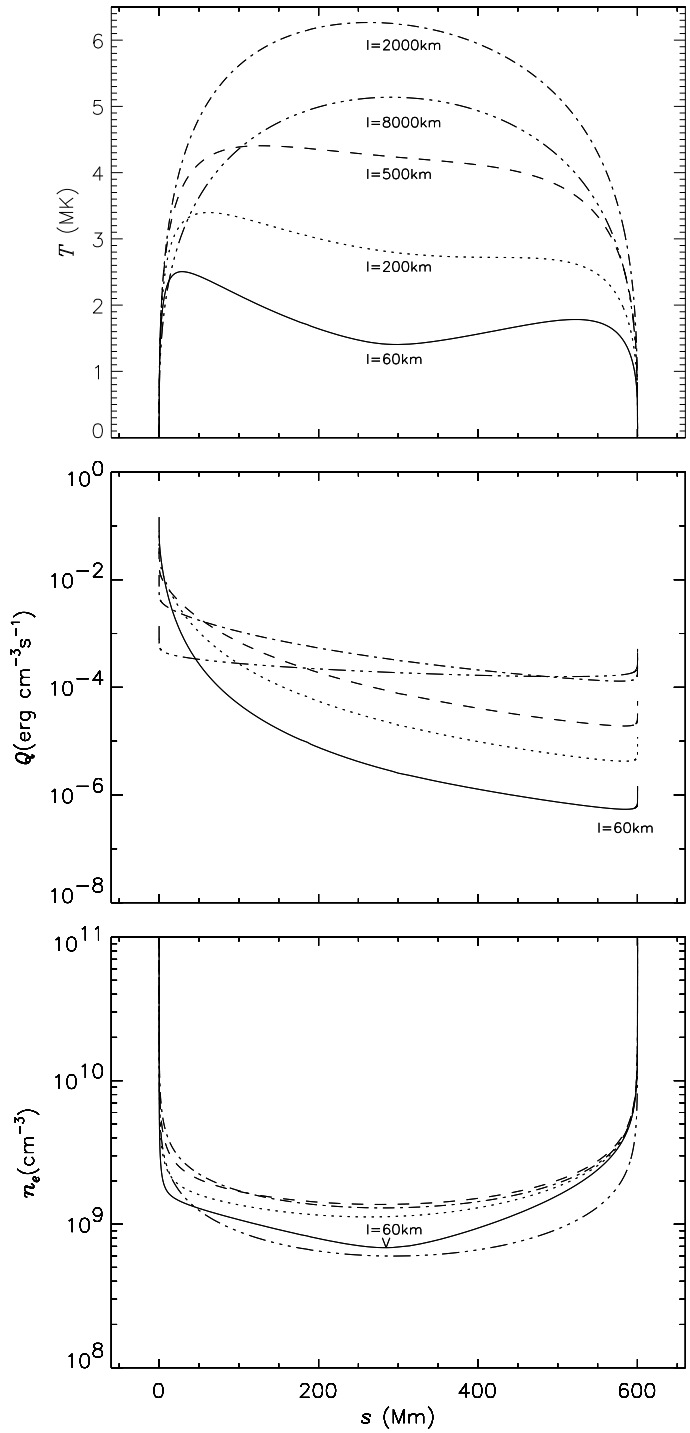

Figure 4.6: Proton temperature profile (*top panel*), heating rate (*middle panel*) and density profile (*bottom panel*) of a L=600Mm loop progressing through the driving scales of $l_{\rm drive}$=60 (*solid line*), 200 (*dotted line*), 500 (*dashed line*), 2000 (*dot-dashed line*) and 8000 km (*triple-dot-dashed line*). ξ = 14kms^{-1} for all solutions. Each line represents the heating profiles of *temperature inversion*, *footpoint*, *non-uniform*, *optimised heating* and *quasi-uniform* respectively.

is a profile where it is obvious there is an enhancement in heating above the upflowing footpoint. Wave energy can propagate further before being totally dissipated. At $l_{\rm drive}$ = 500km, wave energy is able to propagate further. In this case, there is a steady loss in wave energy from the upflowing to the downflowing footpoint. The maximum temperature has again increased to T = 4.5MK above the upflowing footpoint, but the temperature profile is becoming more symmetric. This profile exhibits a 'non-uniform heating' profile. After some experimentation, it was found that by decreasing the energy flux into the loop (ξ), that isothermal solutions are possible. A case-study is outlined in Section 5.3 where the relationship between non-uniform heating and isothermal loops is clarified. As the driving scale is increased to $l_{\rm drive}$ = 2000km, optimised heating for the whole loop length is acquired ($T_{\rm max}$ = 6.3MK). The contours in Fig. 4.1a and 4.3a show these regions of optimised heating for each loop length. Generally they occur at larger $l_{\rm drive}$, before quasi-hydrostatic solutions. Higher driving scales ($l_{\rm drive}$ = 8000km) lead to quasi-hydrostatic solutions as the maximum temperature settles at T = 5.2MK. The heating rate becomes symmetrical at these large driving scales, therefore driving minimum plasma around the loop, reducing flow and heating.

Figure 4.7 extends this analysis by plotting the variation in Alfvén wave amplitude with distance along the loop (using the same solutions as Fig. 4.6). The model allows ξ to change (or evolve) as the local density and wave pressure changes (the evolving Alfvén wave amplitude is indicated as $\xi_{\rm ev}$). $\xi_{\rm ev}$ is given by the simple equation $\xi_{\rm ev} = (2p_w/\rho)^{1/2}$ (as noted in Eq. 3.9). As wave pressure (p_w) peaks above the upflowing footpoint, $\xi_{\rm ev}$ reaches a maximum very quickly if the driving scale is small. As $l_{\rm drive}$ is increased, maximum $\xi_{\rm ev}$ is reached further along the loop length. All the heating profiles are present and the decay of $\xi_{\rm ev}$ clearly shows the rate at which energy is transferred from wave to plasma.

As expected, the temperature inversion profile (at $l_{\rm drive}$ = 60km) peaks sharply and ex-

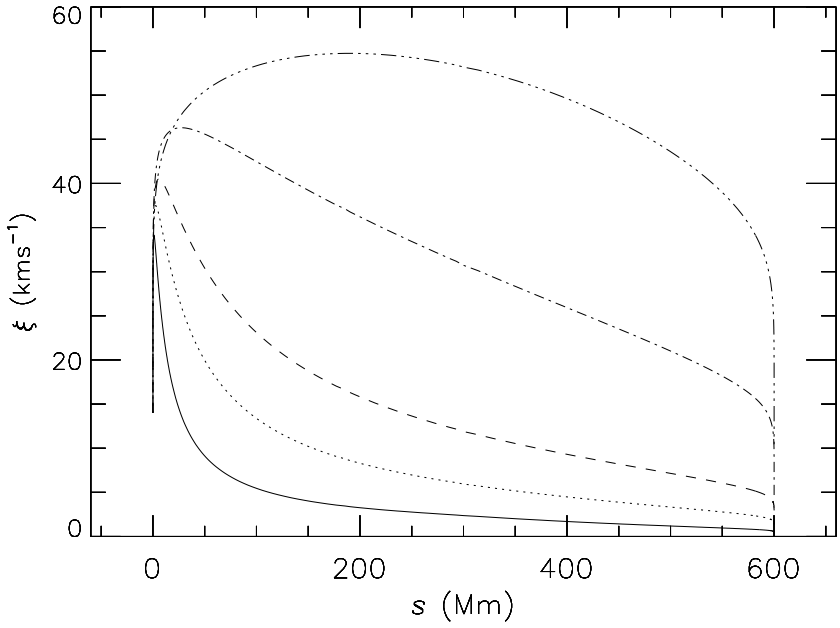

Figure 4.7: The evolution of ξ_{ev} with s along the $L = 600$Mm solution (corresponding to Fig. 4.6), progressing through the driving scales of l_{drive}=60 (*solid line*), 200 (*dotted line*), 500 (*dashed line*), 2000 (*dot-dashed line*) and 8000 km (*triple-dot-dashed line*). ξ begins at 14kms^{-1} for all solutions and allowed to evolve.

ponentially decays with s, energy is transferred very quickly to the footpoint plasma. In contrast, the ξ_{ev} associated with optimised heating ($l_{drive} = 2000$km) demonstrates a linear decay of energy after reaching maximum ξ_{ev}. This is key to understanding the physics behind the region of optimised heating for each loop as it represents *the most efficient way of heating the whole loop length* and not just a focused region. Before the loop reaches optimised heating ($l_{drive} < 2000$km in this case), the heating profiles are predominantly exponential, thus dumping wave energy very quickly. As l_{drive} is increased beyond optimised heating, the heating profile does not heat the loop fast enough. The region of optimised heating is where the decay of ξ_{ev} tends to a linear profile, providing steady and extended heating for the whole loop length.

Figure 4.8 shows the variation of ξ_{ev} with temperature along the loop. Depending on heating profile, the variation of ξ_{ev} will cause unique heating in the loop length. With reference to Fig. 4.8, each profile begins at $\xi = 14$kms^{-1}. As the loops evolve, they

diverge before the plasma is heated to $T = 1$MK. Several conclusions can be drawn from this representation of modelled results. Firstly, where $l_{\rm drive}$ is small (in the case of temperature inversion and footpoint heating), although there may be very intense heating at the upflowing footpoint, heating whole loops by waves of these scales is very inefficient. For the $l_{\rm drive} = 60$km solution, the temperature peaks at 2.5MK, and when compared with the optimised heating 'lobe' (with $T_{\rm max} = 6.5$MK), the difference is dramatic. Some parameters are summarised in Table 4.1 and demonstrate a linear increase in $\xi_{\rm max}$ with temperature. Each heating rate is listed along with $\xi_{\rm max}$, the position of maximum $\xi_{\rm ev}$ along the loop (s) and the temperature at this position ($T_{{\rm max}\xi}$).

So far, only the heating profiles of the $L = 600$Mm loop have been investigated. As already mentioned, each loop length exhibits similar heating profiles, so a comparison of all the results for $L = 600$Mm will be compared with all the results for a short

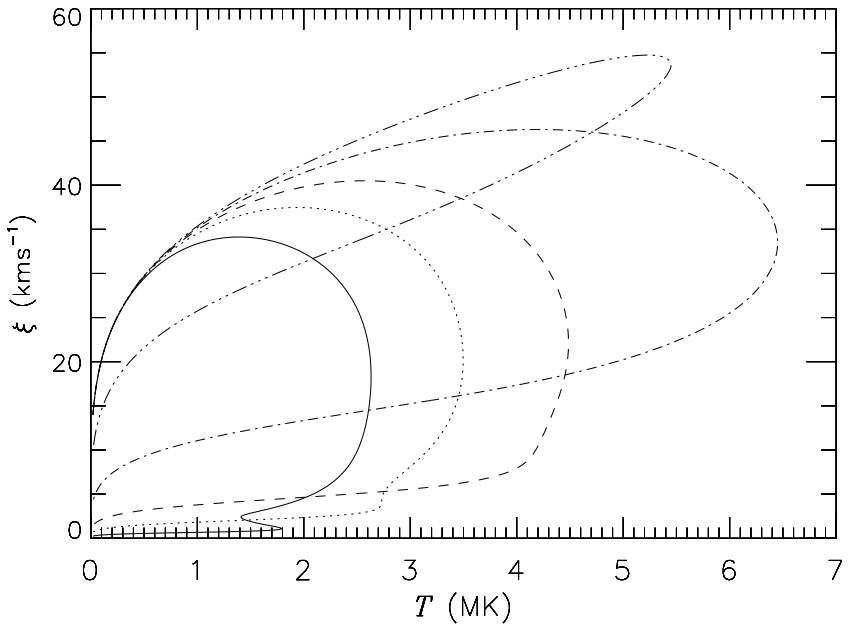

Figure 4.8: The relationship between $\xi_{\rm ev}$ and T as the Alfvén wave evolves along the $L = 600$Mm loop (corresponding with Fig. 4.6). Progression through the driving scales of $l_{\rm drive}$=60 (*solid line*), 200 (*dotted line*), 500 (*dashed line*), 2000 (*dot-dashed line*) and 8000 km (*triple-dot-dashed line*). ξ begins at 14kms^{-1} for all solutions and allowed to evolve.

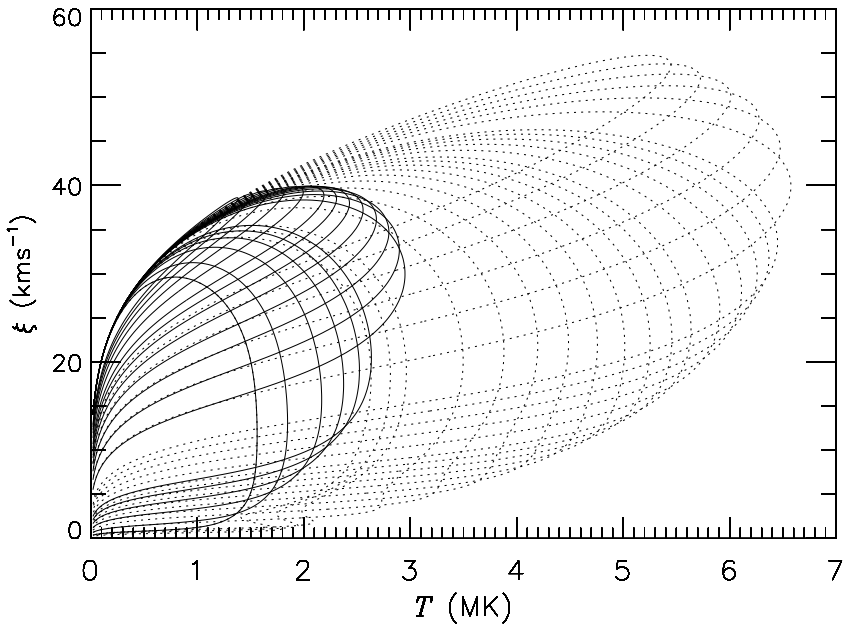

Figure 4.9: The relationship between ξ and T as the Alfvén wave amplitude evolves for all driving scales ($l_{\text{drive (min)}} - l_{\text{drive (max)}}$) for the $L = 600$Mm loop (*dotted lines*) as compared with the short $L = 40$Mm loop (*solid lines*). Solutions for $L = 40$Mm and $L = 600$Mm extracted from Fig. 4.3.

$L = 40$Mm loop. Both loops are heated by $\xi = 14\text{kms}^{-1}$ waves. Figure 4.9 demonstrates both loops stepping through l_{min} (in the case of the $L = 40$Mm loop, $l_{\text{min}} = 10$km; for $L = 600$Mm, $l_{\text{min}} = 60$km) to l_{max} (for $L = 40$Mm, $l_{\text{max}} = 2000$km; for $L = 600$Mm, $l_{\text{max}} = 8000$km). Both loops are overlaid, *solid lines* for $L = 40$Mm solutions and *dotted lines* for $L = 600$Mm solutions. For short loops, the range of temperatures and ξ_{ev} can be expected to be smaller than that of long loops. Similar patterns emerge for both loop lengths, it is the magnitude of ξ_{ev} and T that changes. This confirms that the loop length governs Alfvén wave evolution and maximum temperature.

The above analysis provides a good visualisation of the effects of various wave heating profiles on a selected loop length. Plotting ξ_{ev} along the loop has implications for the theorised source of the very high non-thermal velocities as described in Section 2.4. The extreme values of $\xi = 25 - 70\text{kms}^{-1}$ (Kjeldseth Moe & Nicolas, 1977, Acton *et al.*, 1981) may be very large when compared with the results of Chae *et al.* (1998), but

Table 4.1: Maximum values of Alfvén wave amplitude (ξ_{max}), the position where ξ_{max} occurs (s) and the temperature ($T_{max\xi}$) at ξ_{max} during evolution for each heating profile in Fig. 4.6. Measurements taken from the ξ vs. s and ξ vs. T plots (Fig. 4.7 and 4.8).

	1	2	3	4	5
l_{drive} (km):	60	200	500	2000	8000
ξ_{max} (kms^{-1}):	34.1	37.5	40.5	46.3	54.7
s (Mm):	<10	<10	10	25	200
$T_{max\xi}$ (MK):	1.4	2.0	2.6	4.2	5.3

on analysing the very rapid evolution of ξ in this model (refer to Table 4.1), Alfvén wave amplitudes (a.k.a. non-thermal velocities) of up to 55kms^{-1} can be modelled by allowing ξ to evolve during propagation. ξ_{ev} tends to peak in relatively low regions of the corona if l_{drive} is sufficiently balanced with loop length and ξ. This short investigation supports wave dissipation in the lower corona as this mechanism provides a source of non-thermal velocities within the extremes of observed non-thermal broadening of spectral lines. However, modelled ξ_{ev} does not appear to conform to the ξ vs. T curve in Fig. 2.4 (Chae *et al.*, 2002) as ξ_{ev} appears to increase continuously with temperature and appears to be associated with far higher temperatures.

4.5 Model vs. Classical Theory

As discussed by Winebarger *et al.* (2003), loops with isothermal temperature profiles and loops with temperature maximum at the apex are suspected of being heated by different mechanisms. Section 4.4 finds wave heating to be sufficient to explain many forms of temperature profile simply by assuming a cascade of energy and wave dissipation through resonance with protons. Depending on the turbulent characteristics of the wave (ξ and l_{drive}), almost any variety of dynamic loop is possible. In general, ξ directly influences the energy flux of the injected Alfvén wave and has a dramatic effect on the overall temperature maximum. The dissipation of the wave is governed by l_{drive}

and dictates the scale of the wave and the extent of its dissipation into the plasma. This variable locates the scale of the region where the wave energy is to be dumped into the plasma influencing the amount of plasma driven into the loop. Through the very simple turbulent heating equation, total control on the plasma parameters can be achieved.

Non-uniform heating as observed in the corona (Parker, 1988, Chae *et al.*, 2002) may reveal rapid wave dissipation from the footpoints. If the driving scale is low, the waves will dump energy quickly. This will cause an exponential decay in wave energy as the wave propagates around the loop body. The model described in this thesis simulates a range of non-uniform heating profiles (Section. 4.4). Strong footpoint heating occurs if the driving scale of the turbulent heating is low. This has the effect of drawing more plasma from the chromosphere into the coronal loop. As $l_{\rm drive}$ is increased, it is found (generally) that the non-uniform heating profile shallows out as plasma flow velocity and plasma density decreases. As already mentioned, this method readily produces hot, tenuous loops and short, dense loops. A direct comparison will therefore be made between model solutions and solutions *expected* from classical theory.

Classical theory by Rosner *et al.* (1978) derive a scaling relation in the hope to explain observations by *Skylab* of apparent hydrostatic structures in the lower corona (Section 2.6). Due to the highly dynamic nature of the method as described in this thesis, a scaling relation is difficult to arrive at (due to the large array of free variables and parameters). Attempts have been made to relate turbulence driven dynamic loops with isothermal EUV observations (Section 5.3), but no attempt has been made to assemble a relationship between loop length, temperature or pressure/density. It would therefore be interesting to compare the outputted pressures from this model with *expected* pressures arising from the scaling relation from classical theory (Eq. 4.1).

If a loop has a density higher than the classical model, the loop is known to be *overdense*, if a loop is less dense than expected, the loop is known to be *underdense*. Equa-

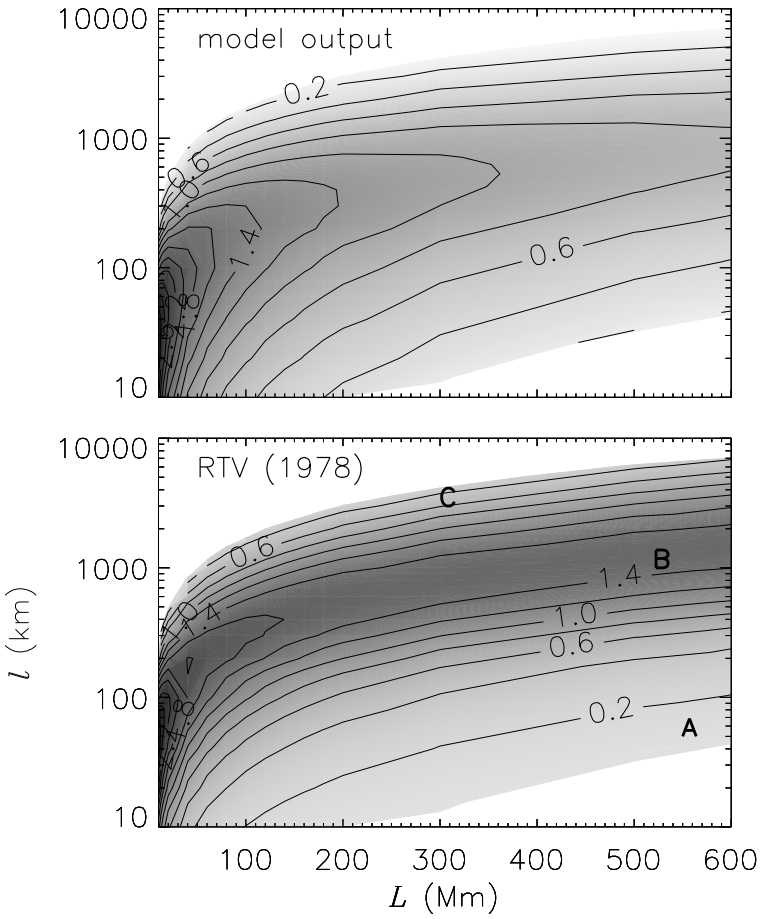

Figure 4.10: A direct comparison between modelled loop minimum pressure (*top-panel*) and derived pressure (*bottom-panel*) from the well known hydrostatic scaling relation by Rosner *et al.* (1978) (Eq. 4.1). Maximum temperatures from the $\xi = 10\text{kms}^{-1}$ modelled loops are used to find the *expected* hydrostatic pressures. The regions labelled 'A','B' and 'C' mark some regions of interest.

tion 4.1 demonstrates the hydrostatic relationship from the observations carried out by *Skylab* and derived by Rosner *et al.*. This relates loop length, pressure and maximum temperature for static loops

$$T_{\max} \approx 1400 \times (pL_{1/2})^{1/3} \tag{4.1}$$

where $T_{\max}$ is the maximum loop temperature, p is the hydrostatic minimum loop pres-

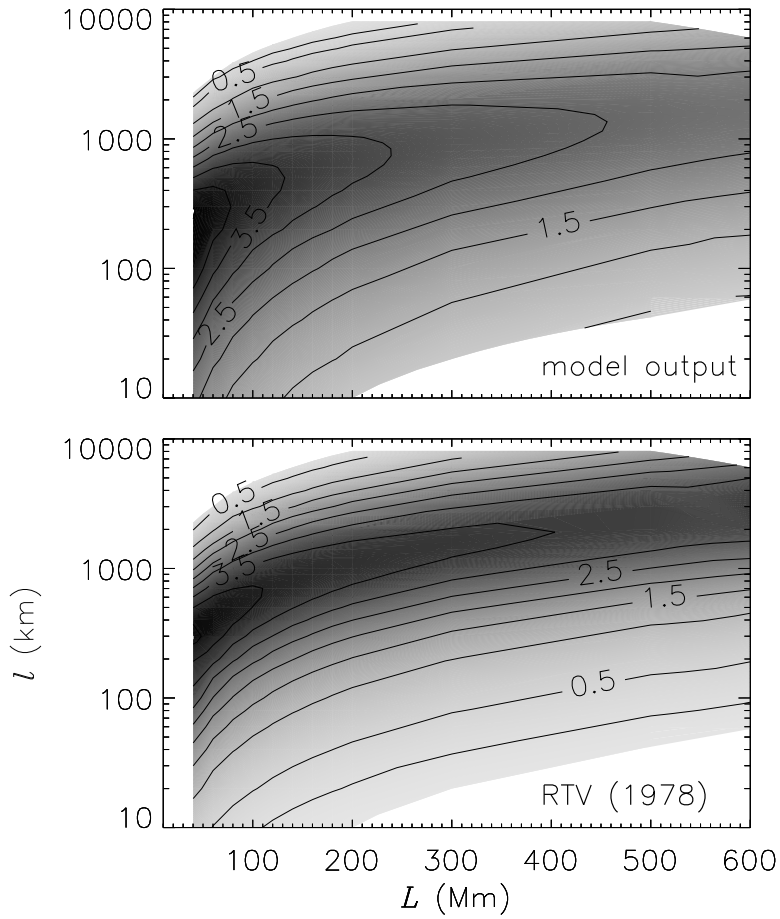

Figure 4.11: As Fig. 4.10, but for loops heated by $\xi = 14 \mathrm{kms}^{-1}$ waves.

sure and $L_{1/2}$ is the loop *half*-length. Pressure is related to density ($p = nk_{\rm B}T$) so modelled pressure is indicative of loop density (Aschwanden, 2004). The pressure of modelled loops using the dynamic method described in this study will be compared with the *expected* loop pressures if the loops were hydrostatic. This is done by outputting temperature results and applying the rearranged equation (from Eq. 4.1)

$$p = \frac{1}{L_{1/2}} \left(\frac{T_{\rm max}}{1400} \right)^3 \tag{4.2}$$

Figure 4.10 demonstrates the comparison of pressure from the loops in this study (top panel) as compared with the result expected if they were hydrostatic (bottom panel). The top panel shows the outputted pressures for loops heated by $\xi = 10 {\rm kms}^{-1}$ waves, the bottom panel shows the expected pressures arising from the relationship in Eq. 4.2. The maximum temperatures and loop (half) lengths are read into the equation and expected pressures are plotted.

High velocity solutions in the low-$l_{\rm drive}$ region (labelled 'A' in Fig. 4.10) return favorable results suggesting higher velocity flows and low driving scales pull more plasma into the corona, creating an overdensity (Winebarger *et al.*, 2002, 2003, Patsourakos *et al.*, 2004). A complication occurs when the classical (hydrostatic) results from the above scaling relation appear to return more dense results for longer loop solutions (labelled 'B'). Generally it is thought hydrodynamic loops will be more dense when compared with hydrostatic loops, this result defies this idea. However, underdense loops may also be modelled by hydrodynamic models when they exibit X-ray loop charateristics. This is confirmed by the simulation where long coronal loops at high driving scales outputted from the model (labelled 'C') appear to be underdense when compared with the classical values. Figure 4.11 compares the model pressures with expected values (in the same manner as Fig. 4.10), but using data from the $\xi = 14 {\rm kms}^{-1}$ study (Fig. 4.3). A very similar pattern exists for both studies, underdense loops in high-$l_{\rm drive}$ regions,

overdense loops in low-$l_{\rm drive}$ regions, again with a discrepancy for long modelled loops.

Obtaining better clarity in results is required. Figures 4.12 and 4.13 arise from subtracting modelled pressures ($p_{\rm model}$) from the expected Rosner *et al.* (1978) hydrostatic pressures ($p_{\rm RTV}$) shown in the comparison plots in Figures 4.10 and 4.11. A very interesting pattern emerges from this analysis. Primarily there appears to be two very distinct regions of overpressure and underpressure (corresponding to overdensity and underdensity). In both Figures 4.12 and 4.13 an overdensity region can be found in the bottom-left hand corner of the plots. This region corresponds to the coolest, short and dense coronal loops in the results of the $\xi = 10{\rm kms}^{-1}$ and $\xi = 14{\rm kms}^{-1}$ analysis (Fig. 4.1 and Fig. 4.3 respectively). A region of underdensity can be found in the top-right hand corner of both plots which corresponds to hot, long and tenuous coronal loops found in the $\xi = 10{\rm kms}^{-1}$ and $\xi = 14{\rm kms}^{-1}$ analysis. Cargill & Klimchuk (2004) support this finding. By comparing loop model densities and pressures with classical theory (Rosner *et al.*, 1978, Craig *et al.*, 1978, Hood & Priest, 1979), Cargill & Klimchuk conclude dynamic loop models produce overdense, cool loops and underdense, hot loops. The results from the analysis summerised in Fig. 4.12 and Fig. 4.13 add an extra parame-

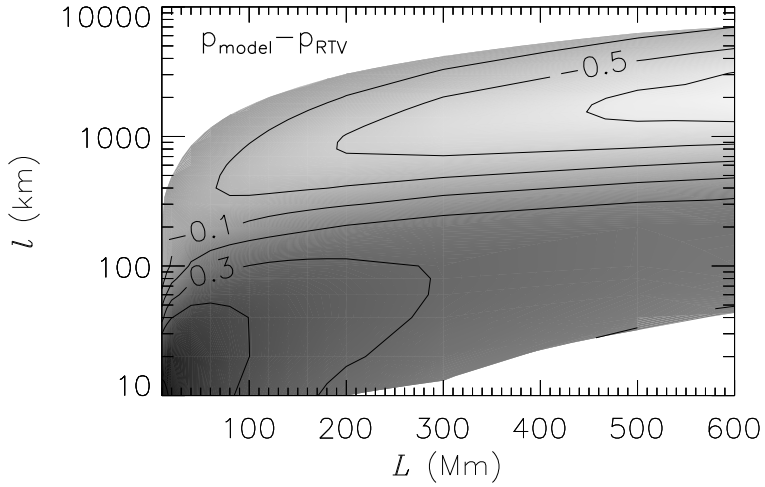

Figure 4.12: From Fig. 4.10, $p_{\rm model} - p_{\rm RTV}$ is plotted. For the $\xi = 10{\rm kms}^{-1}$ dataset, differences in pressure between loops range from $\Delta p \sim -0.8$ dyne cm^{-2} (underdensity) in the top-right sector to $\Delta p \sim 1.1$ dyne cm^{-2} (overdensity) in the bottom-left sector.

ter: *the dependence on loop length*. In this case overdense loops are generally short ($L < 100$Mm) whereas underdense loops are generally long ($L > 300$Mm).

Figure 4.14 generalises these results by plotting the regions of overdensities and underdensites onto the heating profile plot described in Section 4.2 (Fig. 4.2). As can be seen, regions of maximum and minimum temperatures reside in these areas. Observations suggest cool (EUV) overdense loops and hot (X-ray) underdense loops. Winebarger *et al.* (2003) find loops observed by *TRACE* are overdense structures and loops observed by SXT are underdense structures, concluding hydrostatic loop models are insufficient to explain the densities of coronal loops. It can therefore be suggested that hot, X-ray loops will result from high-$l_{\rm drive}$, high-L models and EUV/cool loops will result from low-$l_{\rm drive}$, low-L models. The turbulence heated coronal loops described in this thesis appear to support general observational findings, although no definitive loop length-temperature relationship exists at present.

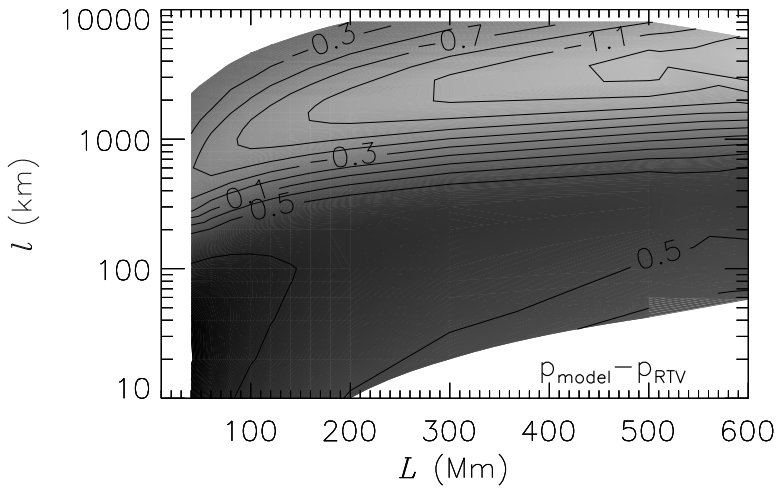

Figure 4.13: From Fig. 4.10, $p_{\rm model} - p_{\rm RTV}$ is plotted. For the $\xi = 14$kms^{-1} dataset, differences in pressure between loops range from $\Delta p \sim -1.4$ dyne cm^{-2} (underdensity) in the top-right sector to $\Delta p \sim 1.6$ dyne cm^{-2} (overdensity) in the bottom-left sector.

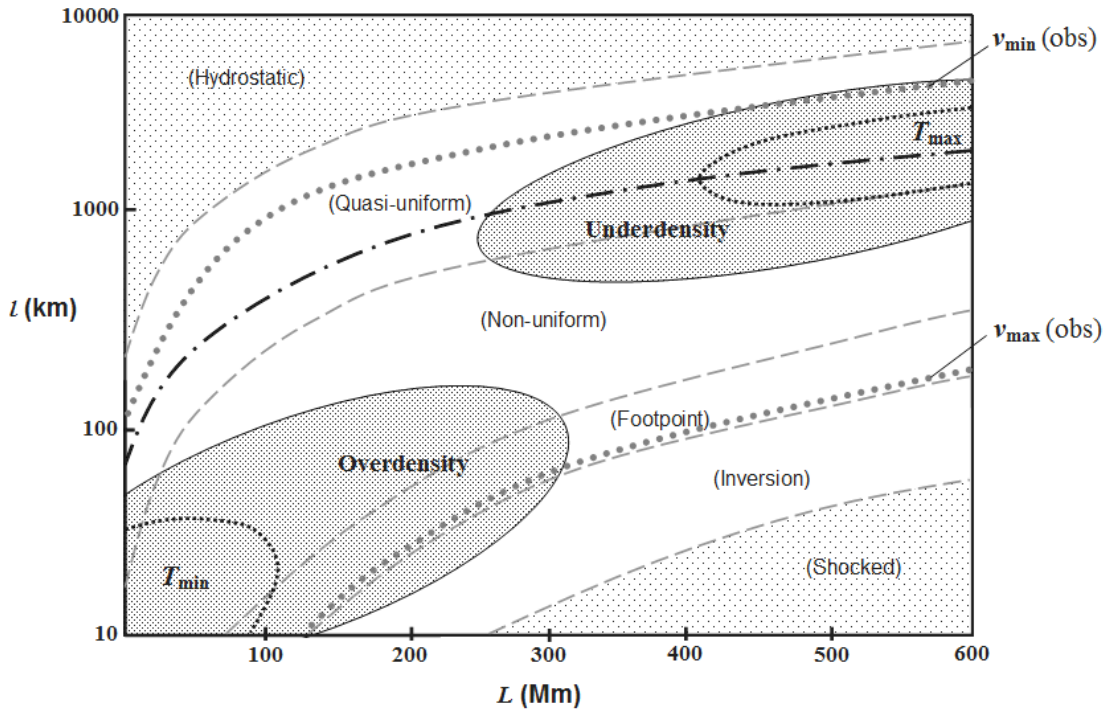

Figure 4.14: As Fig. 4.2 but regions of overdensity and underdensity are included. The region of 'optimised heating' (see Fig. 4.6) is included (*dot-dashed* line) with regions of general loop underdensities and overdensities (labelled). Maximum and minimum temperatures reside in these regions. *Dashed*, grey lines represent the boundaries between loop heating profiles (replicated from Fig. 4.2) and grey *dotted* lines represent the maximum and minimum observed velocities for quiescent loops.

4.6 Discussion

This chapter demonstrates the unique numerical method described in Chapter 3 can produce densities comparable with *TRACE* and EIT loops (Fig 4.15; Aschwanden *et al.* 2000a,b). Hot X-ray loops with densities comparable with SXT observations (Kano & Tsuneta, 1995) can also be produced. Steady flow loop models can enhance loop densities far higher than hydrostatic simulations (Winebarger *et al.*, 2002, Patsourakos *et al.*, 2004) but these models still fail to explain the high density observed by *TRACE* and EIT (see Fig. 4.16 for a loop modelled by Winebarger *et al.* 2002). It is demonstrated here that *momentum deposition by Alfvén waves improves modelled coronal loop densities*. This also supports the idea that EUV and SXT loops *may* share a similar

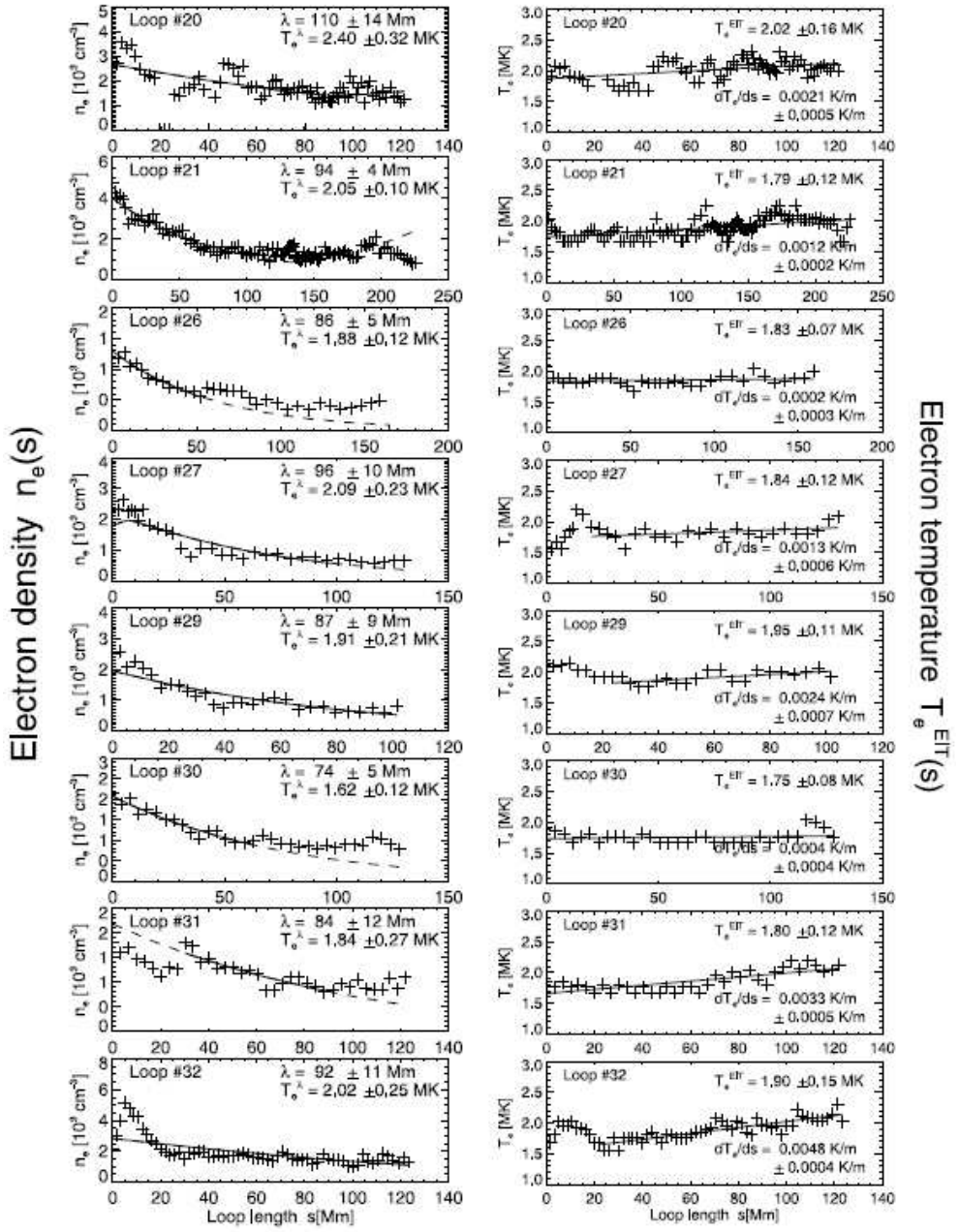

Figure 4.15: Observed electron temperature and density profiles along a selection of loops (as presented by Aschwanden *et al.* 2000a in Figures 5 and 6). Temperature values are derived from applying the filter ratio method to the 284Å and 195Å EIT bandpasses (which has some shortcomings as identified in Section 1.6). From this small selection of 8 loops of varying length, it is evident that the model results in Figures 4.1, 4.3 and 4.4 appear to approximate observed parameters depending on the balance between the turbulence variables ξ and l_{drive}.

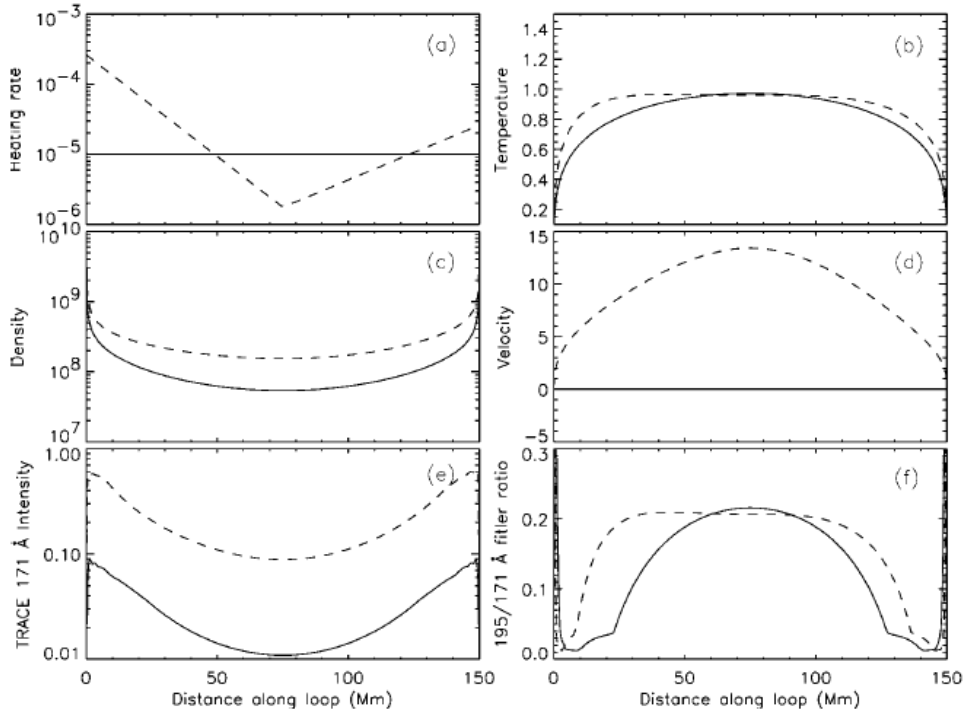

Figure 4.16: Modelled loop parameters for a 150Mm isothermal loop heated by an *ad-hoc* (non-uniform, 'V'-shaped) heating rate (from Fig. 3 in the Winebarger *et al.* 2002 study). The parameters modelled for a loop heated by a uniform heating rate (*solid* line) and a non-uniform heating rate (*dashed* line) are shown. Note the plasma density of this loop is significantly lower than modelled *wave-driven* loops of this length shown in Fig. 4.1 and Fig. 4.3 and observed loops shown in Fig. 4.15.

(wave-momentum deposition) heating mechanism (Winebarger *et al.*, 2003, Schmieder *et al.*, 2004). This important finding is discussed in Section 4.5 by relating the parameter study results with classical models (Rosner *et al.*, 1978). A strong relationship between L, $l_{\rm drive}$ and over/underpressure is obvious, providing evidence that hydrodynamic loops heated by MHD waves can improve coronal loop densities for short coronal loops (overdensity) and improve results for long coronal loops (underdensity).

The effect of ξ on the loop solutions mainly governs the energy flux injected into the plasma. A brief comparison of the $\xi = 10\text{kms}^{-1}$ and $\xi = 14\text{kms}^{-1}$ results (Section 4.2) shows hotter, more dense loops result from an increase in Alfvén wave amplitude. The magnitude of ξ has a large influence on the loop footpoint plasma characteristics

too, this becomes evident when attempting to model "moss" solutions (investigated in Section 5.6).

On modelling the evolution of ξ along a coronal loop (Section 4.4), implications for the possibility of Alfvén wave propagation generating non-thermal velocities are very interesting. From Fig. 4.8, the maximum non-thermal velocities can be related to temperature, thus giving a picture of how modelled non-thermal velocities (or ξ) compare with observation.

The driving scale ($l_{\rm drive}$) of turbulence is key to the heating of the modelled coronal loops. As discussed in this chapter, $l_{\rm drive}$ strongly influences plasma flow velocity and loop density to a high degree. If we compare the final solution velocities with the observed loop velocity range of 5-60kms^{-1}, one is able to see which solutions fall within the region of observed velocities. Figure 4.14 marks this region between the *dotted* lines labelled v_{max}(obs) (maximum observed velocity of 60kms^{-1}; Saba & Strong 1991) and v_{min}(obs) (minimum observed velocity of 5kms^{-1}; Spadaro *et al.* 2000). From this figure it is reasonable to propose that the extreme velocity solutions ($v > 60$kms^{-1} and $v < 5$kms^{-1}) may be flows that have yet to be discovered or indeed do not exist in dynamic quiescent loops. Loops exceeding $v > 60$kms^{-1} are interesting features demonstrating a 'double hump' (exaggerating the gravitational influence on loop heating) in temperature profile and should not be discounted from this work.

Shocked solutions (investigated in Section 5.7) exist in the most extreme flow velocities ($v \sim c_{\rm s}$) at very low driving scales. The numerical method (Chapter 3) cannot calculate rapid changes in plasma parameters (such as the characteristic discontinuity of plasma parameters across the shock front), but some steady state shock solutions are possible if the time-step of the calculations are reduced to improve the code stability.

Chapter 5

Unique Loop Solutions

5.1 Introduction

The results gained in Chapter 4 provide a summary of the strengths and limitations of the numerical method. By investigating parameter space through the very general method of mapping hundreds of loops, solutions are extracted to model certain coronal phenomena.

This chapter will outline a number of case studies where the mapping method in the parameter study is used to pin-point certain areas of interest for further investigation and development. As this model simulates protons and electrons out of thermal equilibrium, Section 5.2 investigates some situations where Coulomb coupling between species varies in efficiency, causing thermal non-equilibrium. Section 5.3 approaches isothermal modelling of coronal loops and addresses some of the main pitfalls with maintaining an isothermal state through wave heating. This leads to Section 5.4 where the consideration of loop inclination may play a very important role in observations and models alike. Case studies of cool loop solutions, EUV 'moss' and wave-driven shocks are detailed in Sections 5.6, 5.6 and 5.7 respectively.

5.2 Non-Equilibrium of Electron and Proton Plasma

The two-fluid nature of the model aids the understanding of the interaction between plasma species. The Coulomb collision frequency, ν_{pe} (Eq. 3.8), is strongly influenced by density. Figures 5.1 and 5.2 are results arising from the effect of the driving scale on plasma parameters. Figure 5.1 demonstrates a 500Mm loop where the majority of the coronal section has a large difference in species temperature (electron temperature is the *bold line* and proton temperature is the *dotted line*). As the driving scale is high, minimum matter is driven from the chromospheric reservoir. The plasma velocity and loop density is therefore low. This has implications for ν_{pe} in that the efficiency of energy transfer in the form of collisions will be low in the coronal section of the loop. A 500Mm loop is used in Fig. 5.1 to exaggerate the non-equilibrium for clarity, but it can be expected that significant non-equilibrium will exist across all L and all ξ at

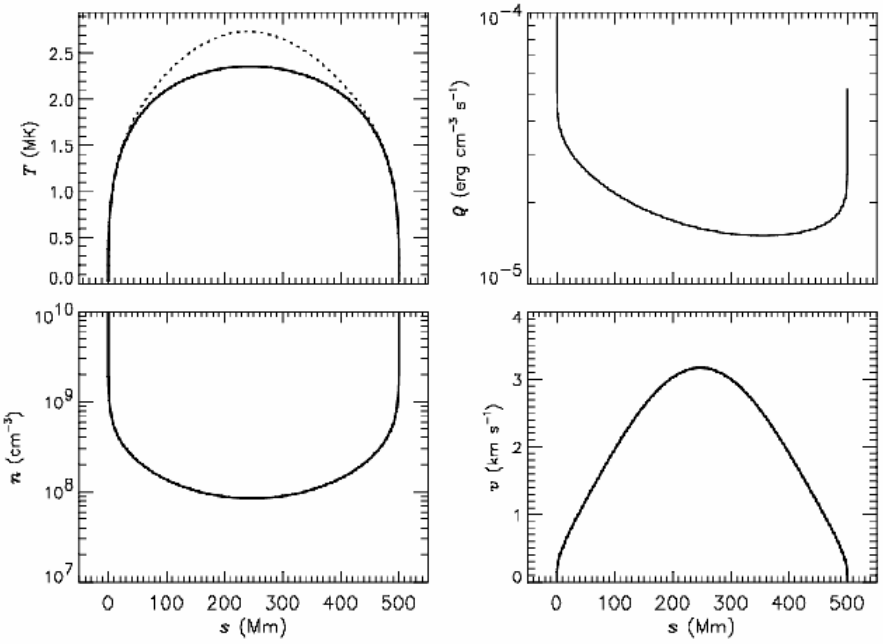

Figure 5.1: A 500Mm loop out of electron (*bold line*) and proton (*dotted line*) thermal equilibrium for the majority of its coronal section. The driving scale is a maximum for the loop length and Alfvén wave amplitude is set at an arbitrary value (when l_{drive} is maximum for any L, a similar profile is acquired across all L). Clockwise from top-left: temperature profile, heating rate, velocities and density profile.

maximum $l_{\rm drive}$.

Significant non-equilibrium may be evident in loops with high $l_{\rm drive}$ (and low density), but non-equilibrium between the two species can exist in loops driven by low-$l_{\rm drive}$ waves. As shown in Fig. 5.2, the driving scale is at a minimum for the example 500Mm coronal loop. Plasma density is likely to be at a maximum at minimum-$l_{\rm drive}$, so it can be expected that ν_{pe} will be at its most efficient when transferring energy from proton to electron gas. However, even at low driving scales non-equilibrium can occur due to an energetic 'overshoot' (circled). As plasma is driven from the chromosphere in the first footpoint, highly energetic waves will accelerate the plasma (primarily the proton gas) into the corona at high velocity. The density is also high, but Coulomb coupling cannot transfer thermal energy fast enough to prevent a local non-equilibrium above the first footpoint. At low driving scales, the characteristic double hump feature is evident

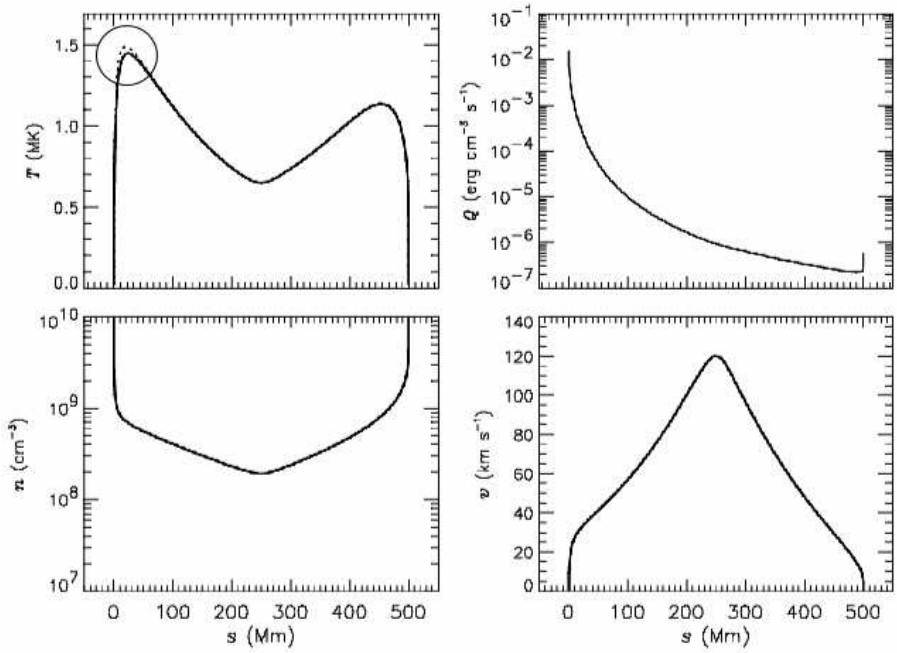

Figure 5.2: A 500Mm loop held at minimum-$l_{\rm drive}$ (before becoming shocked). A small 'overshoot' in proton temperature can be observed (circled) where Coulomb coupling cannot transfer energy fast enough to the electron gas. Equilibrium is re-instated very quickly in the coronal section due to high flow velocity and density. Clockwise from top-left: temperature profile, heating rate, velocities and density profile.

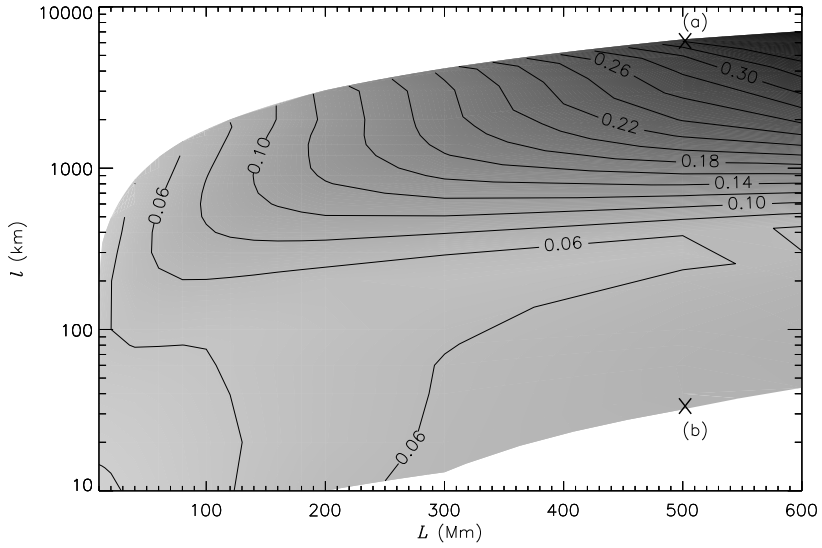

Figure 5.3: Data from the ξ=10kms^{-1} study (Fig. 4.1), showing temperature non-equilibrium ($T_{\mathrm{p(max)}} - T_{\mathrm{e(max)}}$) between protons and electrons, for the complete range of ξ and l_{drive}. Temperature values quoted in MK. The label (a) corresponds to the location of the solution in Fig. 5.1 and (b) is the location of the solution in Fig 5.2

in long loops, highlighting the local non-equilibrium.

Figure 5.3 demonstrates the non-equilibrium between electrons and protons ($T_{\mathrm{p(max)}} - T_{\mathrm{e(max)}}$) for the range of loop lengths and driving scales in the $\xi = 10\mathrm{kms}^{-1}$ study. The non-equilibrium in proton and electron temperatures increases with loop length and l_{drive}. There is a maximum temperature difference for long loops ($L > 400$Mm) at large driving scales (l_{drive} >1000km), reaching a maximum of 0.38MK for the L = 600Mm loop at $l_{\mathrm{drive}} = 7000$km. Loops heated by various Alfvén wave amplitudes exhibit similar features. Long solutions heated by high-l_{drive} waves are at maximum non-equilibrium, whereas short loops at low-l_{drive} exhibit very little non-equilibrium.

Some models assume the main constituents of coronal loop plasma (i.e. protons and electrons) are in thermal equilibrium. Lenz (2004) construct a hydrodynamic model with this in mind but also assume minor ions are heated higher than the electron/proton equilibrium temperature. Bradshaw & Mason (2003) model 15 abundant ions in a cool-

ing coronal loop and find significant non-equilibrium between species when simulated time-dependently. The unique model described in this thesis only considers a two-fluid plasma where there is strong Coulombic interactions between protons and electrons, but non-equilibrium is found to be commonplace (especially when plasma density is low).

5.3 Isothermal Loop Solutions

Chapter 4 investigates isothermal loops embedded within the parameter space. This case study extracts a selection of loop lengths from results that exhibit near-isothermal properties. The turbulence variables are then adjusted so temperature profiles are approximately isothermal. This is a very difficult process as there appears to be very few unique isothermal solutions for a given loop length. The criteria imposed on the output solution is the temperature difference between temperature maximum and apex temperature should not exceed 2% of the temperature maximum (i.e. $[T_{\max} - T_{\text{apex}}]/T_{\max} \leq 0.02$). This value was arrived at through trial and error and by comparing our modelled results with the observations (Neupert *et al.*, 1998, Lenz *et al.*, 1999). Table 5.1 summarises the results of four modelled isothermal loops of different lengths corresponding to the profiles in Fig. 5.4.

Figure 5.4 plots the isothermal temperatures for each loop length. l_{drive} and ξ are ad-

Table 5.1: The values of loop length (L), driving scale (l_{drive}), Alfvén wave amplitude (ξ) and approximate chromospheric temperature (T_{foot}) from Chae *et al.* (1998) to produce stable isothermal solutions detailed in Fig. 5.4. The maximum temperature ($T_{\max}$) attained by each loop is also detailed.

L (Mm)	l_{drive} (km)	ξ (kms^{-1})	T_{foot} (K)	$T_{\max}$ (K)
100	10	4.3	1.2×10^4	1.0×10^6
200	20	4.5	1.2×10^4	1.2×10^6
300	48	5.4	1.3×10^4	1.6×10^6
600	190	7.9	1.4×10^4	2.8×10^6

justed until the coronal section of each loop falls within a variance of 2%. It is worth noting that although there appears to be one unique isothermal solution for a given loop length, the magnetic field strength (B_0) remains a constant throughout (at 80G). After experimentation it is found that decreasing B_0 results in cooler loops, thus decreasing the isothermal temperature.

For the range of loops from L = 100Mm to L = 600Mm, isothermal loops can be modelled. However there is a very strong relationship between loop isothermal temperature and loop length, a relationship not currently observed by *TRACE* or EIT. Loop inclination also has a factor to play in that the gravitational energy component acting on the loop will decrease with χ, degrading the isothermal profile in favour of an asymmetric temperature profile.

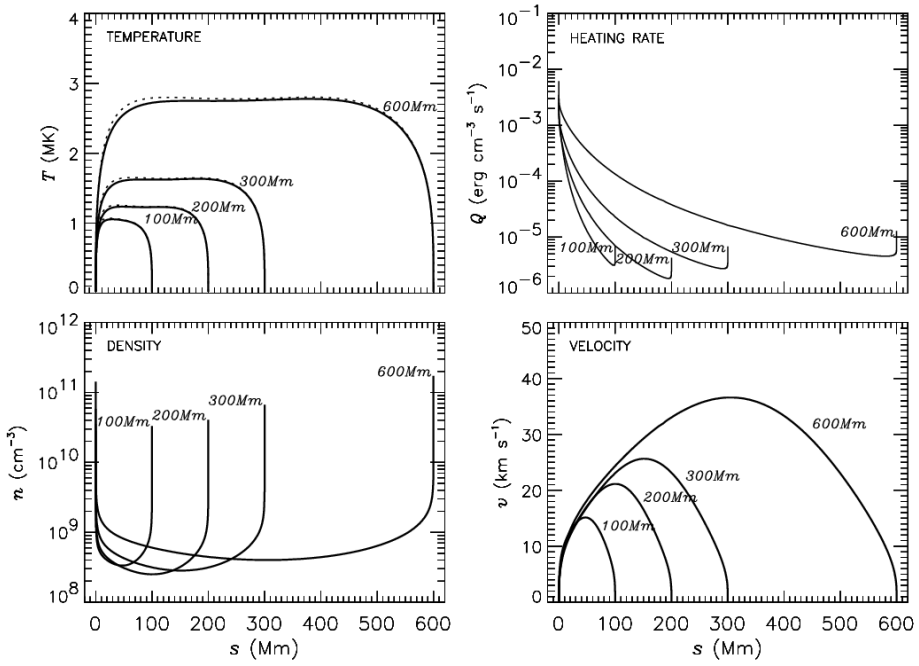

Figure 5.4: A selection of isothermal coronal loop solutions of loop lengths L =100Mm, 200Mm, 300Mm and 600Mm. The model parameters are listed in Table 5.1. Clockwise from top-left: proton (*dotted* line) and electron (*solid* line) temperature profiles, heating rate, velocities and density profile.

5.4 The Effect of Loop Inclination

As discussed in Section 3.2.1, it is rare to find a perfectly vertical coronal loop, many loops evolve at an angle from the vertical due to magnetic pressures of neighbouring loops, magnetic configuration or plasma load (Aschwanden *et al.*, 2000a). Loop inclination reduces the gravitational energy flux component (Section 3.7), thus reducing the enthalpy energy flux, cooling the loop. Equation 3.10 describes the gravitational component of the basic equations modelled in this work where the variable χ (loop inclination) has a profound effect on the loop plasma parameters (Reale, 1999, Aschwanden *et al.*, 2000a, Tsiklauri & Nakariakov, 2001). Figure 5.5 demonstrates the progression of an isothermal loop as it is inclined from vertical (0°) to horizontal (90°) to the solar

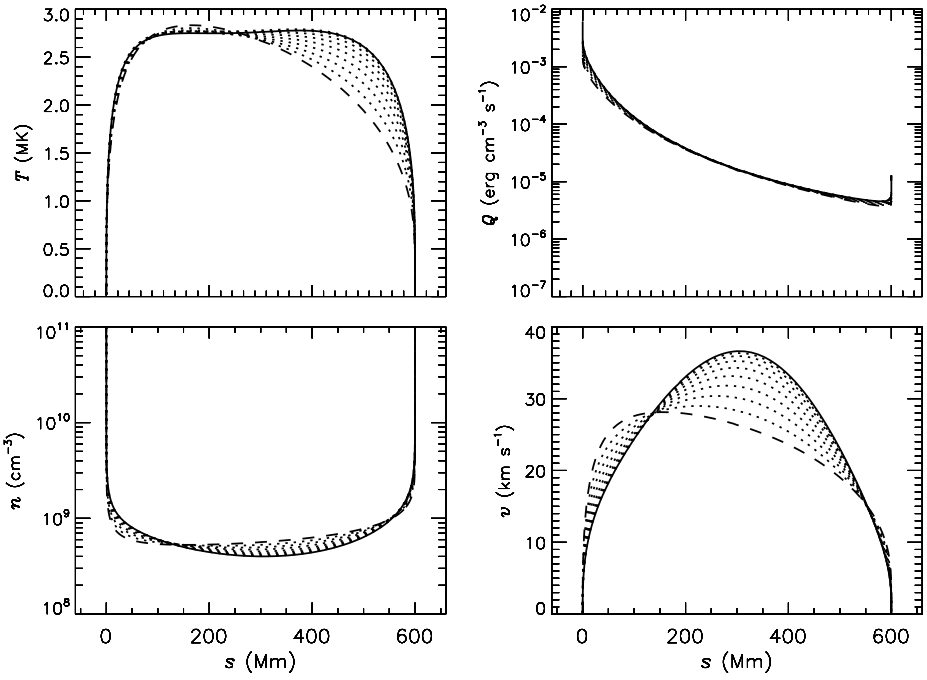

Figure 5.5: A 600Mm isothermal loop inclined from $\chi = 0°$ (vertical) to the extreme $\chi = 90°$ (horizontal) in 10° increments. The starting (isothermal) state has a *bold line*, the 10° increments are *dotted lines* and the final $\chi = 90°$ state has a *dashed line*. Clockwise from top-left: proton temperature profile, heating rate, velocities and density profile.

surface. A long, $L = 600$Mm loop is used so the effect on the plasma parameters are obvious.

As expected, the loop generally cools as χ is increased, however the maximum temperature above the left (upflowing) footpoint does not cool (there is in fact slight heating). This effect may be due to the lack of gravity countering plasma flow when driven by wave energy flux. The isothermal temperature profile is lost very quickly, developing an asymmetric profile as the loop is inclined further. This behaviour is expected, as already mentioned, the enthalpy energy flux (self heating) will be drastically interrupted as the driving gravitational energy flux is reduced. It is therefore logical to conclude that isothermal temperatures cannot be maintained (Section 5.3) if the loop is inclined beyond 30°, the heating source for the downflowing footpoint is weakened and eventually cancelled out as χ approaches 90°. There is little change in the heating rate along the loop, however plasma velocity becomes more asymmetric and is reduced by $\sim 25\%$. Plasma density expriences a slight increase as χ is increased. This behaviour is evident across all loop lengths, but greater in long loops.

5.5 Cool Loop Solutions

Cool coronal loops have a temperature range of $0.02 > T > 1$MK and have often been associated with the cooler plasma flowing from sunspots in active regions (Foukal, 1975, 1976, Bray *et al.*, 1991). Active regions are usually under intense study for sunspot activity and flaring, hot loops. The existence of cool, steady loops are therefore of particular interest. Cool loops are often found in close proximity to hot coronal loops and can be orders of magnitude cooler than the surrounding plasma, very little thermal conduction acts perpendicular to the field lines (Habbal *et al.*, 1985). Cool loops will therefore contrast greatly, appearing dark against the highly radiating, hot plasma. Foukal (1975,

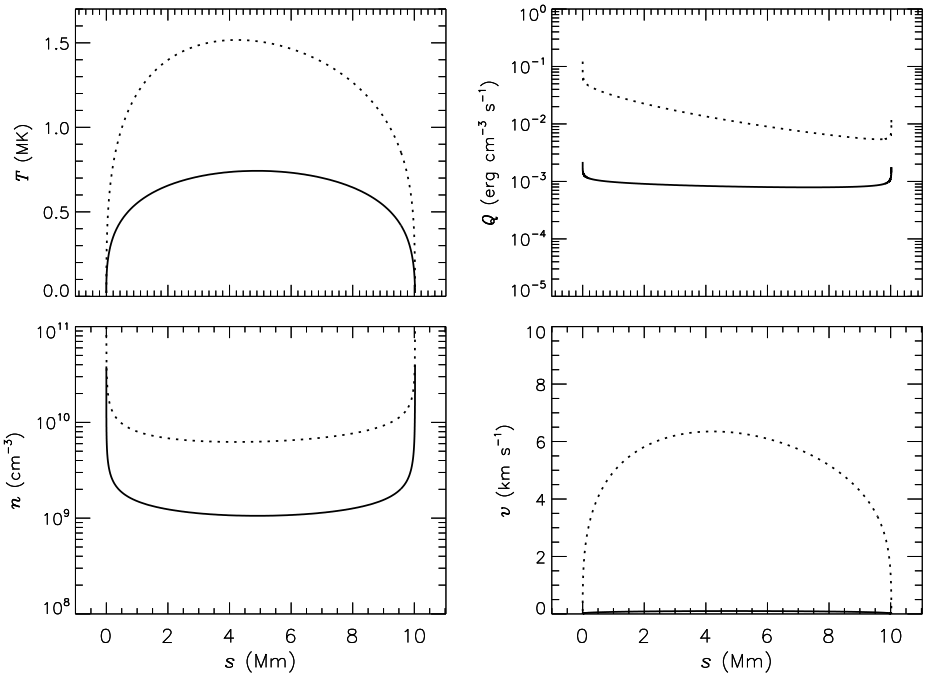

Figure 5.6: A cool, L = 10Mm loop example (*bold line*) as compared with the hottest L = 10Mm loop solution (*dotted line*). $l_{\rm drive}$ = 280km for the coolest loop, $l_{\rm drive}$ = 10km for the hottest loop. ξ = 10kms^{-1} remains constant. Clockwise from top-left: proton temperature profile, heating rate, velocities and density profile.

1976) analyse *Skylab* data and find cool loops can only exist through dynamic plasma flow. Their internal pressures can be expected to be lower than the surrounding plasma and densities of surrounding loops will generally be higher.

A large array of coronal loops can be arrived at from the parameter study in Chapter 4, so it may be possible that MHD wave activity can sustain a flow along cool loops whilst maintaining a locally low temperature.

To evaluate the coolest loops as outputted in the results, the shortest loop (L = 10Mm) from the ξ = 10kms^{-1} dataset (Fig. 4.1) is presented in Fig 5.6. The coolest loop solution for this length is compared with the hottest loop solution, $l_{\rm drive}$ = 280km (*solid line*) and $l_{\rm drive}$ = 60km (*dotted line*) respectively. In this example, it is found the coolest solution has a temperature maximum of under 0.8MK and a minimum density of 10^9cm^{-3}

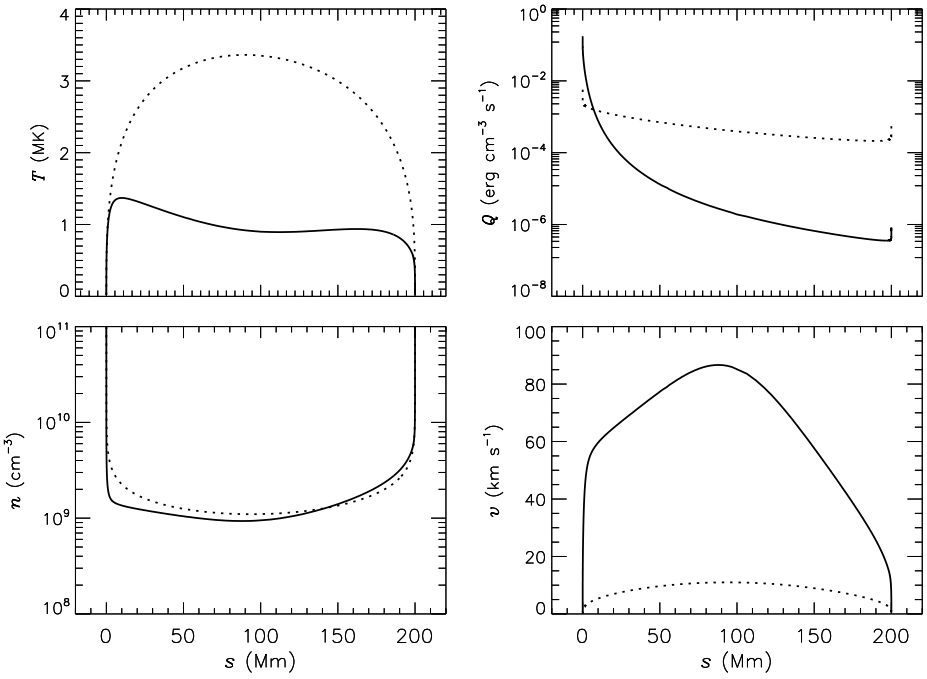

Figure 5.7: The coolest, $L = 600$Mm loop example (*bold line*) as compared with the hottest $L = 600$Mm loop solution (*dotted line*). $l_{\rm drive} = 58$km for the coolest loop, $l_{\rm drive} = 2000$km for the hottest loop. $\xi = 14$kms^{-1} remains constant. Clockwise from top-left: proton temperature profile, heating rate, velocities and density profile.

(there is no cooler solution below $l_{\rm drive} = 10$km). The heating profile is quasi-uniform, suggesting minimum plasma is driven into the loop. The flow velocity will therefore be expected to be low ($v \sim 0$). If cool loops are to be maintained in active regions, there must be a strong flow of plasma. In this case, there is approximately zero flow suggesting short and cool coronal loops cannot be sustained in such regions. The maximum flow velocity ($v = 18$kms^{-1}) is associated with low driving scales and *maximum* temperatures ($T = 1.3$MK). It is also worth noting the enhancement in loop density of nearly one order of magnitude (from $\sim 10^9$ to $\sim 10^{10}$) as $l_{\rm drive}$ is decreased from 280km to 10km.

A different pattern emerges as loop length is increased. Figure 5.7 is a longer loop ($L = 200$Mm) from the same $\xi = 10$kms^{-1} dataset (Fig. 4.1). Again, the coolest loop

is compared with the hottest loop for this length. This time it is found the coolest solution is the most dynamic solution (whereas in Fig. 5.6, the coolest loop was quasi-hydrostatic). The coolest solution cannot be cooled below 1MK as the $\xi = 10\text{kms}^{-1}$ waves cannot support lower driving scales (below $l_{\text{drive}} = 58\text{km}$), so technically is not a 'cool' loop, but this comparison remains useful. As a general rule, we acquire cool loop solutions at both extremes of plasma flow. Cool solutions exist for quasi-hydrostatic loops and for highly dynamic loops. In the case of Fig 5.6, it so happens the *coolest* loop resides in the quasi-hydrostatic (maximum-l_{drive}) region, but in the case of Fig. 5.7, the *coolest* loop resides in the highly dynamic (minimum-l_{drive}) region. All values of ξ produce a similar pattern. For loops of $L < 100\text{Mm}$, the coolest solutions can be found in quasi-hydrostatic states and for loops of $L > 100\text{Mm}$, the coolest solutions can be found in highly dynamic states (but often at velocities exceeding that of observations; Saba & Strong 1991, Spadaro *et al.* 2000, Winebarger *et al.* 2002).

In conclusion, this model reproduces relatively cool loop solutions (w.r.t. the majority of solutions) with both dynamic and quasi-hydrostatic characteristics, but to cool the loop sufficiently ξ needs to be very low. Only then can l_{drive} be reduced to optimise both flow speed (within the 5-60kms^{-1} observed range) and minimum temperature ($T < 1\text{MK}$). Generally, the wave heating outlined in this thesis produces hot loops; cool solutions are difficult to arrive at. Cally & Robb (1991) find that cool loops of temperatures lower than the ones discussed here are generally unstable and evolve very quickly into a hot state. It is also more likely long loops will remain 'cool' for a longer period, contradicting the main results in this study that cool loop solutions are generally short.

5.6 Modelling Transition Region 'Moss'

Some of the hotter solutions detailed in Chapter 4 demonstrate low-altitude plasma exhibiting characteristics of EUV 'moss' as observed by the Coronal Diagnostic Spectrometer (CDS) onboard *SOHO* (Berger *et al.*, 1999). EUV moss can often be observed in the footpoints of some X-ray loops. Peres *et al.* (1994) report findings from the Normal Incidence X-ray Telescope (NIXT) where regions of intense brightness are observed in the lower regions of hot (X-ray) coronal loops. Peres *et al.* relates intense low lying EUV emission (or 'Hα plage') with X-ray loops and state that instruments sensitive to 10^4-10^6K emission can be used to search for the footpoints of X-ray loop systems. However the loops are assumed to be in hydrostatic equilibrium (i.e. they lack plasma upflow).

In this model, as the plasma rises by chromospheric evaporation, it is heated through EUV temperatures (0.6–1.6MK) at approximately 2Mm above the photosphere (allowing it to be observed by instruments that operate with band passes within the EUV wavelengths). The moss emission tends to be restricted to a thickness of 1Mm and exists at pressures in the range of 0.7-1.7 dyne cm^{-2} (fulfilling the criteria outlined by Berger *et al.* 1999). Dynamic plasma upflows are also observed in these regions.

By focusing on the footpoints of the long and hot solutions modelled in this thesis, conditions for observed EUV moss have been met for a range of loops. Figure 5.8 shows the plasma temperature, velocity, density and pressure profiles of 5 hot, L=300Mm loops that fall within or close to the criteria for observed EUV moss.

For all results, $l_{\rm drive}$ is kept at a constant 4000km, whilst ξ is increased 11-15kms^{-1}. The temperature and pressure requirements are boxed in the top-left and bottom-right frames. From this simple analysis the two solutions that successfully model moss characteristics (matching both the temperature and pressure conditions) are ξ=12kms^{-1} and

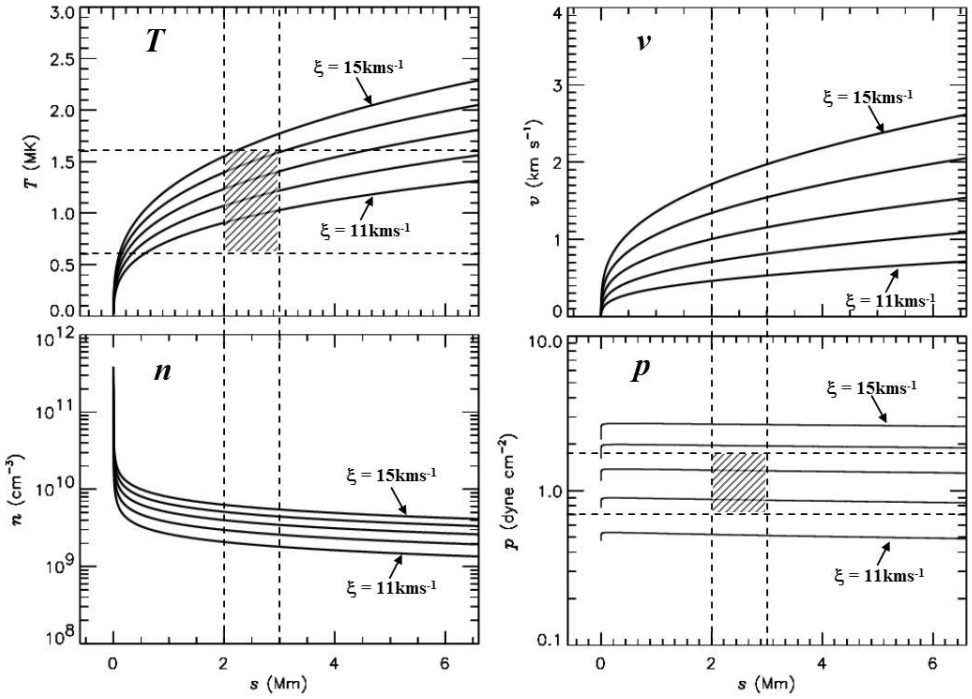

Figure 5.8: Solutions from the model (L = 300Mm) with 'moss' characteristics. The dashed lines represent the boundaries matching values quoted by Berger *et al.* (1999) of observed parameters of EUV moss. Clockwise from top-left: footpoint proton temperature, velocities, pressures and densities.

ξ=13kms^{-1}. As more energy flux is injected into the loop (by increasing ξ), the loop footpoint undergoes increases in plasma temperature, density (therefore pressure) and velocity. ξ appears to have a strong influence on moss characteristics. $l_{\rm drive}$ has a more influential effect on the higher sections of hot loops, but has negligible influence on lower regions. This is highlighted in Fig. 4.6 in Section 4.4 where the driving scale is increased to change the overall structure of a long coronal loop.

Figure 5.8 demonstrates the coronal loop model used in this study can readily simulate the observed characteristics of EUV moss in the lower corona. In conclusion, it appears EUV moss may be symptomatic of rapid wave dissipation in the footpoints of long, hot coronal loops, allowing instruments observing EUV emission (e.g. *TRACE* and EIT) to search for large-scale X-ray loops (Peres *et al.*, 1994).

5.7 Shocks

Chapter 4 demonstrates the difficulty the numerical method has with acquiring steady state for low-$l_{\rm drive}$ and supersonic flow. At low-$l_{\rm drive}$, long loops exhibit a temperature inversion which quickly moves toward a quasi-shocked state. A shock is characterised by a sudden increase in density followed by a sharp drop in flow velocity. These rapid changes will appear almost as a discontinuity. Due to the rapid change in plasma parameters the numerical method will not converge to a steady state for long loops ($L > 200$Mm) at low-$l_{\rm drive}$. However it is suspected there is a transition zone between temperature inversion and shocked solutions where standing shocks may be modelled.

This scenario is investigated by Orlando *et al.* (1995b) where a shocked loop with a modelled siphon flow was presented. Supersonic flow was modelled in a very hot ($T_{\rm max} \sim 7$MK) loop of half-length $L_{1/2} = 5 \times 10^{10}$cm ($L = 1000$Mm). In an adiabatic situation ($\gamma = 5/3$), it is found a shock forms toward the downflowing half of the loop, creating a discontinuity in temperature profile (an increase of ~ 4MK at the shock front), density profile (an increase of $\sim 2 \times 10^{7}$cm^{-3}) and velocity profile (a decrease of ~ 400kms^{-1}). In the model presented here, a similar pattern emerges, although the magnitude of the shock on modelled parameters is less dramatic.

Figure 5.9 presents two shocked solutions for the $L = 600$Mm loop, one heated by $\xi = 7$kms^{-1} waves (*solid line*) and the other by more energetic $\xi = 14$kms^{-1} waves (*dashed line*). As shocked solutions reside in low-$l_{\rm drive}$ regions of the parameter space (Chapter 4), it is expected that all shocked loops will have very intense (and localised) heating above the upflowing footpoint. As the loop cools from the upflowing footpoint temperature maximum ($T_{\rm max}$), the plasma reaches a local minimum at approximately $s = 350$Mm (as predicted, the $\xi = 14$kms^{-1} loop is warmer than the $\xi = 7$kms^{-1} loop) before experiencing a sharp increase of ~ 0.5MK. Loop density also undergoes a

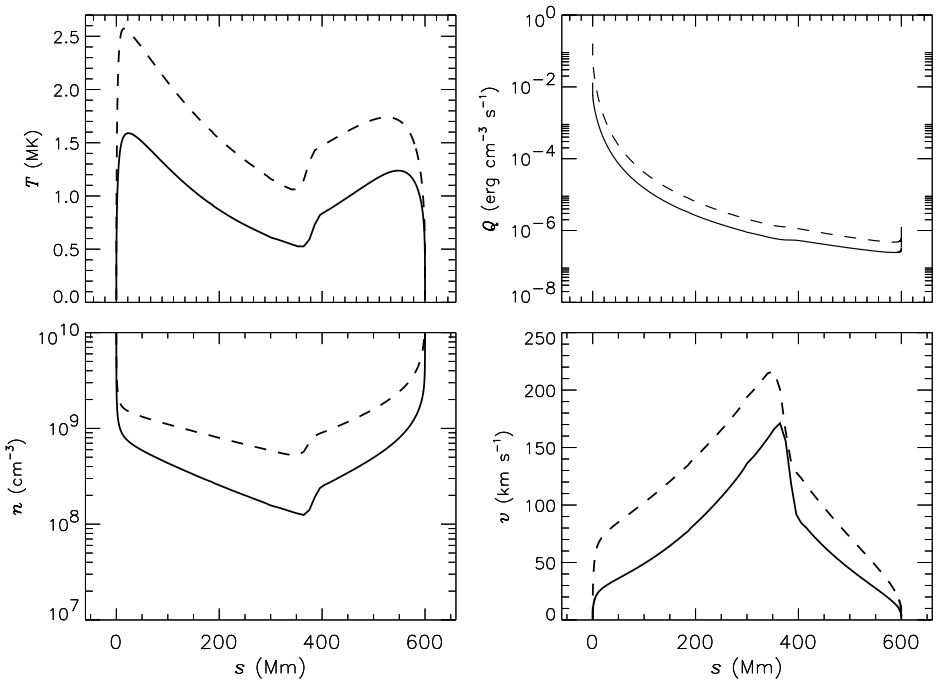

Figure 5.9: Standing shocks for a 600Mm loop. This example remains in steady state with no appreciable change in plasma parameters. A loop heated by $\xi = 7\text{kms}^{-1}$ waves (*solid line*) is compared with a loop heated by $\xi = 14\text{kms}^{-1}$ waves (*dashed line*). $l_{\text{drive}} = 30\text{km}$ and $l_{\text{drive}} = 50\text{km}$ respectively. The shock develops very quickly in both solutions (in under 100s) and this figure is 500s into the simulation. To improve calculation stability the model time-step length is reduced from 10s to 0.1s and the iterative approach is applied. Clockwise from top-left: proton temperature, heating rate, velocity and density.

rapid increase over a short distance of $s \approx 25$Mm. There is a discontinuity in plasma flow speed in the same location. Both loops indicate a rapid drop in velocities through the shock (a velocity difference of -50% for the $\xi = 7\text{kms}^{-1}$ solution, -40% for the $\xi = 14\text{kms}^{-1}$ solution). The position of the shock does not deviate significantly from $s = 350$Mm. As most of the loops modelled appear to produce velocity maximum at the loop apex, all lengths produce a standing shock on the downflowing section, just after the loop apex. An increase in ξ causes an increase in loop temperature, loop density and velocity, but does not greatly influence the position or magnitude of the shock. Orlando *et al.* (1995b) predicted shock formation at $T_{\max}$ whereas this model predicts shock formation at the local $T_{\min}$, but both predict shock formation beyond the loop apex, in the downflowing section. Cargill & Priest (1980) support the formation of shocks in the downflowing section of the loop, although this model does not consider the effect of gravity. The solution in Fig 5.9 cannot shock for loops with a temperature maximum at the loop apex as generally flow speed is not close to the local sound speed, only loops with focused heating above the upflowing footpoint can acquire supersonic flow. Robb & Cally (1992) also model standing shocks as a result of supersonic siphon flow and find similar results. There is a shock in the downflowing section of the loop at velocities comparable with the model in Fig. 5.9.

Shocked flow is characterised by the *Mach number*. The Mach number is a simple ratio between flow velocity (v) and local sound speed (c_{s}) in the plasma

$$M = \frac{v}{c_{\text{s}}} \tag{5.1}$$

where the sound speed is

$$c_{\text{s}} = \left[\frac{p}{\rho}\right]^{1/2} \approx \left[\frac{k\left(T_e + T_p\right)}{m_p}\right]^{1/2} \tag{5.2}$$

where parameters are as previously stated (in Section 3.2.1). With reference to the results in Fig. 5.10, the flow velocity for the $\xi = 7\text{kms}^{-1}$ loop is plotted against local sound speed and Mach number. On comparison with 5.9, there is strong heating above the upflowing footpoint due to the very low-l_{drive}, causing a temperature maximum at $T = 1.6\text{MK}$. There is a steady decrease in plasma temperature (both T_p and T_e are in equilibrium) until the shock forms. The flow velocity (*dashed line*) rises steadily until it matches the local sound speed (*dash-dot line*). The sound speed is strongly dependent on plasma temperature (Eq. 5.2) and therefore decreases toward the cool loop apex. At this point, $M = 1$ (a.k.a. *transonic flow*). Plasma flow can be seen to decelerate as as it flows supersonically ($M > 1$). The shock front quickly forms at approximately $s = 350\text{Mm}$, causing a sharp increase in density and a sharp drop-off in flow velocity until the flow becomes subsonic in the down-flowing section of the loop.

For any detailed study of shocked solutions, better resolution is required in the model

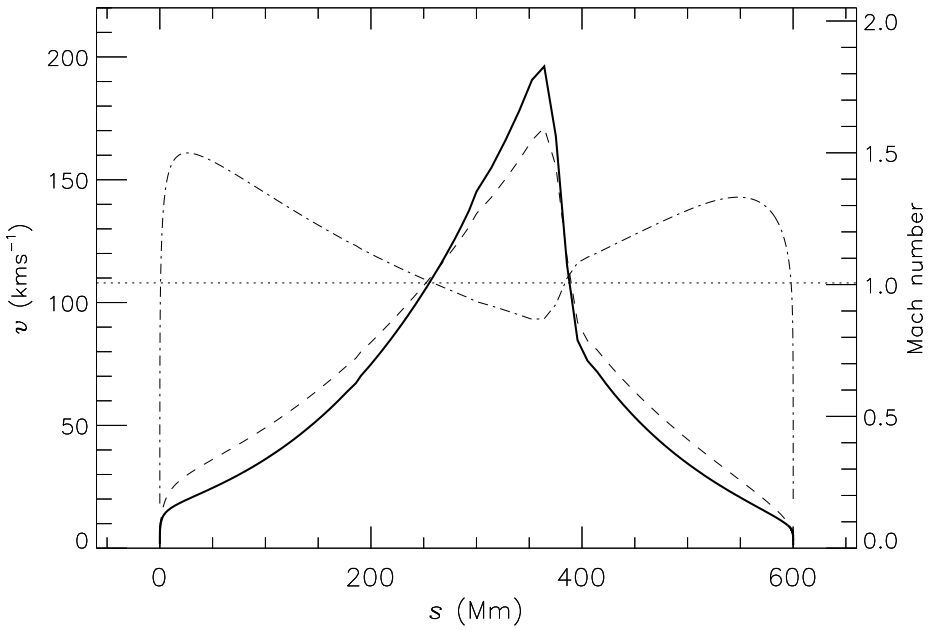

Figure 5.10: The shocked plasma velocity profile along the $\xi = 7\text{kms}^{-1}$ solution in Fig. 5.9. The Mach number (Eq. 5.1) along the loop (*thick solid line*), flow velocity (v; *dashed line*) and plasma sound speed (c_s; *dot-dash line*) are plotted. The horizontal *dotted line* marks where $M = 1$ (at $\sim 110\text{kms}^{-1}$).

loop apex. Currently all the loops have maximum resolution toward the loop footpoints and minimum resolution at the loop apex (up to 1Mm grid spacing for the $L = 600$Mm loop discussed here). Where there are sudden changes in plasma parameters, better resolution is required so the model remains stable and the small-scale fluctuations can be examined.

It is important to note that shock charateristics will change if the gravitational component is reduced (the loop is inclined). As χ increases, g decreases, reducing the gravitational energy flux. With reference to the inclined loop in Fig 5.5, flow speed will reduce requiring smaller values of l_{drive} to drive the flow faster. Maintaining a modelled shock in an inclined loop requires more energetic waves with lower driving scales. In this case, the flow velocity profile is not symmetric, the velocity maximum will drift toward the upflowing footpoint. Should a shock form for inclined loops, it can be expected the shock front will drift toward the upflowing footpoint and not the downflowing footpoint due to the reduction in gravitational energy.

5.8 Discussion

This chapter summarises some of the highlights of the parameter study carried out in Chapter 4. Primarily, as two-fluid coronal loops are modelled, the coupling between the resonant protons and non-resonant electrons is very important (Section 5.2). As energy is transferred between proton and electron gas via Coulombic interactions, it is found that plasma non-equilibrium maximises in loops with minimum density (i.e. long and tenuous, hot loops). Short loop solutions are generally dense so Coulomb coupling is very efficient at retaining thermal equilibrium.

Isothermal coronal loops are the source of much debate, so solutions with isothermal characteristics are extracted from the vast array of possible solutions. Section 5.3 in-

vestigates four isothermal loops and find a strong relationship between loop length and isothermal temperature. A very delicate balance between the turbulence variables is required to maintain an isothermal state. The two main energy sources in an isothermal loop are wave flux and gravitational flux, if one is lost (or significantly reduced), isothermal loops cannot be modelled. From this, tests on loop inclination are carried out in Section 5.4. It is logical to conclude that an increase in inclination will decrease the gravitational energy flux. This imposes a serious restriction on the formation of isothermal loops as the majority of coronal loops are inclined to some degree (Aschwanden *et al.*, 2000a). This would suggest that *if* wave heating is a main contender in coronal loop heating and *if* isothermal temperature profiles in EUV loops do exist, there must be another form of heating supporting the flat temperature profile in the coronal section **or** the observational techniques used in the analysis of isothermal coronal loops are flawed (Schmelz *et al.*, 2001, Martens *et al.*, 2002, Schmelz, 2002, Aschwanden, 2002). Waves propagating from one footpoint as the *only* form of energy input is not sufficient to create a flat temperature profile, a temperature maximum above the upflowing footpoint or at the loop apex is more likely to result. In addition to these arguments, Winebarger *et al.* (2002) model a dynamic loop with an asymmetric (*ad-hoc*) heating rate (Fig. 4.16). There is strong heating in the upflowing section which decreases steadily with height. The heating minimises at the loop apex. The heating rate is then increased along the downflowing section of the loop which reaches a maximum at the downflowing footpoint. The 'V' shape of the energy input maintains the isothermal profile along the loop. On comparison with the heating rates in the model described here, wave flux dominates the upflowing section whereas gravitational flux dominates the downflowing section, approximating a similar 'V' profile as suggested by Winebarger *et al.* (2002). There is recognition that two forms of energy input are required in the upflowing and downflowing sections of coronal loops to maintain an isothermal profile if asymmetric flow is assumed.

Some cool loop solutions are also analysed (Section 5.5) where a comparison is made between the coolest solutions and the hottest solutions from results in Chapter 4. It is found that cool solutions can only be modelled *with* sufficient flow if the loop is of length $L > 100$Mm and modelled with low-l_{drive}. The coolest solutions for shorter loops tend to be quasi-hydrostatic.

The phenomenon of transition region moss is investigated in Section 5.6. This section moves away from analysis of the whole loop and focuses on a selection of loop footpoints. Keeping in mind the moss characteristics from observations (Peres *et al.*, 1994, Berger *et al.*, 1999), some hot loop solutions appear to have footpoint characteristics similar to moss features and provide a 'tracer' for EUV instruments to search for X-ray loop footpoints.

This chapter is completed by a study into the possibility of standing wave-driven shocks (Section 5.7) and arrive at some surprising results. The study in Chapter 4 clearly shows regions in model data where flow velocities are considered to be in a shocked state. Due to the constraints on this numerical method (i.e. difficulties in arriving at steady state if sudden changes in plasma parameters develop), these regions were largely disregarded. On further investigation it became apparent that some steady-state shocks can be successfully modelled. Further refinement of the model (such as improved grid resolution at loop apex) is required before an exhaustive study of wave-driven shocks can be carried out, but the results presented here are very positive.

Chapter 6

Conclusions

This thesis presents the results arising from the development of a unique, self-consistent numerical method and thorough parameter study of modelled turbulence and ion cyclotron resonance in a variety of coronal loops. Coronal loops are basic structures in the lower layers of the corona and form a link from the convection zone to the solar atmosphere. Any heating mechanism in the extended corona or solar wind is also assumed to operate along coronal loops. Following from solar wind heating and acceleration models, the full-implicit, one-dimensional numerical method is successfully applied. It is assumed that Alfvén waves launched from the photosphere (generated by an assumed shuffling motion of footpoints) are transmitted into the corona. A non-linear turbulent cascade transports energy to higher wave numbers in the turbulent spectrum, thus allowing waves of frequencies comparable with the plasma gyrofrequencies to resonate with protons. Coulomb coupling between proton and electron gas allows heating of non-resonant electrons. There may be significant non-equilibrium between plasma species as protons are preferentially heated.

Principal Results

The primary objective of this study is to complete a thorough parameter study of the turbulence variables governing the nature of the energy cascade. Alfvén wave amplitude and driving scale are found to have total control over the modelled loop plasma parameters (Section 4.2). A novel way of summarising the results of a large number of steady-state solutions is to map the plasma parameters against ξ, l_{drive} and L. From the iterative method (Section 3.3) hundreds of solutions are outputted, so when mapped, the plasma response to the propagating waves is clearly visible. The main results arising from this study can be summarised as follows:

1. Low values of l_{drive} generally increases flow velocity and density. For long loops ($L > 200$Mm), very low l_{drive} will result in standing shocks (Section 5.7).

2. The coolest loop solutions can be found at low-l_{drive} and low-L. Cool solutions are also found at maximum l_{drive} where modelled loops approach hydrostatic states (Section 5.5). The hottest loop solutions can be found at high-l_{drive} and high-L, although a region of optimised heating exists at a particular value of l_{drive} for each loop length.

3. There is significant thermal non-equilibrium between protons and electrons where plasma flow is either extremely large or very low. Low plasma densities weaken Coulomb interactions between the resonantly heated proton and electron gas (Section 5.2).

4. Short loops are generally overdense and long loops are underdense (Section 4.5).

5. The heating rate along loops heated by Kraichnan turbulence is more exponential than Kolmogorov loops suggesting the Kraichnan regime is less efficient at transferring energy to coronal loop plasma, requiring more energetic waves to be injected at low-l_{drive}. Kraichnan scales are confirmed to be 2 orders of magnitude

lower than Kolmogorov scales, so Kolmogorov turbulence is favoured (Section 4.3).

6. Isothermal loops can be modelled, but a very delicate balance between the turbulent variables and gravitational energy flux is required. For a constant magnetic field strength, a strong relationship between loop length and isothermal temperature presents itself (Section 5.3). The isothermal profile is lost as loop inclination is increased (Section 5.4).

7. The characteristics of EUV transition region 'moss' can be readily simulated, matching observed parameters, indicating footpoint brightening of X-ray loops may by symptomatic of rapid wave energy dissipation at low altitudes (Section 5.8).

8. A host of heating profiles exist across the whole range of coronal loops. This study confirms the idea that isothermal loops are heated by strongly asymmetric or non-uniform heating rates whilst loops with a temperature maximum at the apex exhibit quasi-uniform heating (Section 4.4).

Outstanding Problems

On reviewing the main conclusions from this study, several issues have been raised concerning the current understanding of the solar corona. The following points highlight the most contentious subjects:

1. High resolution measurements are required before a definitive answer to the nature of turbulent scales can be arrived at. Advanced methods of remote measuring techniques are required to establish the nature of $l_{\rm drive}$. Turbulence operating over Kolmogorov scales are assumed to be the best candidate as structures believed responsible for wave generation (such as photospheric flux footpoint shuffling)

can be resolved by instrumentation (Section 4.3).

2. How waves of these scales are produced at all is a matter of debate. It is known that waves of scales down to a thousand kilometers may be generated by features of the order of photospheric flux tubes or granulation as these features are well within the resolution limit of modern instruments. As explored in Chapter 4, the values of l_{drive} range from 10-10000km for loops of length 10-600Mm. Also, by assuming Kolmogorov turbulence for the results in the parameter study, the typical l_{drive} expected in the corona is quoted at 1200km (Chae *et al.*, 1998), so many of the results are well out of the range of the expected l_{drive}. More advanced theoretical ideas need to be conceived for generation mechanisms of sub-resolution scales. l_{drive} is therefore a free variable where no definitive link with solar scales can be made at present.

3. Current EUV observations debate the existence of isothermal coronal loops. The numerical method outlined in this study can reproduce similar isothermal profiles with comparable densities and flow velocities as observations (Section 5.3). It is however noted that a very delicate balance of the turbulence variables is required to regulate the heating rate along the loop to maintain the isothermal profile. Inclination of the loop results in loss of the isothermal profile, indicating loops modelling wave driven flow deviating from the vertical cannot sustain an isothermal temperature (Section 5.4). If an isothermal structure is to be maintained, another form of heating must replace the loss in gravitational energy flux (i.e. symmetrical wave propagation from both footpoints rather than one). Further investigation of EUV loop analysis methods are required.

Future Work

During development and analysis of this numerical method, limitations on the code itself or investigations out of the scope of this project are inevitable. Further work is required before a complete understanding and development of the self-consistent model can reach completion. The following points outline some areas of improvement and further study:

1. Direct comparisons with observations are now required. Results returned from the application of this self-consistent, turbulence-driven wave model compare favorably with observations, but definitive data analysis is needed.

2. It is well known that dynamic coronal loop models improve density when compared with observation, but a discrepancy remains. Direct comparisons with other loop models should therefore be carried out to see the role wave momentum deposition plays in density enhancements.

3. Once steps (1) and (2) are complete, the model can be developed so fitting routines can be applied to observational data. Waves definitely have a role to play in plasma heating in coronal loops, but to what degree of the total heating flux do they contribute? By developing an analysis package, the required wave characteristics can be modelled to fit observations. Once observations become more advanced, evidence for the required wave heating can be acquired.

4. There must be an awareness that other coronal heating mechanisms may contribute to the total heating flux. The possible coupling between turbulent flow and nanoflare generation is one such example how the heating mechanism may have secondary effects, amplifying loop heating.

5. The structure of modelled loops are of a semi-circular, constant cross-section configuration. Although this is a good approximation, the effect of a varying

cross-section or footpoint expansion may yield interesting results.

6. Modelling symmetric propagation of waves (from both footpoints) may produce other loop categories. This would promote chromospheric evaporation from both loop footpoints causing a collision and therefore an increase in density at the loop apex. Prominences may form. The physical loop structure may also be modelled with a 'dip' at the apex (increasing the local gravitational acceleration at the apex), also developing prominences.

7. Including additional plasma species in modelled loops would be an advantageous step. Tests of a 3-fluid loop model have been carried out but with little success. Further work is required to model ion cyclotron resonance with heavier ions such as helium (α-particles) so energy can be transferred down the mass hierarchy with an additional species ($He^{++} \rightarrow p \rightarrow e$).

This postgraduate research position was funded entirely by the Particle Physics and Astronomy Research Council (PPARC) rolling grant to UWA.

Publication List

O'Neill, I. J. and X. Li, Coronal loops heated by turbulence-driven Alfvén waves: A two fluid model, *A&A*, **435**, pages 1159–1167, 2005.

O'Neill, I. J. and X. Li, Turbulent Alfvén wave-driven coronal loops: A two-fluid model, in *ESA SP-575: SOHO 15 Coronal Heating*, pages 426–430, 2004.

Li, X., I. J. O'Neill and S. R. Habbal, Transition region and coronal loops heated by turbulence, in *ESA SP-547: SOHO 13 Waves, Oscillations and Small-Scale Transients Events in the Solar Atmosphere: Joint View from SOHO and TRACE*, pages 279–283, 2004.

Bibliography

Abdelatif, T. E., Heating of coronal loops by phase-mixed shear Alfvén waves, *ApJ*, **322**, pages 494–502, 1987.

Acton, L. W., C. J. Wolfson, E. G. Joki, J. L. Culhane, C. G. Rapley, R. D. Bentley, A. H. Gabriel, K. J. H. Phillips, R. W. Hayes & E. Antonucci, X-ray line widths and coronal heating, *ApJL*, **244**, pages L137–L140, 1981.

Alfvén, H., Magneto hydrodynamic waves, and the heating of the solar corona, *MNRAS*, **107**, pages 211–219, 1947.

Allen, L. A., S. R. Habbal & X. Li, Thermal coupling of protons and neutral hydrogen with anisotropic temperatures in the fast solar wind, *J. Geophys. Res.*, **105**(A10), pages 23 123–23 134, 2000.

Antiochos, S. K. & J. A. Klimchuk, A model for the formation of solar prominences, *ApJ*, **378**, pages 372–377, 1991.

Aschwanden, M. J., An evaluation of coronal heating models for Active Regions based on Yohkoh, SOHO, and TRACE observations, *ApJ*, **560**, pages 1035–1044, 2001.

Aschwanden, M. J., Observations and models of coronal loops: From Yohkoh to TRACE, in *Magnetic coupling of the solar atmosphere*, volume 188, pages 1–9, 2002a.

Aschwanden, M. J., Review of coronal oscillations - An observers view, in *Turbulence, waves and instabilities in the solar plasma*, pages 1–21, NATO Advanced Research Workshops, 2002b.

Aschwanden, M. J., The differential emission measure distribution in the multiloop corona, *ApJ*, **580**, pages L79–L83, 2002.

Aschwanden, M. J., *Physics of the Solar Corona. An Introduction*, Praxis Publishing Ltd., 2004, ISBN 3-540-22321-5.

Aschwanden, M. J., D. Alexander, N. Hurlburt, J. S. Newmark, W. M. Neupert, J. A. Klimchuk & G. A. Gary, Three dimensional stereoscopic analysis of solar active region loops. II. SOHO/EIT observations at temperatures of 1.5–2.5 MK, *ApJ*, **531**, pages 1129–1149, 2000a.

Aschwanden, M. J., R. W. Nightingale & D. Alexander, Evidence for non-uniform

heating of coronal loops inferred from multithread modelling of TRACE data, *ApJ*, **541**, pages 1059–1077, 2000b.

Aschwanden, M. J., C. J. Schrijver & D. Alexander, Modeling of coronal EUV loops observed with TRACE. I. Hydrostatic solutions with nonuniform heating, *ApJ*, **550**, pages 1036–1050, 2001.

Axford, W. I. & J. F. Mckenzie, *The Solar Wind*, University of Arizona Press, 1997.

Belcher, J. W., Alfvénic wave pressures and the solar wind, *ApJ*, **168**, pages 509–524, 1971.

Belcher, J. W. & L. Davis, Large-amplitude Alfvén waves in the interplanetary medium, 2, *J. Geophys. Res.*, **76**, pages 3534–3563, 1971.

Berger, T. E., B. De Pontieu, L. Fletcher, C. J. Schrijver, T. D. Tarbell & A. M. Title, What is moss?, *Sol. Phys.*, **190**, pages 409–418, 1999.

Biskamp, D., *Magnetohydrodynamic Turbulence*, Cambridge University Press, 2003, ISBN 0-521-81011-6.

Boland, B. C., E. P. Dyer, J. G. Firth, A. H. Gabriel, B. B. Jones, C. Jordan, R. W. P. McWhirter, P. Monk & R. F. Turner, Further measurements of emission line profiles in the solar ultraviolet spectrum, *MNRAS*, **171**, pages 697–724, 1975.

Bradshaw, S. J. & H. E. Mason, A self-consistent treatment of radiation in coronal loop modelling, *A&A*, **401**, pages 699–709, 2003.

Braginski, S. I., *Review of Plasma Physics*, New York: Consultants Bureau, 1965.

Bray, R. J., L. E. Cram, C. J. Durrant & R. E. Loughhead, *Plasma loops in the solar corona*, Cambridge University Press, 1991, ISBN 0-521-35107-3.

Bruno, R. & V. Carbone, The solar wind as a turbulence laboratory, *Living Reviews in Solar Physics*, **2**, page 4, 2005.

Cally, P. S. & T. D. Robb, Stability, structure and evolution of cool loops, *ApJ*, **372**, pages 329–335, 1991.

Cargill, P. J. & J. A. Klimchuk, Nanoflare heating of the corona revisited, *ApJ*, **605**, pages 911–920, 2004.

Cargill, P. J. & E. R. Priest, Siphon flows in coronal loops. I - Adiabatic flow, *Sol. Phys.*, **65**, pages 251–269, 1980.

Carroll, B. W. & D. A. Ostlie, *An Introduction to Modern Astrophysics*, Addison-Wesley, 1996, ISBN 0-201-54730-9.

Chae, J., A. I. Poland & M. J. Aschwanden, Coronal loops heated by MHD turbulence. I. A model of isobaric quiet sun loops with constant cross sections, *ApJ*, **581**, pages 726–735, 2002.

Chae, J., U. Schuhle & P. Lemaire, SUMER measurements of nonthermal motions: Constraints on coronal heating mechanisms, *ApJ*, **505**, pages 957–973, 1998.

Chae, J., H. Wang, J. Qiu, P. R. Goode & K. Wilhelm, Active Region loops observed with SUMER on board the SOHO, *ApJ*, **533**, pages 535–545, 2000.

Cheng, C. C., G. A. Doschek & U. Feldman, The dynamical properties of the solar corona from intensities and line widths of EUV forbidden lines of SI VIII, Fe XI, and Fe XII, *ApJ*, **227**, pages 1037–1046, 1979.

Cho, J., A. Lazarian & E. T. Vishniac, MHD Turbulence: Scaling Laws and Astrophysical Implications, *LNP Vol. 614: Turbulence and Magnetic Fields in Astrophysics*, **614**, pages 56–98, 2003.

Craig, I. J. D., A. N. McClymont & J. H. Underwood, The temperature and density structure of active region coronal loops, *A&A*, **70**, pages 1–11, 1978.

Del Zanna, G. & H. E. Mason, Solar active regions: SOHO/CDS and TRACE observations of quiescent coronal loops, *A&A*, **406**, pages 1089–1103, 2003.

Dere, K. P., J.-D. F. Bartoe, G. E. Brueckner, J. W. Cook & D. G. Socker, Discrete subresolution structures in the solar transition zone, *Sol. Phys.*, **114**, pages 223–237, 1987.

Dmitruk, P. & D. O. Gómez, Turbulent coronal heating and the distribution of nanoflares, *ApJ*, **484**, pages L83–L86, 1997.

Dmitruk, P. & D. O. Gómez, Scaling law for the heating of solar coronal loops, *ApJ*, **527**, pages L63–L66, 1999.

Dobrowolny, M., A. Mangeney & P. Veltri, Fully developed anisotropic hydromagnetic turbulence in interplanetary space, *Phys. Rev. Lett.*, **45**(2), pages 144–147, 1980.

Doschek, G. A., M. E. Vanhoosier, J.-D. F. Bartoe & U. Feldman, The emission-line spectrum above the limb of the quiet sun - 1175-1940 A, *ApJS*, **31**, pages 417–443, 1976.

Doyle, J. G., E. O'Shea, R. Erdelyi, K. P. Dere, D. G. Socker & F. P. Keenan, Nonthermal velocities in the solar transition zone and corona, *Sol. Phys.*, **173**, pages 243–258, 1997.

Doyle, J. G., L. Teriaca & D. Banerjee, Solar transition region line broadening: Limb to limb measurements, *A&A*, **356**, pages 335–338, 2000.

Elsässer, W. M., The hydromagnetic equations, *Phys. Rev.*, **79**, page 183, 1950.

Erdélyi, R., Heating of the Solar Corona: Review, *Publications of the Astronomy Department of the Eotvos Lorand University*, **15**, pages 7–19, 2005.

Erdélyi, R., J. G. Doyle, M. E. Perez & K. Wilhelm, Center-to-limb line width measurements of solar chromospheric, transition region and coronal lines, *A&A*, **337**, pages 287–293, 1998.

Fludra, A. & J. T. Schmelz, The absolute coronal abundances of sulfur, calcium and iron from Yohkoh-BCS flare spectra, *A&A*, **348**, pages 286–294, 1999.

Foukal, P., The temperature structure and pressure balance of magnetic loops in active regions, *Sol. Phys.*, **43**, pages 327–336, 1975.

Foukal, P. V., The pressure and energy balance of the cool corona over sunspots, *ApJ*, **210**, pages 575–581, 1976.

Golub, L. & M. Pasachoff, J., *The Solar Corona*, Cambridge University Press, 1997, ISBN 0-521-48535-5.

Gómez, D. & C. Ferro Fontán, Coronal heating by selective decay of MHD turbulence, *Sol. Phys.*, **116**, pages 33–44, 1988.

Gough, D. O. & M. E. McIntyre, Inevitability of a magnetic field in the Sun's radiative interior, *Nature*, **394**, pages 755–757, 2001.

Habbal, S. R., R. Ronan & G. L. Withbroe, Spatial and temporal variations of solar coronal loops, *Sol. Phys.*, **98**, pages 323–340, 1985.

Habbal, S. R. & R. Woo, Solar wind: The solar wind and the Sun-Earth link, *Astronomy and Geophysics*, **45**, pages 38–43, 2004.

Habbal, S. R., R. Woo, S. Fineschi, R. O'Neal, J. Kohl, G. Noci & C. Korendyke, Origins of the slow and the ubiquitous fast solar wind, *ApJL*, **489**, pages L103–L106, 1997.

Harrison, R. A., A. W. Hood & C. D. Pike, Off-limb EUV line profiles and the search for wave activity in the low corona, *A&A*, **392**, pages 319–327, 2002.

Heyvaerts, J. & E. R. Priest, Coronal heating by phase-mixed shear Alfven waves, *A&A*, **117**, pages 220–234, 1983.

Heyvaerts, J. & E. R. Priest, A self-consistent turbulent model for solar coronal heating, *ApJ*, **390**, pages 297–308, 1992.

Hollweg, J. V., Resonances of coronal loops, *ApJ*, **277**, pages 392–403, 1984.

Hollweg, J. V., Transition region, corona, and solar wind in coronal holes, *J. Geophys. Res.*, **91**, pages 4111–4125, 1986.

Hollweg, J. V. & W. Johnson, Transition region, corona, and the solar wind in coronal holes - Some two-fluid models, *J. Geophys. Res.*, **93**, pages 9547–9554, 1988.

Hood, A. W. & E. R. Priest, The equilibrium of solar coronal magnetic loops, *A&A*, **77**, pages 233–251, 1979.

Hu, Y. Q., A multistep implicit scheme for time-dependent 2-Dimensional magnetohydrodynamic flows, *J. Comput. Phys.*, **84**, pages 441–460, 1989.

Hu, Y. Q., R. Esser & S. R. Habbal, A fast solar wind model with anisotropic proton temperature, *J. Geophys. Res.*, **102**, pages 14 661–14 676, 1997.

Inverarity, G. W. & E. R. Priest, Turbulent coronal heating. III. Wave heating in coronal loops, *A&A*, **302**, pages 567–577, 1995.

Inverarity, G. W., E. R. Priest & J. Heyvaerts, Turbulent coronal heating. I. Sheared arcade, *A&A*, **293**, pages 913–926, 1995.

Ionson, J. A., Resonant absorption of Alfvenic surface waves and the heating of solar coronal loops, *ApJ*, **226**, pages 650–673, 1978.

Isenberg, P. A. & J. V. Hollweg, On the preferential acceleration and heating of solar wind heavy ions, *J. Geophys. Res.*, **88**, pages 3923–3935, 1983.

Kano, R. & S. Tsuneta, Scaling law of solar coronal loops obtained with YOHKOH, *ApJ*, **454**, pages 934–944, 1995.

Kano, R. & S. Tsuneta, Temperature distributions and energy scaling law of solar coronal loops obtained with Yokoh, *PASJ*, **48**, pages 535–543, 1996.

Kivelson, M. G. & C. T. Russell, *Introduction to Space Physics*, Cambridge University Press, 1995, ISBN 0-521-45714-9.

Kjeldseth Moe, O. & K. R. Nicolas, Emission measures, electron densities, and non-thermal velocities from optically thin UV lines near a quiet solar limb, *ApJ*, **211**, pages 579–586, 1977.

Klimchuk, J. A. & P. J. Cargill, Spectroscopic diagnostics of nanoflare-heated loops, *ApJ*, **553**, pages 440–448, 2001.

Klimchuk, J. A., S. Patsourakos & A. R. Winebarger, Are all coronal loops heated by nanoflares?, *AAS/Solar Physics Division Meeting*, **34**, pages –+, 2003.

Kolmogorov, A. N., The local structure of turbulence in incompressible viscous fluid for very large Reynolds numbers, *C. R. Acad. Sci. URSS*, **30**, page 301, 1941.

Kraichnan, R. H., Inertial-range spectrum of hydrodynamic turbulence, *Phys. Fluids*, **8**, pages 1385–1387, 1965.

Krieger, A. S., G. S. Vaiana & L. P. van Speybroeck, The X-ray corona and the photospheric magnetic field, in *IAU Symp. 43: Solar Magnetic Fields*, pages 397–411, 1971.

Lang, K. R., *The Cambridge Encyclopedia of the Sun*, Cambridge University Press, 2001, ISBN 0-521-78093-4.

Lenz, D. D., Energetics and structure of multispecies solar coronal loops, *ApJ*, **517**, pages 497–509, 1999.

Lenz, D. D., Effects of flow on structure and abundances in multispecies solar coronal loops, *ApJ*, **604**, pages 433–441, 2004.

Lenz, D. D., E. E. Deluca, L. Golub, R. Rosner & J. A. Bookbinder, Temperature

and emission-measure profiles along long-lived solar coronal loops observed with the Transition Region and Coronal Explorer, *ApJL*, **517**, pages L155–L158, 1999.

Li, X., Heating in coronal funnels by ion cyclotron waves, *ApJ*, **571**, pages L67–L70, 2002.

Li, X. & S. R. Habbal, Coronal loops heated by turbulence-driven Alfvén waves, *ApJ*, **598**, pages L125–L128, 2003.

Li, X., S. R. Habbal, J. V. Hollweg & R. Esser, Heating and cooling of protons by turbulence-driven ion cyclotron waves in the fast solar wind, *J. Geophys. Res.*, **104**(A2), pages 2521–2535, 1999.

Li, X., I. O'Neill & S. R. Habbal, Transition region and coronal loops heated by turbulence, in *ESA SP-547: SOHO 13 Waves, Oscillations and Small-Scale Transients Events in the Solar Atmosphere: Joint View from SOHO and TRACE*, pages 279–283, 2004.

Liewer, P. C., M. Velli & B. E. Goldstein, Alfvén wave propagation and ion cyclotron interactions in the expanding solar wind: One-dimensional hybrid simulations, *J. Geophys. Res.*, **106**, pages 29 261–29 282, 2001.

Lindemuth, I. & J. Killeen, Alternative direction implicit techniques for two-dimensional magnetohydrodynamic calculations, *J. Comput. Phys.*, **17**, page 181, 1973.

Litwin, C. & R. Rosner, On the structure of solar and stellar coronae - Loops and loop heat transport, *ApJ*, **412**, pages 375–385, 1993.

Litwin, C. & R. Rosner, Alfvén wave transmission and heating of solar coronal loops, *ApJ*, **499**, pages 945–950, 1998a.

Litwin, C. & R. Rosner, Coronal scale-height enhancement by MHD waves, *ApJ*, **506**, pages L143–L146, 1998b.

MacQueen, R. M., J. G. Blankner, D. F. Elmore, A. R. Lecinski & O. R. White, Initial CHIP HeI observations of solar limb activity, *Sol. Phys.*, **182**, pages 97–105, 1998.

Mariska, J. T., *The Solar Transition Region*, Cambridge University Press, 1992, ISBN 0-521-38261-0.

Mariska, J. T., U. Feldman & G. A. Doschek, Measurements of extreme-ultraviolet emission-line profiles near the solar limb, *ApJ*, **226**, pages 698–705, 1978.

Marsch, E., C. K. Goertz & K. Richter, Wave heating and acceleration of solar wind ions by cyclotron resonance, *J. Geophys. Res.*, **87**, pages 5030–5044, 1982.

Martens, P. C. H., J. W. Cirtain & J. T. Schmelz, The inadequacy of temperature measurements in the solar corona through narrowband filter and line ratios, *ApJL*, **577**, pages L115–L117, 2002.

Matthaeus, W. H. & M. L. Goldstein, Measurement of the rugged invariants of magnetohydrodynamic turbulence in the solar wind, *J. Geophys. Res.*, **87**, pages 6011–6028, 1982.

Matthaeus, W. H. & M. L. Goldstein, Magnetohydrodynamic turbulence in the solar wind, in *Solar Wind Five*, volume 188, pages 73–80, 1983.

McKenzie, J. F., Interaction between Alfvén waves and a multicomponent plasma with differential ion streaming, *J. Geophys. Res.*, **99**, pages 4193–4200, 1994.

McWhirter, R. W. P., P. C. Thonemann & R. Wilson, The heating of the solar corona. II - A model based on energy balance, *A&A*, **40**, pages 63–73, 1975.

Moriyasu, S., T. Kudoh, T. Yokoyama & K. Shibata, The nonlinear Alfvén wave model for solar coronal heating and nanoflares, *ApJL*, **601**, pages L107–L110, 2004.

Muller, R., T. Roudier, J. Vigneau & H. Auffret, The proper motion of network bright points and the heating of the solar corona, *A&A*, **283**, pages 232–240, 1994.

Narain, U. & P. Ulmschneider, Chromospheric and coronal heating mechanisms, *Space Sci. Rev.*, **54**, pages 377–445, 1990.

Narain, U. & P. Ulmschneider, Chromospheric and coronal heating mechanisms II, *Space Sci. Rev.*, **75**, pages 453–509, 1996.

Neugebauer, M. & C. W. Snyder, Solar Plasma Experiment, *Science*, **138**, pages 1095–1097, 1962.

Neupert, W. M., J. Newmark, J.-P. Delaboudinière, B. J. Thompson, R. C. Catura, J. D. Moses, J. B. Gurman, F. Portier-Fozzani, A. H. Gabriel, G. Artzner, F. Clette, P. Cugnon, A. J. Maucherat, J. M. Defise, C. Jamar, P. Rochus, K. P. Dere, R. A. Howard, D. J. Michels, S. Freeland, J. R. Lemen & R. A. Stern, Observations of coronal structures above an active region by EIT and implications for coronal energy deposition, *Sol. Phys.*, **183**, pages 305–321, 1998.

Ofman, L., J. A. Klimchuk & J. M. Davila, A self-consistent model for the resonant heating of coronal loops: The effects of coupling with the chromosphere, *ApJ*, **493**, pages 474–479, 1998.

O'Neill, I. J. & X. Li, Turbulent Alfvén wave-driven coronal loops: A two-fluid model, in *ESA SP-575: SOHO 15 Coronal Heating*, pages 426–430, 2004.

O'Neill, I. J. & X. Li, Coronal loops heated by turbulence-driven Alfvén waves: A two fluid model, *A&A*, **435**, pages 1159–1167, 2005.

Orlando, S., G. Peres & S. Serio, Models of stationary siphon flows in stratified, thermally conducting coronal loops. I. Regular solutions, *A&A*, **294**, pages 861–873, 1995a.

Orlando, S., G. Peres & S. Serio, Models of stationary siphon flows in stratified,

thermally conducting coronal loops. II. Shocked solutions, *A&A*, **300**, pages 549–558, 1995b.

Parker, E. N., Hydromagnetic dynamo models, *ApJ*, **122**, pages 293–314, 1955.

Parker, E. N., Stimulated dissipation of magnetic discontinuities and the origin of solar flares, *Sol. Phys.*, **111**, pages 297–308, 1987.

Parker, E. N., Nanoflares and the solar X-ray corona, *ApJ*, **330**, pages 474–479, 1988.

Parnell, C., Magnetic carpets and hot coronae, in *A&G*, volume 43, pages 16–20, 2002.

Parnell, C. E. & P. E. Jupp, Statistical analysis of the energy distribution of nanoflares in the Quiet Sun, *ApJ*, **529**, pages 554–569, 2000.

Patsourakos, S., J. A. Klimchuk & P. J. MacNeice, The inability of steady-flow models to explain the extreme-ultraviolet coronal loops, *ApJ*, **603**, pages 322–329, 2004.

Peres, G., F. Reale & L. Golub, Loop models of low coronal structures observed by the Normal Incidence X-ray Telescope (NIXT), *ApJ*, **422**, pages 412–415, 1994.

Poletto, G., G. S. Vaiana, M. V. Zombeck, A. S. Krieger & A. F. Timothy, A comparison of coronal X-ray structures of active regions with magnetic fields computed from photospheric observations, *Sol. Phys.*, **44**, pages 83–99, 1975.

Porter, L. J. & J. A. Klimchuk, Soft X-ray loops and coronal heating, *ApJ*, **454**, pages 499–511, 1995.

Priest, E. R., C. R. Foley, J. Heyvaerts, T. D. Arber, D. Mackay, J. L. Culhane & L. W. Acton, A method to determine the heating mechanisms of the solar corona, *ApJ*, **539**, pages 1002–1022, 2000.

Reale, F., Inclination of large coronal loops observed by TRACE, *Sol. Phys.*, **190**, pages 139–144, 1999.

Reale, F., G. Nigro, F. Malara, G. Peres & P. Veltri, Modeling a coronal loop heated by magnetohydrodynamic turbulence nanoflares, *ApJ*, **633**, pages 489–498, 2005.

Reale, F., G. Peres, S. Serio, R. M. Betta, E. E. DeLuca & L. Golub, A brightening coronal loop observed by TRACE. II. Loop modeling and constraints on heating, *ApJ*, **535**, pages 423–437, 2000.

Reisenfeld, D. B., S. P. Gary, J. T. Gosling, J. T. Steinberg, D. J. McComas, B. E. Goldstein & M. Neugebauer, Helium energetics in the high-latitude solar wind: Ulysses observations, *J. Geophys. Res.*, **106**, pages 5693–5708, 2001.

Robb, T. D. & P. S. Cally, Steady and nonsteady siphon flow in hot coronal loops, *ApJ*, **397**, pages 329–336, 1992.

Roberts, D. A., M. L. Goldstein, D. L. Klein & W. H. Matthaeus, The nature and evolution of magnetohydrodynamic fluctuations in the solar wind - Voyager observations, *J. Geophys. Res.*, **92**, pages 11 021–11 040, 1987.

Rosner, R., W. H. Tucker & G. S. Vaiana, Dynamics of the quiescent solar corona, *ApJ*, **220**, pages 643–665, 1978.

Saba, J. L. R. & K. T. Strong, Coronal dynamics of a quiescent active region, *ApJ*, **375**, pages 789–799, 1991.

Sakai, J. I., A. Takahata & I. V. Sokolov, Heating of coronal loop footpoints by magnetic reconnection resulting from surface Alfvén waves and colliding plasma flows in chromospheric current sheets, *ApJ*, **556**, pages 905–911, 2001.

Schmelz, J. T., Are coronal loops isothermal?, *ApJ*, **578**, pages L161–L164, 2002.

Schmelz, J. T., K. Nasraoui, V. L. Richardson, P. J. Hubbard, C. R. Nevels & J. E. Beene, All coronal loops are the same: Evidence to the contrary, *ApJL*, **627**, pages L81–L84, 2005.

Schmelz, J. T., R. T. Scopes, J. W. Cirtain, H. D. Winter & J. D. Allen, Observational constraints on coronal heating models using coronal diagnostics spectrometer and Soft X-Ray Telescope data, *ApJ*, **556**, pages 896–904, 2001.

Schmieder, B., D. M. Rust, M. K. Georgoulis, P. Démoulin & P. N. Bernasconi, Emerging flux and the heating of coronal loops, *ApJ*, **601**, pages 530–545, 2004.

Serio, S., G. Peres, G. S. Vaiana, L. Golub & R. Rosner, Closed coronal structures. II. Generalised hydrostatic model, *ApJ*, **243**, pages 288–300, 1981.

Spadaro, D., A. C. Lanzafame, L. Consoli, E. Marsch, D. H. Brooks & J. Lang, Structure and dynamics of an active region loop system observed on the solar disc with SUMER on SOHO, *A&A*, **359**, pages 716–728, 2000.

Spitzer, L., *Physics of fully ionized gases*, Physics of Fully Ionized Gases, New York: Interscience (2nd edition), 1962.

Strong, K. T., J. L. R. Saba, B. M. Haisch & J. T. Schmelz, *The many faces of the sun : a summary of the results from NASA's Solar Maximum Mission*, New York : Springer, 1999.

Testa, P., G. Peres & F. Reale, Emission measure distribution in loops impulsively heated at the footpoints, *ApJ*, **622**, pages 695–703, 2005.

Tsiklauri, D. & V. M. Nakariakov, Wide-spectrum slow magnetoacoustic waves in coronal loops, *A&A*, **379**, pages 1106–1112, 2001.

Tu, C. Y. & E. Marsch, MHD structures, waves and turbulence in the solar wind: Observations and theories, *Space Sci. Rev.*, **73**(1), pages 1–210, 1995.

Ulrich, R. K., Observations of magnetohydrodynamic oscillations in the solar atmosphere with properties of Alfvén waves, *ApJ*, **465**, pages 436–450, 1996.

Vaiana, G. S., J. M. Davis, R. Giacconi, A. S. Krieger, J. K. Silk, A. F. Timothy & M. Zombeck, X-Ray Observations of Characteristic Structures and Time Variations

from the Solar Corona: Preliminary Results from SKYLAB, *ApJL*, **185**, pages L47–L51, 1973.

van Tend, W., Coronal heating by prominence turbulence, *Sol. Phys.*, **66**, pages 29–37, 1980.

Vourlidas, A., J. A. Klimchuk, C. M. Korendyke, T. D. Tarbell & B. N. Handy, On the correlation between coronal and lower transition region structures at arcsecond scales, *ApJ*, **563**, pages 374–380, 2001.

Walsh, R. W. & J. Ireland, The heating of the solar corona, *A&ARv*, **12**, pages 1–41, 2003.

Warren, H. P., A. R. Winebarger & P. S. Hamilton, Hydrodynamic modeling of active region loops, *ApJ*, **579**, pages L41–L44, 2002.

Weber, M. A., J. T. Schmelz, E. E. DeLuca & J. K. Roames, Isothermal bias of the "filter ratio" method for observations of multithermal plasma, *ApJL*, **635**, pages L101–L104, 2005.

Wilhelm, K., B. N. Dwivedi & L. Teriaca, On the widths of the Mg X lines near 60 nm in the corona, *A&A*, **415**, pages 1133–1139, 2004.

Wilhelm, K., A. Fludra, L. Teriaca, R. A. Harrison, B. N. Dwivedi & C. D. Pike, The widths of vacuum-ultraviolet spectral lines in the equatorial solar corona observed with CDS and SUMER, *A&A*, **435**, pages 733–741, 2005.

Winebarger, A. R., H. Warren, A. van Ballegooijen, E. E. DeLuca & L. Golub, Steady flows detected in extreme-ultraviolet loops, *ApJ*, **567**, pages L89–L92, 2002.

Winebarger, A. R., H. P. Warren & J. T. Mariska, Transition Region and Coronal Explorer and Soft X-Ray Telescope Active Region loop observations: comparisons with static solutions of the hydrodynamic equations, *ApJ*, **587**, pages 439–449, 2003.